

The future influences of climate change and river regulation on high-latitude
circulation as determined by ocean modelling

by

Yiran Xu

A thesis submitted in partial fulfillment of the requirements for the degree of

Master of Science

Department of Earth and Atmospheric Sciences
University of Alberta

© Yiran Xu, 2023

Abstract

The Hudson Bay Complex (HBC), encompassing Foxe Basin (FB), Hudson Strait (HS), Ungava Bay (UB), Hudson Bay (HB), and James Bay (JB), experiences notable shifts in freshwater sources. Despite being smaller than the Arctic Ocean, the HBC annually receives around 900 km^3 of river discharge, constituting about 25% of the Arctic Ocean's inflow.

The HBC receives freshwater primarily from river runoff and ice freeze-thaw processes, both impacted by human activities (e.g., diversions, dams, and reservoirs) and climate change. Using the NEMO ocean-sea ice model with the Arctic and Northern Hemisphere Atlantic (ANHA) configuration, we investigated how river regulation and climate change affect HBC's freshwater dynamics.

We applied an ensemble of five climate simulations, which were from the Coupled Model Inter-comparison Project 5 (CMIP5) model experiments. They were initialized between 1980 and 2005, forced with naturalized and regulated river runoff, and driven by different representative concentrations of greenhouse gases (RCP4.5 and RCP8.5) over the 2006–2070 period. The results showed a general increase in freshwater content, along with a sharp decrease in ice thickness and concentration in the future. The mixed layer depth can reach up to 230 m near the north side of HS. With increased freshwater from rivers and ice thawing, future mixed layers are projected to be slightly shallower compared to the historical period. Finally, we examined atmospheric forcing changes to understand ocean-sea ice-atmosphere interactions in a changing climate. Our results reveal significant impacts of distinct ensemble members on salinity and freshwater content variations, reflecting hydrological cycle evolution in climate models. Differences in content between naturalized and regulated regimes are linked to factors including freshwater residence time and discharge timing.

Acknowledgments

First of all, I would like to express my sincere appreciation to my supervisor Dr. Paul G. Myers for his support and encouragement during my MSc study. Without the support of him, I would not have gotten far. His knowledge, advice and confidence inspired me these ideas and kept on the track to my goal. His careful editing greatly improved this thesis.

Besides my supervisor, I also would like to thank all the rest of my committee members for their insightful advices during my study. Thank my colleagues for their valuable comments to help me get closer to my degree. Especially, I would like to thank Natasha Ridenour, who assist me in how to remap river runoff with our model configuration and gave me confidence when I had difficulties on my research.

Thanks also go to all my colleagues no matter how long we had been together and where you are now. Big thanks to Laura Castro de la Guardia, Liam Buchart, Ran Tao, Nathan Grivault for their valuable discussion and kind assistance in my study. I would like to thank Brandon Justin Bethel, although we were colleagues for just three months in Nanjing, he took some time went through my plots and gave me advice on my thesis draft.

Last but not least, I want to thank my parents, Changqing and Aimei, who are my biggest supporters: for supporting my decision to pursue graduate studies. They always give their patience to me and talk with me as close friends when I am in bad mood.

Contents

List of Tables	vii
List of Figures	viii
1 Introduction	1
1.1 The Hudson Bay Complex	1
1.2 Freshwater Properties	4
1.2.1 River runoff and estuaries	4
1.2.2 Calculation of Freshwater	6
1.2.3 Arctic Freshwater System	7
1.2.4 The Sources and Storage of the Freshwater in the Arctic Ocean	9
1.2.5 Arctic Ocean Freshwater Change	10
1.3 River Regulation	10
1.4 Thesis Objectives and Outline	11
Bibliography	13
2 An Ocean-Ice Coupled Model: Nucleus for European Modelling of the Ocean (NEMO)	19
2.1 Ocean Component	19
2.1.1 Primitive Equations	21
2.1.2 Boundaries	23
2.1.3 Curvilinear Coordinate System and Spatial Discretization	26
2.1.4 Subgrid Scale Physics	30

2.1.5	Time Discretization	32
2.2	Sea-Ice Component	35
2.2.1	Sea-Ice Dynamics	36
2.2.2	Sea-Ice Thermodynamics	38
2.2.2.1	Vertical Growth and Decay	38
2.2.2.2	Lateral Growth and Decay	39
2.2.3	Ocean-Ice Coupling	40
	Bibliography	42
3	Experiment Setup	46
3.1	Numerical Modelling of the Ocean and Sea Ice	46
3.2	Method and Theoretical Background	47
3.2.1	Configuration	47
3.2.2	Initial Conditions	48
3.2.3	Ensemble Climate Data	48
3.2.4	Runoff Forcing Fields	49
3.2.5	Remapping Method	51
	Bibliography	54
4	Influences of Climate Change and River Regulation on Hudson Bay Complex Freshwater Dynamics	58
4.1	Introduction	59
4.2	Methods and Data	63
4.2.1	Statistical Analyses Method	64
4.2.2	Climate Ensemble	64
4.2.3	River Runoff Datasets	65
4.3	Results	66
4.3.1	Analysis of Atmospheric Forcing Fields	66
4.3.2	Net heat flux	70
4.3.3	Maximum Mixed Layer Depth	71
4.3.4	Sea Ice Properties	75

4.3.5	Oceanic Properties	86
4.3.5.1	Temperature and Heat Content	86
4.3.5.2	Salinity and Freshwater Content	88
4.4	Discussion and conclusion	91
	Bibliography	100
5	Conclusion	109
5.1	Main Findings	110
5.1.1	The Significance of Findings	111
5.2	Thesis Summary	112
5.2.1	Limitations and Further work	114
	Bibliography	117

List of Tables

4.1	The mean, standard deviation (SD), coefficient of variation (CV) in annual ice concentration and ice thickness time series with slope and intercept (Inter) of the linear regressions (The trend starts in year 2006).	83
4.2	The mean, standard deviation (SD), coefficient of variation (CV) in spring (MAM), fall (SON), and winter (DJF) ice concentration and ice thickness time series with slope and intercept (Inter) of the linear regressions (The trend starts in year 2006).	83
4.3	The mean, standard deviation (SD), coefficient of variation (CV) in annual heat content, temperature, freshwater content, and salinity time series with slope and intercept (Inter) of the linear regressions (The trend starts in year 2006).	97
4.4	The mean, standard deviation (SD), coefficient of variation (CV) in spring (MAM),fall (SON), and winter (DJF) heat content and temperature time series with slope and intercept (Inter) of the linear regressions (The trend starts in year 2006).	98
4.5	The mean, standard deviation (SD), coefficient of variation (CV) in spring (MAM),fall (SON), and winter (DJF) freshwater content and salinity time series with slope and intercept (Inter) of the linear regressions (The trend starts in year 2006).	99

List of Figures

1.1	Map of the Hudson Bay Complex (HBC) in the model, which denotes the bathymetry structure and the river estuaries (figures with details of drainage basins surrounding the complex can be found in Déry et al., 2016; Braun et al., 2021) around the complex. The locations of Baffin Bay, Davis Strait, and Labrador Sea are also labeled, which play significant roles in freshwater exchanges within the HBC. A relative small scale figure of the HBC showing its specific components will be presented in Chapter 4 as Figure 4.1.	2
2.1	The spherical coordinate system is used in NEMO. The horizontal unit vectors, \mathbf{i} and \mathbf{j} (in red), orthogonal to each other, are described by λ and φ . The vertical upward vector (which is perpendicular to the horizontal plan of (\mathbf{i}, \mathbf{j})) is shown as \mathbf{k} (in red).	23
2.2	The surface and bottom boundaries of the ocean in NEMO. The sea floor boundary is defined as $z = -H(i, j)$ and the ocean surface boundary is defined as $z = \eta(i, j, k, t)$, where η is the height of the sea surface and is allowed to change over time. Both H and η are referenced to the mean sea surface, $z = 0$	24
2.3	Schematic of the placement of model variables on the staggered horizontal Arakawa grids used in ocean models. T refers to tracer and density, $u; v$ refer to horizontal velocity components, h refers to layer thickness, and ψ refers to horizontal streamfunction or surface height. This figure is from Fig. 3.1 of Haidvogel and Beckmann (1999).	28

2.4	3D (A) and 2D (B) over the horizontal plane representation of a C-grid cell in the NEMO with every computed variable. $\mathbf{T} = (T, S, p, \rho)$ is a vector containing scalar variables, shown by the red squares in the core of each cell. F shown by light blue pentagons represents vorticity. $\mathbf{U} = (U, V, W)$ is the vector of velocity, whose three components are represented by blue circles, green pentagons, and purple pentagons respectively. The size of each grid cell is defined by three local scale factors, e_1, e_2 , and e_3 , shown in (A).	29
2.5	Vertical grid of traditional z-coordinate with full steps (left) and z-coordinate with partial steps (right) in model. Dash lines represent the real bathymetry of ocean and shaded cells show the simulated bathymetry in the model.	29
2.6	Temporal and spatial pattern of the time stepping in the Leapfrog scheme is used for non-diffusive processes. Inputs from different time and space steps are shown by the terminal points of arrows, while the points of using output as input are shown by the beginning of arrows.	35
3.1	The Arctic and Northern Hemispheric Atlantic $1/4^\circ$ (ANHA4) horizontal mesh (every 10 grids, color shows the resolution in kilometers). (A) The entire ANHA4 configuration with $544 \times 800 \times 50$ grid points. (B) The same configuration as in (A) where zoom in the HBC.	52
3.2	The river runoff mapping flow chart. Based on Figure 2 in Hu and Myers, 2015.	53
4.1	The Hudson Bay Complex (HBC) Bathymetry. Abbreviations for specific geographic locations stands for FB = Foxe Basin, HS = Hudson Strait, UB = Ungava Bay, HB = Hudson Bay, JB = James Bay, PCI = Prince Charles Island, SI = Southampton Island, FHS = Fury and Hecla Strait, RWS = Roes Welcome Sound, and BI = Belcher Islands. Modified based on Ridenour et al., 2019b.	63

4.2	The schematic of ensemble runs with the impacts of climate change and river regulation (Note that naturalized runs are with unregulated rivers and regulated runs are with regulated rivers). Data are from the Meteorological Research Institute Coupled General Circulation Model (MRI-CGCM3), the Geophysical Fluid Dynamics Laboratory Community Model (GFDL-CM3), and the Fifth Model for Interdisciplinary Research On Climate (MIROC5). Orange boxes to the left represent sources of data for the initialized historical period: 1981–2005, while the ten brown boxes to the right are the future experiments which run from 2006 to 2070.	67
4.3	Time series of annual (A) air temperature at 2 m height ($^{\circ}\text{C}$), (C) precipitation (m), and (E) wind speed (m/s) averaged over the HBC from 1981 to 2070 for 5 climate runs. Seasonal time series of these variables are given in (B), (D), and (F) respectively.	69
4.4	Annual (A) and seasonal (B) time series of the total net heat flux (Wm^{-2}) that are averaged over the HBC from 1981 to 2070 for 5 climate runs.	72
4.5	Annual maximum mixed layer depths (MMLDs; in m) in the HBC.	75
4.6	Annual MMLD spatial distributions for five model experiments (A) MRI-CGCM3 historical and RCP4.5, (B) MRI-CGCM3 RCP8.5, (C) GFDL historical and RCP4.5, (D) MIROC5 historical and RCP4.5, and (E) MIROC5 RCP8.5.	76
4.7	Time series of annual (A) sea ice concentration (SIC; in %) and (B) sea ice thickness (SIT; in m) over the HBC from 1981 to 2070 for 5 naturalized runs only influenced by climate change. Seasonal time series of the two variables are given in (B) and (D).	81
4.8	Similar to Figure 4.7 but considering impacts of both river regulation and climate change. Time series of annual (A) sea ice concentration (SIC; in %) and (C) sea ice thickness (SIT; in m) over the HBC from 1981 to 2070 for 5 regulated runs. Seasonal time series of the two variables are given in (B) and (D).	82

4.9	Spatial distributions of (A) annual and (B) January–March sea ice concentration (SIC; in %) in the HBC. Shown for outputs from MRI-CGCM3 (top: a, b, c), MIROC5 (middle: d, e, f), and GFDL (bottom: g, h). Columns from left to right represent historical forcing simulations for 1981–2005, RCP4.5 forcing simulations for 2006–2070, and RCP8.5 forcing simulations for 2006–2070. . . .	84
4.10	Spatial distributions of (A) annual and (B) January–March sea ice thickness (SIT; in <i>m</i>) in the HBC. Shown for outputs from MRI-CGCM3 (top: a, b, c), MIROC5 (middle: d, e, f), and GFDL (bottom: g, h). Columns from left to right represent historical forcing simulations for 1981–2005, RCP4.5 forcing simulations for 2006–2070, and RCP8.5 forcing simulations for 2006–2070. . . .	85
4.11	Annual (left column) and seasonal (right column) time series of temperature (T; in °C) and heat content (HC; in J) over the HBC from 1981 to 2070 for 5 naturalized runs only influenced by climate change. Upper panels (A–D) depict the two variables averaged on top 50 m and lower panels (E–H) depict the two variables averaged on top 250 m.	93
4.12	Similar to Figure 4.11 but considering impacts of both river regulation and climate change. Annual (left column) and seasonal (right column) time series of temperature (T; in °C) and heat content (HC; in J) over the HBC from 1981 to 2070 for 5 regulated runs. Upper panels (A–D) depict the two variables averaged on top 50 m and lower panels (E–H) depict the two variables averaged on top 250 m.	94
4.13	Annual (left column) and seasonal (right column) time series of salinity (S; in psu) and freshwater content (FWC; in km ³) over the HBC from 1981 to 2070 for 5 naturalized runs only influenced by climate change. Upper panels (A–D) depict the two variables averaged on top 50 m and lower panels (E–H) depict the two variables averaged on top 250 m.	95

4.14 Similar to Figure 4.13 but considering impacts of both river regulation and climate change. Annual (left column) and seasonal (right column) time series of salinity (S; in psu) and freshwater content (FWC; in km³) over the HBC from 1981 to 2070 for 5 regulated runs. Upper panels (A-D) depict the two variables averaged on top 50 m and lower panels (E-H) depict the two variables averaged on top 250 m. 96

Chapter 1

Introduction

1.1 The Hudson Bay Complex

The Hudson Bay Complex (HBC), which is comprised of five sub-regions of Foxe Basin (FB), Hudson Strait (HS), Ungava Bay (UB), Hudson Bay (HB), and James Bay (JB), occupies an area of 1.3 million km² area (Kuzyk and Candlish, 2019) (Figure 1.1). The complex is connected to the Labrador Sea and the North Atlantic Ocean via HS in its eastern part, and to the Canadian Arctic Archipelago (CAA) and the Arctic Ocean through FB in its northern part. The HBC is one of the largest inland seas around the world and the area of its total drainage basins is 3.8 million km², making it the largest watershed in Canada over the five provinces containing Alberta, Manitoba, Ontario, Québec, and Saskatchewan (Stewart and Lockhart, 2005; Andrews et al., 2016; Lukovich et al., 2021). The complex is unique among the oceans all over the world as it is almost ice-free during the summer months and is nearly fully covered by ice during winter (Drinkwater, 1986; Houser and Gough, 2003; Andrews et al., 2018).

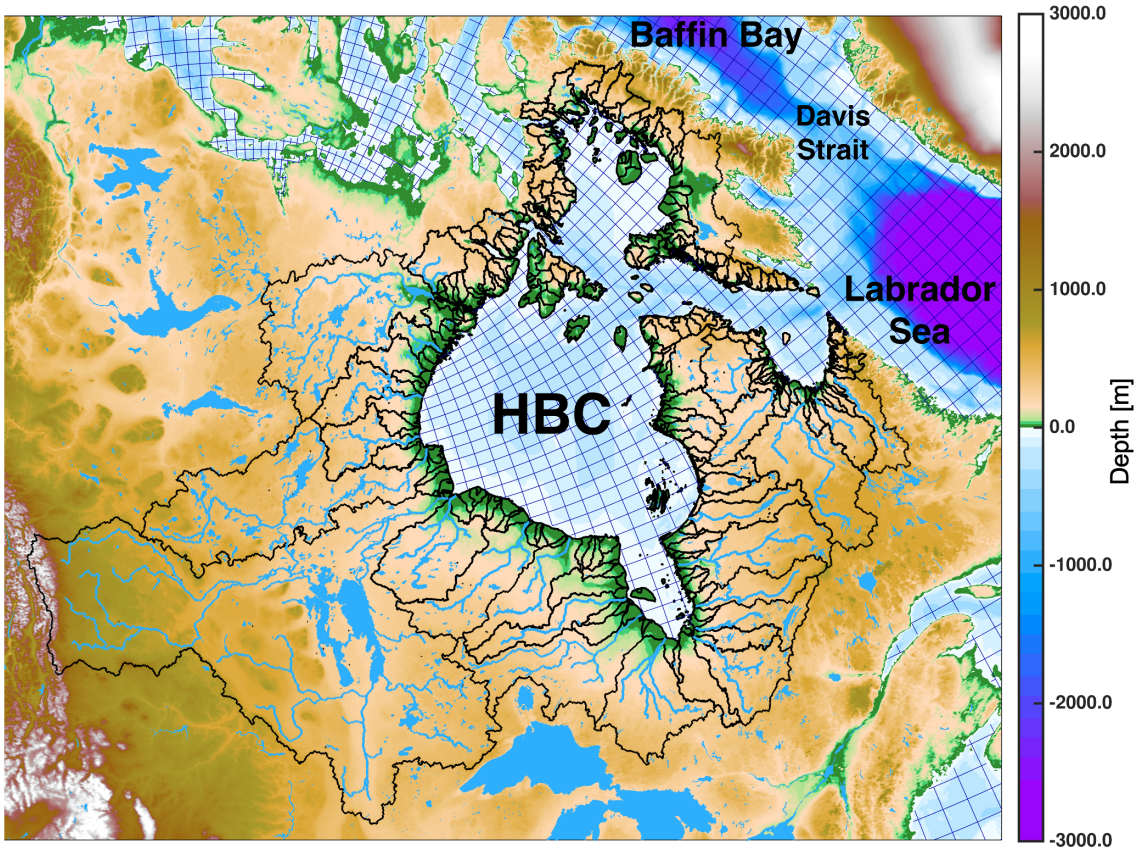


Figure 1.1: Map of the Hudson Bay Complex (HBC) in the model, which denotes the bathymetry structure and the river estuaries (figures with details of drainage basins surrounding the complex can be found in Déry et al., 2016; Braun et al., 2021) around the complex. The locations of Baffin Bay, Davis Strait, and Labrador Sea are also labeled, which play significant roles in freshwater exchanges within the HBC. A relative small scale figure of the HBC showing its specific components will be presented in Chapter 4 as Figure 4.1.

It also receives a large amount of freshwater (both liquid and solid) runoff. With regard to the system of HBC freshwater budget, the complex is fed by approximately $940 \text{ km}^3 \text{ yr}^{-1}$ of freshwater coming from rivers, which is comparable to the combined outflows of the Mackenzie and St Lawrence rivers (Stadnyk et al., 2019). Due to the restriction of the counterclockwise current mainly within Hudson Bay, river runoff is firstly transported along the coastline then secondly to Hudson Strait and the Labrador Sea, finally joining with other water sources in the North Atlantic Ocean. The annual ice-melting freshwater to the surface of the whole region is $\sim 1500 \text{ km}^3$. The evaporation surpasses the precipitation in the most of the HBC, while the reverse is true in James Bay (Hamilton, 2013).

Typically, the HB is thought to have a cyclonic flow all year round (Dunbar, 1982; Ingram and Larouche, 1987; Prinsenber, 1988; Lavoie et al., 2013). The general cyclonic circulation

pattern in HB brings approximately $760 \text{ km}^3 \text{ yr}^{-1}$ freshwater within the bay before the freshwater flows away through HS. The freshwater mainly comes from river discharges around HB and cold freshwater from the Arctic Ocean via FB (Déry et al., 2011; JafariKhasragh et al., 2019). However, from the study of Ridenour et al. (2019), by using a 3D high-resolution ocean general circulation model, it is shown that the circulation pattern in western HB remains cyclonic year around while a weak anticyclonic circulation is presented in eastern HB in spring and summer, with the mean flow through the central part directly in summer (May to August) in this area. This simulated phenomenon is in agreement with Absolute Dynamic Topography (ADT) and velocity observations.

Understanding the variations in ocean and ice properties in response to climate change and river regulation is critical for comprehending the ecosystem conditions of the HBC, particularly with regards to freshwater properties. As mentioned above, the HBC is characterized by seasonal ice cover, with ice-free conditions in summer and ice-covered conditions in winter. Freshwater exchanges, which are governed by vertical and horizontal physical processes of mixing, play a vital role in the delivery of nutrients that support biological life in the system (McCullough et al., 2019).

However, the impact of climate change, resulting from anthropogenic factors such as air pollutant and greenhouse gas emissions, as well as land use changes, has led to increased instability within the HBC due to hunting, watercraft, and unsafe ice conditions for on-ice travel (Stewart and Lockhart, 2005; Stadnyk et al., 2019; Babb et al., 2019). Moreover, as temperatures rise during winter, human activities in the region have also increased. Human-induced activities such as fluvial diversions and the construction of dams and reservoirs can significantly impact river dynamics (McKinney et al., 2015). Although the sources of freshwater and saltwater to the complex are generally understood, the characteristics of dynamical and thermodynamical processes and the impacts of climate change and river regulations on multiple properties are still not fully comprehended.

Thus, this thesis aims to investigate the variations in ocean and ice properties in the HBC, with a focus on freshwater properties and their role in supporting biological life. Additionally, we will assess the impact of climate change and river regulation on these properties, including the influence of human-induced activities.

1.2 Freshwater Properties

1.2.1 River runoff and estuaries

River runoff mainly influences the state of coastal regions. It can reduce the salinity of the surface layer of the ocean and even of the deeper ocean if the vertical mixing is sufficient. Along with the river runoff, there is a large amount of suspended sediment. Generally, there is a remarkable seasonal variation of river runoff, which causes much larger seasonal fluctuations of salinity in coastal waters than in the open ocean. The changes of the seasonal salinity will share a similar pattern of the local precipitation in coastal regions where precipitation occurs mainly as rain. In regions where rivers are fed by meltwater from snowfields or glaciers, such as some locations in the Arctic, the river runoff increases in the summer with large amounts that is many times larger than the runoff in the winter.

Together with other freshwater resources transported to the ocean, the fresh river runoff flowing out over saltier open ocean water creates a strong halocline, which is highly stable to vertical mixing. Consequently, higher temperatures will be present in the surface layer of the ocean during summer months, while in winter especially in high latitudes of the northern hemisphere, the temperature of the surface water can be lower than that of the water underlying the halocline, which is called a "temperature inversion" because of the existence of this stable halocline. Thus, the ice formation tends to happen first in coastal waters, as "fast ice" (it is noted that the shallowness of the coastal region also contributes). In regions like the Arctic where multiyear ice exists, the new coastal ice transports seaward until it meets the first-year ice spreading shoreward from the multiyear pack ice.

As mentioned above, the river water often carries suspended sediment, thus, coastal waters frequently have low optical transparency. Sometimes this sediment is carried in the surface layer with low salinity for some distance while the deeper layer with more saline water remains clear. The deposition of the sediment results in shoaling and creates difficulty to navigation. Generally, the location of the deposition is affected by the spreading of salinity since more and more salinity can cause flocculation of the sediment and accelerating the process of subsidence.

To estimate the influences of river runoff, especially from large rivers, the reduction of salinity and sediments in water can always be measured to trace the runoff far away from the

coast. Examples of major influences on the open ocean can be found in the tropical Atlantic with the Amazon and Congo Rivers and other regions. The net freshwater input from rivers plays an important role in the freshwater budget of oceans. Runoff is almost equivalent to precipitation-minus-evaporation of the open ocean because it deposits net precipitation over land into the ocean.

The Arctic Ocean has a low surface salinity mixed layer, which is partly the result of freshwater discharge from some of the largest rivers on the planet, such as Lena and Yenisey Rivers. Several studies have investigated the drivers of changes in the maximum mixed layer depth (MMLD) in Arctic and sub-Arctic regions, including the Hudson Bay. For example, Wang et al. (2021); Perovich and Richter-Menge (2009) suggested that the reduction in the MMLD in the Arctic Ocean was mainly driven by the increase in SST, while the decrease in the MMLD in the Beaufort Sea was more influenced by the increase in freshwater input. Similarly, Grivault et al. (2018) showed that the reduction in the MMLD in the Canadian Arctic Archipelago (CAA) was driven by the increase in freshwater input and the reduction in wind stress.

As the river discharge can reach temperatures of $> 10^{\circ}\text{C}$ during the period of spring freshet, the Arctic heat and freshwater budget can be significantly influenced by river discharge. The input of river discharge to the Arctic is 18% greater than the freshwater from the Pacific Ocean through the Bering Strait and is 60% greater than atmospheric sources (Horikawa et al., 2015; Wang et al., 2021). The cold but gradually saltier halocline layer, which is created by the saltier water from the North Atlantic, separates the cold and fresh surface layer from the warmer and saltier Atlantic layer. The Arctic Ocean is considered to be an estuarine system due to the high lateral and vertical gradients. Due to global warming, the river discharge will be increased, and its temperature will be higher. These changes potentially influence sea ice formation and melt. The heat of the Arctic rivers plays a large role in ice formation and melt and is able to affect the estimation of coastal transport pathways.

As for the calculation of the riverine heat fluxes, it is expressed as

$$H = \rho_w C_p T_{river} Q, \quad (1.1)$$

where H is the monthly mean heat flux (Watts), ρ_w is water density (kgm^{-3}), C_p is specific

heat capacity of water ($\text{Jkg}^{-1}\text{°C}^{-1}$), T_{river} is river temperature (°C), and Q is monthly mean river discharge (m^3s^{-1}) (Whitefield et al., 2015; Yang et al., 2013).

The largest source of freshwater input is runoff from rivers around the continental margins of Siberia and North America, amounting to $\approx 4,200 \text{ km}^3\text{yr}^{-1}$ during the period 2000–2010. Net precipitation contributes a further $\approx 2,200 \text{ km}^3\text{yr}^{-1}$ (Haine et al., 2015).

1.2.2 Calculation of Freshwater

In order to estimate the salt-determined stratification and its changes in the Arctic Ocean, several definitions associated with freshwater are introduced first. There are two categories of freshwater: liquid and solid. Generally, freshwater refers to the phase of liquid freshwater since 'sea ice' is equivalent to 'solid phase freshwater'. Freshwater is defined as the volume of pure freshwater needed to add into or be extracted from a water sample to reach a reference salinity (S_{ref}). In the case of the Arctic Ocean, $S_{ref} = 34.8$, which is the averaged salinity of the Arctic Ocean waters (Aagaard and Carmack, 1989). The freshwater content (FWC) is a term used to describe how much freshwater there is within the water column at a given location (x, y) :

$$FW_{content}(x, y) = \int_H^0 1 - \frac{S(x, y, z)}{S_{ref}} dz \quad (1.2)$$

where H is the depth of the water column, $S(x, y, z)$ is the salinity and z is the vertical coordinate.

To calculate the freshwater storage (FWS), the freshwater content is summed up within a given area, e.g., a basin:

$$FW_{storage} = \iiint_H^0 1 - \frac{S(x, y, z)}{S_{ref}} dx dy dz \quad (1.3)$$

In terms of the calculation of the freshwater budget (FWB), it requires the freshwater flux through a section with a length of L :

$$FW_{flux} = \int_0^L \int_H^0 (1 - \frac{S(l, z)}{S_{ref}}) U(l, z) dz dl \quad (1.4)$$

where l is the along section direction, and $U(l, z)$ is the normal to section velocity. It is noted that freshwater (flux, content, and storage) is also a function of time.

1.2.3 Arctic Freshwater System

The Arctic freshwater system is an essential component of the global climate system. Although climate change is ultimately driven by the addition of heat to the Earth's system, the Arctic freshwater system plays a crucial role in this process by influencing global ocean circulation and the hydrological cycle (Carmack and Yamamoto-Kawai, 2018). Additionally, the freshwater system can affect the global atmospheric cycle, which transports water from low to high latitudes. Furthermore, freshwater largely determines the dynamics of Arctic climate change (Peterson et al., 2019).

The Arctic Ocean, located in the high latitudes of the Northern Hemisphere, is a highly stratified ocean with a thin upper freshwater layer of about 300 m, which receives water from various sources, and a lower layer below 300 m that is fed by inflow from the North Atlantic Ocean, the dominant water layer of the Arctic Ocean (Alkire et al., 2017). Previous research has shown that salinity stratification due to freshening in the Arctic Ocean can impact the ocean's dynamic processes, including circulation patterns, freshwater transfer between different regions around the Arctic Ocean, and changes in the dynamic height, which is related to sea surface height. In the Arctic Ocean, salinity is the most important factor in steric height changes. Specifically, a decrease in salinity will increase the surface height of the ocean, while the effects of temperature can be neglected (Steele and Ermold, 2007).

The overall freshwater budget in the Arctic Ocean was first discussed by Aagaard and Carmack (1989), who set the reference for water salinity in the Arctic Ocean at 34.80 psu. Other studies have since followed this salinity reference and updated the budget, including investigations of the freshwater budget in the Arctic Ocean (e.g., Serreze et al., 2006; Dickson et al., 2007). The freshwater budget in the Arctic Ocean has several components, including liquid freshwater and solid freshwater (ice), such as precipitation-less-evaporation, river runoff and glacial runoff. The estimate of freshwater in the Arctic is critical for understanding the physical properties of water in the region. Thus, this section will describe the state of the Arctic freshwater system, its sources and storage, and the mechanisms that control freshwater in the region.

The Arctic Ocean is the smallest and shallowest of the world's five major oceans, and its

freshwater layer is connected to the North Atlantic Ocean by the Canadian Arctic Archipelago (CAA), which contains many narrow straits. Water flows from the Arctic Ocean via CAA to Baffin Bay and then to the Labrador Sea (Kliem and Greenberg, 2003). The sea ice cover floating in the Canadian Arctic is an essential component of the global climate system, with seasonal first-year ice (FYI) and multi-year ice (MYI) that accounts for more than 50% of the ice. Land-fast ice covers many straits of the CAA during winter, which does not move with currents or winds. Investigating freshwater through the Archipelago is critical for understanding physical CAA processes and mapping the best shipping routes from a local and global perspective (Kliem and Greenberg, 2003; Hu et al., 2018).

The Arctic freshwater system is a complex system that results from a combination of factors including latitude, geography, and marine processes. The Arctic Ocean, which has an annual mean liquid freshwater volume of approximately $74,000 \text{ km}^3$ and a sea ice volume of about $10,000 \text{ km}^3$, has experienced significant changes in its freshwater system since 2000 due to a decrease in sea ice volume (Carmack, 2000a). A large portion of the liquid freshwater in the Arctic Ocean is stored in the Beaufort Gyre, due to the strengthening of Ekman pumping caused by the anticyclonic gyre (Haine et al., 2015). Despite the decrease in sea ice volume, the ageing of ice has continued.

Salinity is the dominant factor for density stratification in the Arctic Ocean. In the upper 200 m, the Arctic water volume is relatively fresh due to the inflow of runoff, net precipitation over land (P-ET), and the inflow of the Pacific Water through the Bering Strait. However, the strong density stratification that results from this phenomenon hinders the convection between the upper layer and the warmer, saltier Atlantic waters below, which can lead to the generation of sea ice (Aagaard and Carmack, 1989).

The Arctic freshwater system plays a very important role in global change, especially in the context of climate change. The Earth's climate is determined by the balance between incoming and outgoing radiation. When more energy is absorbed than radiated, the Earth's temperature increases, resulting in global warming. While the addition of heat is the ultimate driver of climate change, the Arctic freshwater system can play a significant role in the Earth's energy budget. The freshwater inputs from the Arctic can modify the physical and chemical properties of the North Atlantic Ocean, which can alter the global ocean circulation and the

hydrological cycle, affecting the Earth’s energy balance and the climate system as a whole (Carmack et al., 2016; Fu et al., 2020).

In addition, freshwater, to a large extent, determines the dynamics of the Arctic climate change. The Arctic is experiencing unprecedented changes in temperature, sea ice cover, and freshwater supply, which have significant impacts on the Arctic ecosystem and the people living in the region. The changes in the Arctic freshwater system can cause a range of ecological and societal impacts, including changes in Arctic sea ice, ocean circulation, fish and wildlife habitats, and Indigenous subsistence activities (Carmack et al., 2016; Solomon et al., 2021; Ananicheva et al., 2011).

Generally, the Arctic freshwater system is a complex and dynamic system that plays a crucial role in the Earth’s climate system. The freshwater inputs from the Arctic can modify the physical and chemical properties of the North Atlantic Ocean, which can alter the global ocean circulation and the hydrological cycle, affecting the Earth’s energy balance and the climate system as a whole. Understanding the Arctic freshwater system is therefore essential for predicting and mitigating the impacts of climate change in the Arctic and beyond.

1.2.4 The Sources and Storage of the Freshwater in the Arctic Ocean

The sources of Arctic freshwater are mainly river runoff, precipitation-less evaporation (P-E), sea-ice melt and Bering Strait inflow from the Pacific Ocean (Aagaard and Carmack, 1989; Serreze et al., 2006). To be specific, the total runoff into the Arctic Ocean is composed of $3558 \text{ km}^3\text{yr}^{-1}$ of water from the mainland, and $711 \text{ km}^3\text{yr}^{-1}$ from the Arctic islands (Carmack, 2000b). The inflows from the Arctic rivers are difficult to calculate practically or theoretically since the river situations vary greatly. There are no standard methods to measure the Arctic rivers, nor are there comparative studies describing the methodology. The inflow of freshwater from the Pacific to the Arctic Ocean via the Bering Strait supplies the halocline and has two water masses called Bering Sea Summer Water (BSSW) and Bering Sea Winter Water (BSWW) (Carmack, 2000b).

1.2.5 Arctic Ocean Freshwater Change

The Arctic freshwater budget is affected by various physical processes and is often attributed to either source or sink of freshwater and surface winds. According to Haine et al. (2015), the timescale for freshwater variances due to source or sink is around 15 years, while the timescale for export changes due to surface winds is on the order of $O(1 - 10)$ months. The surface winds in the Arctic Ocean play a crucial role in controlling the freshwater fluxes and storages. The interaction of the wind with sea ice affects the surface ocean circulation, thereby influencing the export rates and pathways of freshwater. The amount of freshwater stored or exported from the western part of the Arctic, where there is a clockwise Beaufort Gyre, is closely associated with the gyre strength. The freshwater transport controlled by surface winds is more challenging to predict than the freshwater source or sink (Carmack et al., 2012).

The exchange of water between the Arctic Ocean and the Atlantic Ocean is primarily through the Canadian Arctic Archipelago (CAA) and the Fram Strait. The amount of freshwater exchanged between the Arctic Ocean and the Pacific Ocean is limited due to the size of the Bering Strait. In the CAA area, the freshwater transport is mainly in liquid form, while in the Fram Strait, most of the freshwater outflows are in the form of sea ice. The salinity of the water flows from the Atlantic Ocean in the eastern Fram Strait and the Barents Sea is high (35.0 – 35.2), resulting in a sink of Arctic freshwater. The reduction of sea ice in the Arctic Ocean is expected to increase the significance of the CAA to the total freshwater output while decreasing the importance of the Fram Strait near the end of the 21st century, resulting in a significant reduction of convective gyres in the Labrador Sea (Holland et al., 2010). However, recent studies have shown that the increasing meltwater from the Greenland Ice sheet has reduced the freshwater transport from the Arctic Ocean through the CAA into Baffin Bay and can be balanced by a larger freshwater input through the Fram Strait (Castro de la Guardia et al., 2015).

1.3 River Regulation

Rivers serve as an important connection between the land and the ocean, and have a significant impact on the physical characteristics of estuaries and coastal regions where they flow

(Cochran et al., 2019; Broadley et al., 2022). The term "river discharge" is used to refer to the amount of water flowing out of a river, which is a function of runoff (precipitation-minus-evaporation) and the area of the drainage basin. It is typically estimated in cubic meters per second (m^3/s). In order to investigate the freshwater properties of Hudson Bay Complex (HBC), river runoff is an essential factor in model simulations. However, no runoff forcing is provided by the CMIP experiments, and thus external runoff outputs must be considered.

The Arctic-Hydrological Predictions for the Environment (Arctic-HYPE) model was used to provide runoff to the HBC region. This model was forced by the same bias-corrected atmospheric forcing sets used to drive the NEMO simulations described above. Monthly river discharge data for the HBC were produced for each GCM/RCP pair, using the GCM's historical forcing simulation for the period of 1981–2005 and the future simulation for the period of 2006–2070. Two versions of Arctic-HYPE were run for each climate simulation: one naturalized scenario and one that included river regulation (Stadnyk et al., 2021). As such, two sets of 90-year-long hydrological discharge scenarios were produced to drive NEMO, one naturalized and one regulated, for each bias-corrected GCM/RCP pair. In addition, historical WFDEI fields were used to produce naturalized and regulated runoff over the period of 1980–2018 to drive a historical control simulation.

Additional Arctic-HYPE simulations were carried out for the Pan-Arctic domain, again driven by the same 5 bias-corrected GCM/RCP forcing sets for the period of 1980–2070, along with the WFDEI historical forcing over the period of 1980–2018. Due to a lack of detailed information on regulation of Russian rivers, only naturalized output was produced for the Pan-Arctic domain (Stadnyk et al., 2021). For both regions and all simulations, the HYPE output was then regridded from the river mouth positions onto the NEMO model grid using the approach discussed in Hu et al. (2018) and Hayashida et al. (2019).

1.4 Thesis Objectives and Outline

The Earth's climate is now changing faster than at any point in the history of modern civilization, primarily as a result of human activities. Global climate change has already resulted in a wide range of impacts across every region of the country and many sectors of the economy

that are expected to grow in the coming decades.

Thousands of studies conducted by researchers around the world have documented increases in temperature at Earth's surface, as well as in the atmosphere and oceans. Many other aspects of global climate are changing as well. Human activities, especially emissions of heat-trapping greenhouse gases from fossil fuel combustion, deforestation, and land-use change, are the primary driver of the climate changes observed in the industrial era.

In this thesis, the dynamic modelling of the freshwater content, the atmospheric convection, the sea ice properties are studied, responding to the impacts of river regulation and climate change. Interests are mainly focusing on these issues located in the Hudson Bay Complex (HBC). The impacts of global climate change in Canada are already being felt and are projected to intensify in the future, as indicated by our modelling and simulation, if without further action to reduce climate-related risks. As the impacts of climate change grow, we face decisions about how to respond to the change.

There are three research questions for this thesis to focus on:

- Under the circumstance of climate change, how would the ocean and ice properties respond?
- What effects would exist if river regulation, defined as controlling rivers to meet human demands for domestic and industrial water supplies, is applied in the five simulated climate runs?
- How does atmospheric forcing variability affect the ocean, sea ice, and the atmosphere itself?

This thesis comprises five chapters, consisting of an introduction and model description, a specific study, and at last the summary and discussion part. The model description is presented in chapter 2. The experiment setup and a method helping to remap the river runoff on the ocean model grid of NEMO is discussed in Chapter 3. The upper ocean properties including freshwater content, heat content, sea ice thickness and concentration, mixed layer depth, and the atmospheric forcing fields such as surface air temperature, mean precipitation, net heat flux and wind speed can be found in Chapter 4. In addition, a summary and discussion of possible future work are illustrated in the final part of Chapter 5.

Bibliography

- Aagaard, K., and E. C. Carmack, 1989: The role of sea ice and other fresh water in the arctic circulation. *Journal of Geophysical Research: Oceans*, **94 (C10)**, 14 485–14 498.
- Alkire, M. B., J. Morison, A. Schweiger, J. Zhang, M. Steele, C. Peralta-Ferriz, and S. Dickinson, 2017: A meteoric water budget for the arctic ocean. *Journal of Geophysical Research: Oceans*, **122 (12)**, 10 020–10 041.
- Ananicheva, M., and Coauthors, 2011: *Snow, water, ice and permafrost in the Arctic (SWIPA): climate change and the cryosphere*. Arctic Monitoring and Assessment Programme (AMAP).
- Andrews, J., D. Babb, D. G. Barber, and S. F. Ackley, 2018: Climate change and sea ice: shipping in hudson bay, hudson strait, and foxe basin (1980–2016). *Elementa: Science of the Anthropocene*, **6**.
- Andrews, J., D. Babb, M. McKernan, B. Horton, and D. Barber, 2016: Climate Change in the Hudson Bay Complex: Opportunities and Vulnerabilities for the Port of Churchill’s Marine Operations. Tech. rep., University of Manitoba, Centre for Earth Observation Science.
- Babb, D., J. Andrews, J. Dawson, D. Landry, O. Mussells, and M. Weber, 2019: Transportation and community use of the marine environment. *From science to policy in the Greater Hudson Bay Marine Region: An Integrated Regional Impact Study (IRIS) of climate change and modernization*, 341–377.
- Braun, M., A. N. Thiombiano, M. J. F. Vieira, and T. A. Stadnyk, 2021: Representing climate evolution in ensembles of GCM simulations for the Hudson Bay system. *Elementa: Science of the Anthropocene*, **9 (1)**.
- Broadley, A., B. Stewart-Koster, M. A. Burford, and C. J. Brown, 2022: A global review of the critical link between river flows and productivity in marine fisheries. *Reviews in Fish Biology and Fisheries*, **32 (3)**, 805–825.
- Carmack, E., 2000a: Freshwater and its role in the arctic marine system: Sources, disposition,

- storage, export, and physical and biogeochemical consequences in the arctic and global oceans. *Journal of geophysical research: Oceans*, **105 (C7)**, 16 603–16 624.
- Carmack, E., and M. Yamamoto-Kawai, 2018: The role of sea ice and other fresh water in the arctic circulation. *Journal of Geophysical Research: Oceans*, **123 (3)**, 1846–1866.
- Carmack, E. C., 2000b: The arctic ocean’s freshwater budget: Sources, storage and export. *The freshwater budget of the Arctic Ocean*, 91–126.
- Carmack, E. C., and Coauthors, 2012: Freshwater and its role in the arctic marine system: Sources, disposition, storage, export, and physical and biogeochemical consequences in the arctic and global oceans. *Journal of Geophysical Research: Biogeosciences*, **117 (G1)**.
- Carmack, E. C., and Coauthors, 2016: Freshwater and its role in the Arctic Marine System: Sources, disposition, storage, export, and physical and biogeochemical consequences in the Arctic and global oceans. *Journal of Geophysical Research: Biogeosciences*, **121 (3)**, 675–717.
- Castro de la Guardia, L., X. Hu, and P. G. Myers, 2015: Potential positive feedback between Greenland Ice Sheet melt and Baffin Bay heat content on the west Greenland shelf. *Geophysical Research Letters*, **42 (12)**, 4922–4930.
- Cochran, J. K., H. J. Bokuniewicz, and P. L. Yager, 2019: *Encyclopedia of ocean sciences*. Academic Press.
- Déry, S. J., T. J. Mlynowski, M. A. Hernández-Henríquez, and F. Straneo, 2011: Interannual variability and interdecadal trends in hudson bay streamflow. *Journal of Marine Systems*, **88 (3)**, 341–351.
- Déry, S. J., T. A. Stadnyk, M. K. MacDonald, and B. Gaudi-Sharma, 2016: Recent trends and variability in river discharge across northern Canada. *Hydrology and Earth System Sciences*, **20 (12)**, 4801–4818.
- Dickson, R., B. Rudels, S. Dye, M. Karcher, J. Meincke, and I. Yashayaev, 2007: Current estimates of freshwater flux through arctic and subarctic seas. *Progress in oceanography*, **73 (3-4)**, 210–230.

- Drinkwater, K., 1986: Physical oceanography of hudson strait and ungava bay. *Elsevier oceanography series*, Vol. 44, Elsevier, 237–264.
- Dunbar, M., 1982: Oceanographic research in hudson and james bays. *Naturaliste Canadien*, **109 (4)**, 677–683.
- Fu, W., J. K. Moore, F. W. Primeau, K. Lindsay, and J. T. Randerson, 2020: A growing freshwater lens in the Arctic Ocean with sustained climate warming disrupts marine ecosystem function. *Journal of Geophysical Research: Biogeosciences*, **125 (12)**, e2020JG005693.
- Grivault, N., X. Hu, and P. G. Myers, 2018: Impact of the surface stress on the volume and freshwater transport through the Canadian Arctic Archipelago from a high-resolution numerical simulation. *Journal of Geophysical Research: Oceans*, **123 (12)**, 9038–9060.
- Haine, T. W., and Coauthors, 2015: Arctic freshwater export: Status, mechanisms, and prospects. *Global and Planetary Change*, **125**, 13–35.
- Hamilton, A., 2013: The Hudson Bay Complex in flux: contemplating the future of the world’s largest seasonally ice-covered inland sea. Tech. rep., IISD (International Institute for Sustainable Development).
- Hayashida, H., and Coauthors, 2019: Csib v1 (canadian sea-ice biogeochemistry): a sea-ice biogeochemical model for the NEMO community ocean modelling framework. *Geoscientific Model Development*, **12 (5)**, 1965–1990.
- Holland, M. M., C. M. Bitz, L. B. Tremblay, D. A. Bailey, and M. J. Behrenfeld, 2010: Future abrupt reductions in the summer arctic sea ice. *Geophysical Research Letters*, **37 (16)**.
- Horikawa, K., and Coauthors, 2015: Pliocene cooling enhanced by flow of low-salinity Bering Sea water to the Arctic Ocean. *Nature Communications*, **6 (1)**, 7587.
- Houser, C., and W. A. Gough, 2003: Variations in sea ice in the hudson strait: 1971-1999. *Polar Geography*, **27 (1)**, 1–14.
- Hu, X., J. Sun, T. O. Chan, and P. G. Myers, 2018: Thermodynamic and dynamic ice thickness

- contributions in the Canadian Arctic Archipelago in NEMO-LIM2 numerical simulations. *The Cryosphere*, **12** (4), 1233–1247.
- Ingram, R. G., and P. Larouche, 1987: Variability of an under-ice river plume in hudson bay. *Journal of Geophysical Research: Oceans*, **92** (C9), 9541–9547.
- JafariKhasragh, S., J. V. Lukovich, X. Hu, P. G. Myers, K. Sydor, and D. G. Barber, 2019: Modelling sea surface temperature (SST) in the Hudson Bay Complex using bulk heat flux parameterization: Sensitivity to atmospheric forcing, and model resolution. *Atmosphere-Ocean*, **57**, 120–133.
- Kliem, N., and D. A. Greenberg, 2003: Diagnostic simulations of the summer circulation in the canadian arctic archipelago. *Atmosphere-ocean*, **41** (4), 273–289.
- Kuzyk, Z., and L. Candlish, 2019: From science to policy in the greater hudson bay marine region: An integrated regional impact study (iris) of climate change and modernization. *ArcticNet, Québec City*, 424.
- Lavoie, D., N. Lambert, and A. van der Baaren, 2013: Projections of future physical and biogeochemical conditions in Hudson and Baffin bays from CMIP5 Global Climate Models. Tech. rep., Fisheries and Oceans Canada Pelagic and Ecosystem Science Branch Maurice Lamontagne Institute.
- Lukovich, J. V., and Coauthors, 2021: Simulated impacts of relative climate change and river discharge regulation on sea ice and oceanographic conditions in the hudson bay complex. *Elem Sci Anth*, **9** (1), 00 127.
- McCullough, G., and Coauthors, 2019: Freshwater–marine interactions in the greater hudson bay marine region. *From science to policy in the Greater Hudson Bay Marine Region: An Integrated Regional Impact Study (IRIS) of climate change and modernization. Québec City, Québec, Canada: ArcticNet*, 155–197.
- McKinney, M. A., S. Pedro, R. Dietz, C. Sonne, A. T. Fisk, D. Roy, B. M. Jenssen, and R. J. Letcher, 2015: A review of ecological impacts of global climate change on persistent

- organic pollutant and mercury pathways and exposures in arctic marine ecosystems. *Current Zoology*, **61** (4), 617–628.
- Perovich, D. K., and J. A. Richter-Menge, 2009: Loss of sea ice in the Arctic. *Annual review of marine science*, **1**, 417–441.
- Peterson, B. J., J. W. McClelland, R. Curry, R. M. Holmes, J. E. Walsh, and K. Aagaard, 2019: Trajectory of the arctic as an integrated system. *Ecological Applications*, **29** (6), e01980.
- Prinsenbergh, S., 1988: Ice-cover and ice-ridge contributions to the freshwater contents of hudson bay and foxe basin. *Arctic*, 6–11.
- Ridenour, N. A., X. Hu, K. Sydor, P. G. Myers, and D. G. Barber, 2019: Revisiting the circulation of hudson bay: Evidence for a seasonal pattern. *Geophysical Research Letters*, **46** (7), 3891–3899.
- Serreze, M. C., and Coauthors, 2006: The large-scale freshwater cycle of the arctic. *Journal of Geophysical Research: Oceans*, **111** (C11).
- Solomon, A., and Coauthors, 2021: Freshwater in the Arctic Ocean 2010–2019. *Ocean Science*, **17** (4), 1081–1102.
- Stadnyk, T. A., S. J. Déry, M. K. MacDonald, and K. Kristina, 2019: The freshwater system. *From Science to Policy in the Greater Hudson Bay Marine Region: An Integrated Regional Impact Study (IRIS) of Climate Change and Modernization*, ArcticNet, 113–154.
- Stadnyk, T. A., and Coauthors, 2021: Changing freshwater contributions to the Arctic: A 90-year trend analysis (1981–2070). *Elem Sci Anth*, **9** (1), 00098.
- Steele, M., and W. Ermold, 2007: Steric sea level change in the northern seas. *Journal of Climate*, **20** (3), 403–417.
- Stewart, D., and W. Lockhart, 2005: An overview of the Hudson Bay marine ecosystem. Tech. rep., Central and Arctic Region Fisheries and Oceans Canada.

- Wang, Q., S. Danilov, D. Sidorenko, and X. Wang, 2021: Circulation pathways and exports of Arctic river runoff influenced by atmospheric circulation regimes. *Frontiers in Marine Science*, 1153.
- Whitefield, J., P. Winsor, J. McClelland, and D. Menemenlis, 2015: A new river discharge and river temperature climatology data set for the pan-Arctic region. *Ocean Modelling*, **88**, 1–15.
- Yang, D., P. Marsh, and S. Ge, 2013: Calculation and analysis of Yukon River heat flux. *IAHS-AISH publication*, **360**, 113–117.

Chapter 2

An Ocean-Ice Coupled Model: Nucleus for European Modelling of the Ocean (NEMO)

The ocean engine of Nucleus for European Modelling of the Ocean (NEMO) is a state-of-the-art framework for oceanographic research, operational oceanography, seasonal forecasting and climate studies. It includes five major components, the blue ocean (Océan PARallélisé (OPA) for the ocean dynamics and thermodynamics), the white ocean (Louvain-la-Neuve (LIM) for the sea-ice dynamics and thermodynamics), the green ocean (Tracer in the Ocean Paradigm (TOP) for the biogeochemistry), the adaptive mesh refinement software and the assimilation component (Madec and the NEMO team, 2008; Madec et al., 2017). The official documentation and announcements of NEMO are available from <http://www.nemo-ocean.eu/>. As we study mainly on oceanic and ice properties, the details of ocean and sea-ice components will be described in this chapter. In this thesis, the NEMO version 3.6 from Madec and the NEMO team (2008) is applied to all experiments.

2.1 Ocean Component

The ocean component in the NEMO framework has been developed from the OPA model, which has both global and regional applications. This model can be applied as a forced model and as sea-ice or/and the atmosphere coupling model (Madec et al., 1998, 2017). In OPA, the ocean is described as a set of primitive equations in a curvilinear coordinate system with six assumptions as follows:

- Boussinesq Approximation

In this approximation, a constant value of density (e.g., ρ_0) is used to stand for the 'background density' in equations except the term of density that involved in the buoyancy force. In other word, density variations matter only in Buoyancy term.

- Hydrostatic Approximation

The vertical momentum equation is represented by a balance between vertical pressure gradient and the buoyancy (gravitational) force, which is known as hydrostatic balance. This approximation is mathematically written as:

$$\frac{\partial P}{\partial z} = -\rho g \quad (2.1)$$

Hydrostatic approximation is valid as horizontal oceanic flow is far faster than vertical flow. However, this approximation is inapplicable during convective processes, where the velocity scales in the horizontal and vertical are similar. Thus, in convective processes, vertical accelerations must be parameterized.

- Incompressibility Approximation

If the seawater is incompressible, its density (ρ) is constant following a controlled volume along motion. Thus,

$$\frac{D\rho}{Dt} = 0 \quad (2.2)$$

The continuity equation is given by:

$$\frac{\partial \rho}{\partial t} + \nabla \cdot (\rho \mathbf{U}) = 0 \quad (2.3)$$

From Equation 2.2 and 2.3, it turns out a zero divergence velocity field, which is written as:

$$\nabla \cdot \mathbf{U} = 0 \quad (2.4)$$

where $\nabla = (\frac{\partial}{\partial x}, \frac{\partial}{\partial y}, \frac{\partial}{\partial z})$, \mathbf{U} is the three-dimensional (3D) velocity.

- Spherical Earth Approximation

The geopotential surfaces are assumed to be spheres, so that local vertical gravity is parallel to the Earth's radius. The gravitational acceleration g used in the model is set to be a constant,

9.8 ms^{-2} .

- Thin-shell Approximation

The water depth of ocean can be ignored compared to the Earth's radius. This is because the Earth's radius is 6400 km while the mean ocean depth is much smaller, only 4 km up to ~ 11 km. Hence, the distance from any location in the ocean, representing as points on grid in the model, to the center of the Earth is assumed as a constant value (the Earth's radius).

- Turbulent Closure Hypothesis

An instantaneous flow can be decomposed into its mean motion (time mean flow) and relative motion (turbulent flow) (Reynolds, 1895). The system of equations is written as:

$$\rho \left(\frac{\partial \mathbf{v}}{\partial t} + \mathbf{v} \cdot \nabla \mathbf{v} \right) = -\nabla p + \mu \Delta \mathbf{v} + \rho \mathbf{F} \quad (2.5)$$

where, typically, the body force \mathbf{F} is the weight of the fluid. This system is called the Navier-Stokes (NS) equations.

There are always more unknown turbulent fluxes terms than the number of the equations when we employ the Reynolds averaging on the NS equations (Equation 2.5), which cannot close the whole system (Stull, 1988). To solve this problem, eliminating the unknown variables, the turbulent fluxes, which stand for the effect of small scale processes on the large-scale, are expressed in terms of large-scale features.

2.1.1 Primitive Equations

A curvilinear coordinate system with a horizontal plane represented by unit vectors \mathbf{i} and \mathbf{j} , and a vertical direction represented by a local upward vector \mathbf{k} (Figure 2.1) is used in the OPA model for ocean dynamics and thermodynamics. Taking the above six assumptions into account, the set of six primitive equations is shown below (namely the horizontal equation of motion, the hydrostatic equilibrium, the incompressibility equation, the heat conservation,

the salt conservation, and the equation of state of ocean),

$$\frac{\partial \mathbf{U}_h}{\partial t} = \overbrace{\left[(\nabla \times \mathbf{U}) \times \mathbf{U} + \frac{1}{2} \nabla (\mathbf{U}^2) \right]_h}^{\text{Inertia force}} - \overbrace{f \mathbf{k} \times \mathbf{U}_h}^{\text{Coriolis force}} - \overbrace{\frac{1}{\rho} \nabla_h p}^{\text{Pressure gradient force}} + \overbrace{D^{\mathbf{U}} + F^{\mathbf{U}}}^{\text{small-scale parametrizations + surface forces}} \quad (2.6a)$$

$$\frac{\partial p}{\partial z} = \overbrace{-\rho g}^{\text{Hydrostatic balance}} \quad (2.6b)$$

$$\nabla \cdot \mathbf{U} = \overbrace{0}^{\text{Incompressibility}} \quad (2.6c)$$

$$\frac{\partial T}{\partial t} = \overbrace{-\nabla \cdot (T\mathbf{U})}^{\text{Heat divergence}} + \overbrace{D^T + F^T}^{\text{small-scale parametrizations + surface forces}} \quad (2.6d)$$

$$\frac{\partial S}{\partial t} = \overbrace{-\nabla \cdot (S\mathbf{U})}^{\text{Salt divergence}} + \overbrace{D^S + F^S}^{\text{small-scale parametrizations + surface forces}} \quad (2.6e)$$

$$\rho = \overbrace{\rho(T, S, p)}^{\text{Equation of state of the ocean}} \quad (2.6f)$$

where $D^{\mathbf{U}}, D^T, D^S$ are the parametrizations of small-scale physics for momentum, temperature and salinity, and $F^{\mathbf{U}}, F^T, F^S$ are the surface forcing terms, S is the salinity, T is the potential temperature, ρ is the density derived from Equation 2.6f, ρ_0 is a reference density, p is the pressure, $g = 9.8 \text{ ms}^{-2}$ is the gravitational acceleration, and $f = 2\Omega \sin\varphi$ is the Coriolis parameter (Ω is the Earth's angular velocity and φ is the latitude). The velocity vector is given by $\mathbf{U} = \mathbf{U}_h + w\mathbf{k}$, where $\mathbf{U}_h = (U, V)$ is the horizontal velocity over the (\mathbf{i}, \mathbf{j}) plane, w is the vertical velocity in the direction of \mathbf{k} .

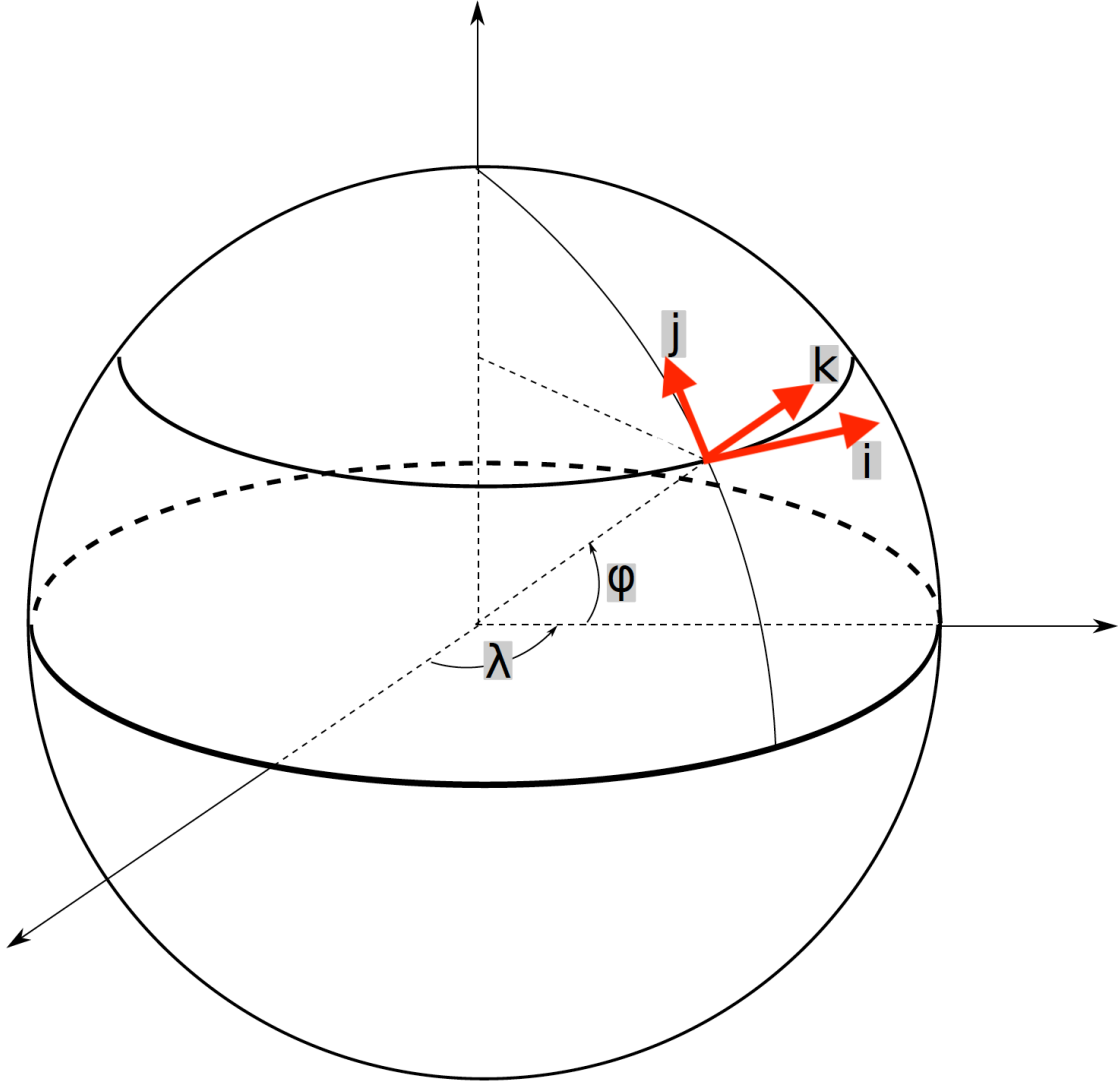


Figure 2.1: The spherical coordinate system is used in NEMO. The horizontal unit vectors, \mathbf{i} and \mathbf{j} (in red), orthogonal to each other, are described by λ and φ . The vertical upward vector (which is perpendicular to the horizontal plan of (\mathbf{i}, \mathbf{j})) is shown as \mathbf{k} (in red).

2.1.2 Boundaries

In the OPA model, there are three boundaries of the ocean, including an interface between the ocean and atmosphere or the ocean and sea ice, irregular lateral coastlines, and topography in the deep ocean, which can be found in Figure 2.2. The expressions of the top and bottom interface of the ocean are $z = \eta(i, j, k, t)$ and $z = -H(i, j)$, respectively. η is the height of the sea surface and is allowed to change over time. H is the depth of the sea floor. Both H and η are referenced to $z = 0$, where $z = 0$ is set to the mean sea surface.

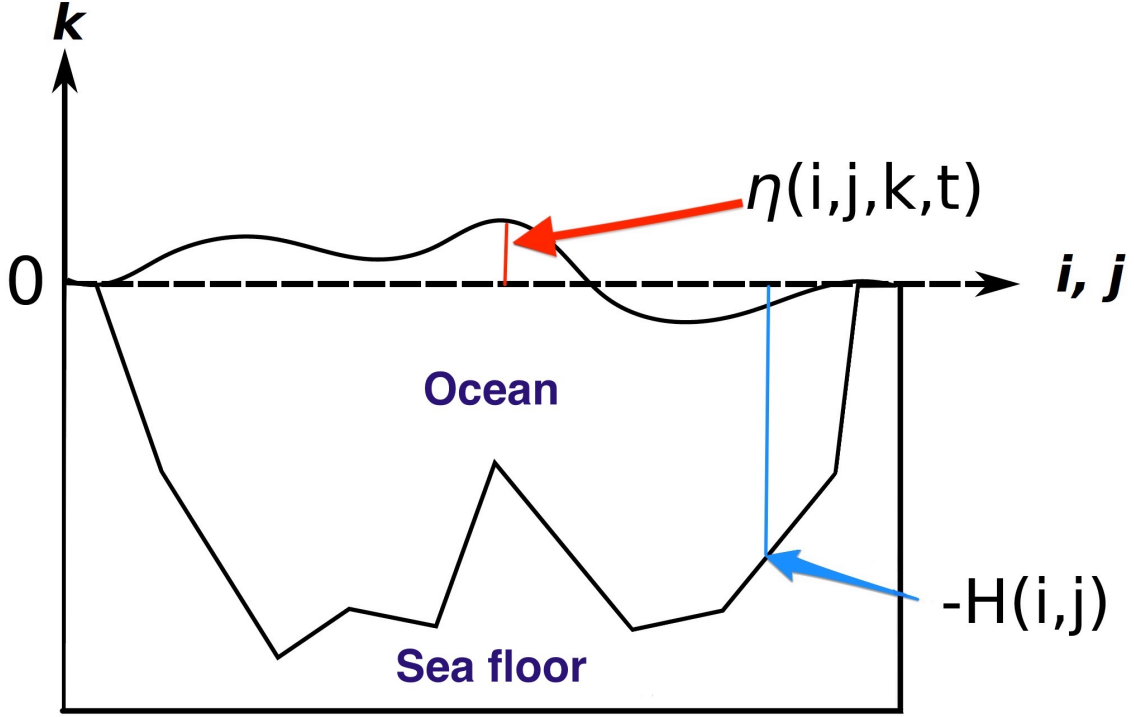


Figure 2.2: The surface and bottom boundaries of the ocean in NEMO. The sea floor boundary is defined as $z = -H(i, j)$ and the ocean surface boundary is defined as $z = \eta(i, j, k, t)$, where η is the height of the sea surface and is allowed to change over time. Both H and η are referenced to the mean sea surface, $z = 0$.

The fluxes of the heat and salt at the bottom of the ocean are small (Huang, 1999) and can be ignored in the model, which means there is no flux of heat and salt across solid boundaries. For the momentum transfer, the situation is different that there is no flow crossing the solid boundaries. In specific, the velocity normal to the sea floor and coastlines is zero. Thus, the bottom velocity is parallel to these boundaries. This kinematic boundary condition for the bottom of ocean is written as:

$$w|_{z=-H} = -\mathbf{U}_h \cdot \nabla H \quad (2.7)$$

At the ocean surface, the exchanges of freshwater, heat, salt, and momentum need to be considered. Based on the mass balance and these exchanges, there is a displacement of the ocean surface boundary governed by the kinematic surface condition, which includes all the dynamic effects:

$$w|_{z=\eta} = \frac{\partial \eta}{\partial t} + \mathbf{U}_h \cdot \nabla_h \eta|_{z=\eta} - (P - E + R + I) \quad (2.8)$$

where P , E , R , and I are total precipitation, evaporation, runoff, and ice growth or melt fluxes, respectively.

The prognostic equation of η ($\frac{\partial\eta}{\partial t}$) can be derived by vertical integration of the continuity equation (2.6c) applying the surface (2.8) and bottom (2.7) kinematic conditions, which is written mathematically as:

$$\frac{\partial\eta}{\partial t} = (P - E + R + I) - \nabla \cdot [(H + \eta)\overline{\mathbf{U}}_h] \quad (2.9)$$

where the vertical averaged horizontal velocity is defined as $\overline{\mathbf{U}}_h = \frac{1}{H+\eta} \int_{-H}^{\eta} \mathbf{U}_h dz$.

After the above simplicities of the dynamic boundary condition, a free surface displacement is applied in the model. However, this displacement can result in the generation of external gravity waves (EGWs), which are regarded as high frequency noise in our experiments. To solve this numerical stability problem, a linear filtered free surface model (Roullet and Madec, 2000) is employed, where an additional forcing term is introduced in the momentum equation (2.6a) to dampen the EGWs:

$$\frac{\partial\mathbf{U}_h}{\partial t} = \mathbf{M} - g\nabla(\tilde{\rho}\eta) - gT_c\nabla\left(\tilde{\rho}\frac{\partial\eta}{\partial t}\right) \quad (2.10)$$

where \mathbf{M} includes the contributions of the hydrostatic pressure gradient, Coriolis force, non-linear and viscous terms in (2.6a). T_c is a parameter characterizing the force with units of time (Roullet and Madec, 2000) and $\tilde{\rho} = \rho/\rho_0$ is the dimensionless density.

Free-slip is applied to the lateral boundary condition in the OPA model. The most appropriate boundary condition for the primitive equations (the NS equations) is regarded as the no-slip boundary condition (Gjesteland and Svård, 2022; Prabhakara and Deshpande, 2004; Deremble et al., 2011; Foreman and A.F., 1988). However, researchers like Deremble et al. (2011) also concluded that the drag-slip boundary condition of NS equations share more similarities with the free-slip boundary condition than the standard no-slip boundary condition.

In this thesis, the definition of friction is in terms of modifying the turbulent fluxes using bottom and lateral boundary conditions, which is called a non-linear quadratic boundary friction and a free-slip lateral boundary condition. To simulate runoff in our model, no heat is transferred from the coastline but freshwater enters into the ocean. The assumption is that all runoff is fresh (0 psu) and is distributed equally within the river column. The representation of runoff is a salt flux, which means the dilution of salt within the ocean exists the runoff.

2.1.3 Curvilinear Coordinate System and Spatial Discretization

In terms of the spatial discretization in ocean models, a set of orthogonal curvilinear coordinates are applied. As shown in the figure (2.1), the upward \mathbf{k} , which is paralleled to the Earth's radius, is set to be the z -axis, and the horizontal plane (x, y) has its unit vectors (\mathbf{i}, \mathbf{j}) that is perpendicular to \mathbf{k} . It is note that the direction of the horizontal axis (x, y) can be arbitrary as long as they are perpendicular to each other. The reason why the x -axis and y -axis are not set to respectively along with the latitude and longitude lines is that a spherical coordinate singularity near to the North and South poles will be generated, where the meridians convergent. (e.g., Murray, 1996; Madec and Imbard, 1996; Roberts et al., 2006; Williamson, 2007; Prusa, 2018; Bénard and Glinton, 2019). A rotated or re-projected grid is widely applied in global or polar regional ocean models to move the singularity from poles to land. Therefore, a re-projected horizontal grid is used following the tri-pole transformation described in Murray (1996).

A staggered horizontal Arakawa C grid is used for the re-projected horizontal grid (Mesinger and Arakawa, 1976; Haidvogel and Beckmann, 1999). Other kinds of Arakawa grids compared to C-grid are shown in figure (2.3). The points of scalar variables (T, S, p, ρ) are placed in the middle of cell and vector points (U, V, W) are located in the center of cell faces, where $\mathbf{U} = (U, V, W)$ (Figure 2.4). The planetary and relative vorticity, f and ζ , and the barotropic stream function ψ are defined on the center of each vertical edge (\mathbf{F} point on Figure 2.4). The dimensions of each grid cell are formed by two horizontal scale factors, e_1 and e_2 , which are aligned with \mathbf{i} -axis and \mathbf{j} -axis, respectively, and one vertical scale factor, e_3 , which is associated to the k -axis (Figure 2.4A). e_1 , e_2 , and e_3 are defined as the width, length, and height of each grid cell, respectively. Therefore, the partial derivatives can be given in a uniform mesh with a grid size of unity mathematically as:

$$\nabla q = \frac{1}{e_1} \frac{\partial q}{\partial i} \mathbf{i} + \frac{1}{e_2} \frac{\partial q}{\partial j} \mathbf{j} + \frac{1}{e_3} \frac{\partial q}{\partial k} \mathbf{k} \quad (2.11a)$$

$$\nabla \cdot \mathbf{A} = \frac{1}{e_1 e_2} \left[\frac{\partial(e_2 a_1)}{\partial i} + \frac{\partial(e_1 a_2)}{\partial j} \right] + \frac{1}{e_3} \frac{\partial a_3}{\partial k} \quad (2.11b)$$

$$\begin{aligned}
\nabla \times \mathbf{A} &= \begin{pmatrix} \mathbf{i} & \mathbf{j} & \mathbf{k} \\ \frac{\partial}{e_1 \partial i} & \frac{\partial}{e_2 \partial j} & \frac{\partial}{e_3 \partial k} \\ a_1 & a_2 & a_3 \end{pmatrix} \\
&= \left[\frac{1}{e_2} \frac{\partial a_3}{\partial j} - \frac{1}{e_3} \frac{\partial a_2}{\partial k} \right] \mathbf{i} \\
&\quad + \left[\frac{1}{e_3} \frac{\partial a_1}{\partial k} - \frac{1}{e_1} \frac{\partial a_3}{\partial i} \right] \mathbf{j} \\
&\quad + \frac{1}{e_1 e_2} \left[\frac{\partial e_2 a_2}{\partial i} - \frac{\partial e_1 a_1}{\partial j} \right] \mathbf{k}
\end{aligned} \tag{2.11c}$$

$$\Delta q = \nabla \cdot (\nabla q) \tag{2.11d}$$

$$\Delta \mathbf{A} = \nabla(\nabla \cdot \mathbf{A}) - \nabla \times (\nabla \times \mathbf{A}) \tag{2.11e}$$

where q stands for a scalar variable, and $\mathbf{A} = (a_1, a_2, a_3)$ is a vector in the curvilinear coordinate system (i, j, k) .

In NEMO, we use a second order centered finite difference method is applied, which is given as the form of:

$$\frac{\partial f}{\partial x} = \frac{f_{i+1} - f_{i-1}}{2\Delta x} + O(\Delta x^2). \tag{2.12}$$

or for second derivative, we have:

$$\frac{\partial^2 f}{\partial x^2} = \frac{f_{i+1} - 2f_i + f_{i-1}}{\Delta x^2} + O(\Delta x^2). \tag{2.13}$$

In the vertical direction, the thickness of almost every layer in the z-coordinate system is set as default values except the depths related to the bottom of the ocean. In this area, the z-coordinate with partial steps (Bernard et al., 2006), which represents the structure of sea floor better than traditional z-coordinate (Figure 2.5) is used in NEMO. Although the traditional z-coordinate method appears more accurate and clear when calculating the pressure gradient, it shows bad performance in representing the topography (Figure 2.5, left). In other words, it poorly resolves the bottom bathymetry of the ocean. Other than the traditional approach where the vertical column is separated into fixed thickness everywhere, the partial-step z-coordinate method allows variable thicknesses for the bottom level cells (Figure 2.5, right).

By using the partial steps, the sea floor can witness a better representation in the model and such approach remains the advantages of the traditional z-coordinate, such as the simplified calculations of pressure gradient.

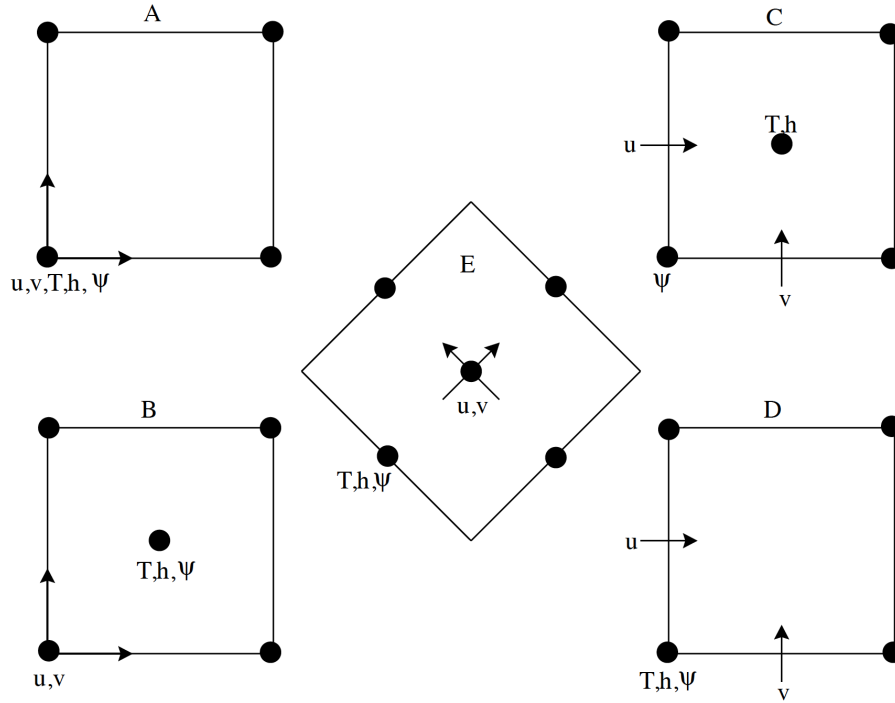


Figure 2.3: Schematic of the placement of model variables on the staggered horizontal Arakawa grids used in ocean models. T refers to tracer and density, $u; v$ refer to horizontal velocity components, h refers to layer thickness, and ψ refers to horizontal streamfunction or surface height. This figure is from Fig. 3.1 of Haidvogel and Beckmann (1999).

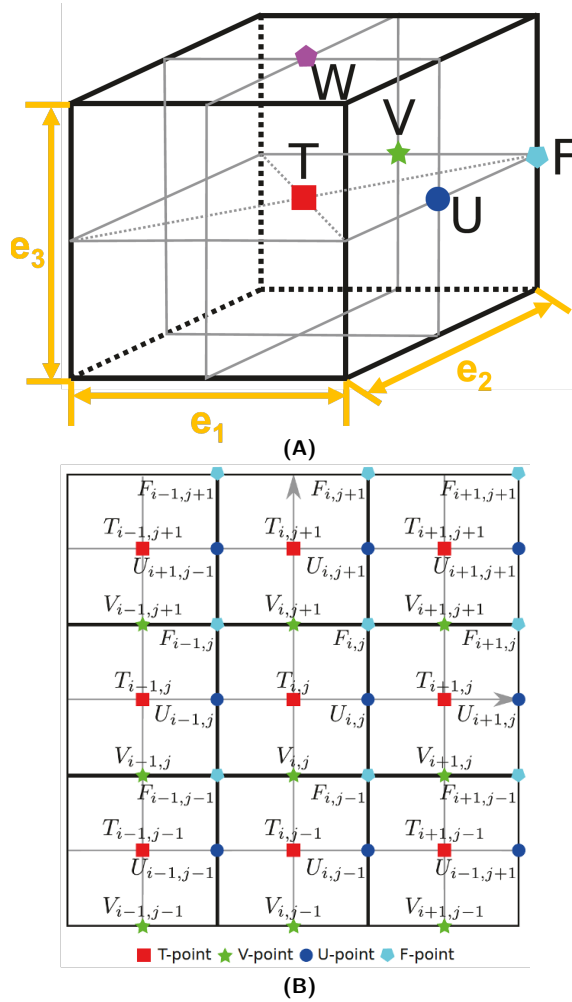


Figure 2.4: 3D (A) and 2D (B) over the horizontal plane representation of a C-grid cell in the NEMO with every computed variable. $\mathbf{T} = (T, S, p, \rho)$ is a vector containing scalar variables, shown by the red squares in the core of each cell. F shown by light blue pentagons represents vorticity. $\mathbf{U} = (U, V, W)$ is the vector of velocity, whose three components are represented by blue circles, green pentagons, and purple pentagons respectively. The size of each grid cell is defined by three local scale factors, e_1 , e_2 , and e_3 , shown in (A).

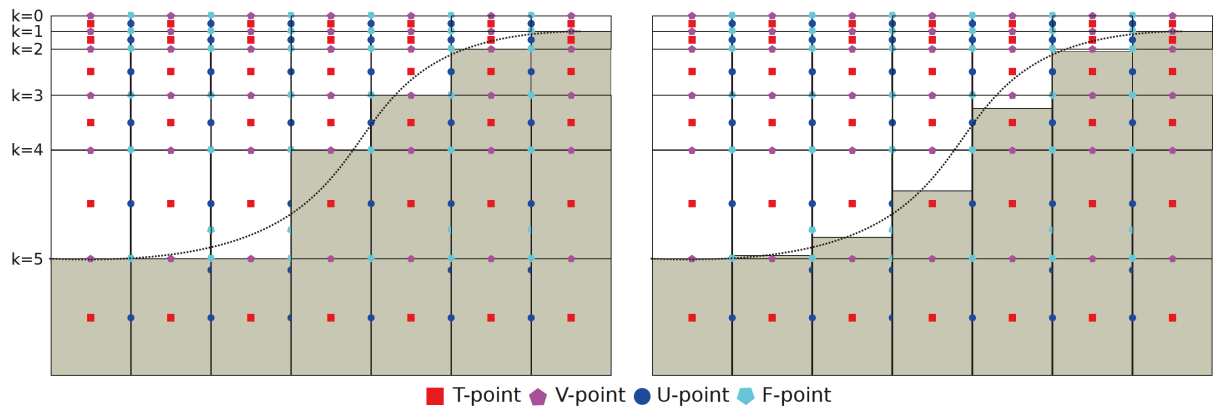


Figure 2.5: Vertical grid of traditional z-coordinate with full steps (left) and z-coordinate with partial steps (right) in model. Dash lines represent the real bathymetry of ocean and shaded cells show the simulated bathymetry in the model.

2.1.4 Subgrid Scale Physics

The primitive equations are used to show the performance of a geophysical fluid both in space and time, with a horizontal range larger than a few kilometres, a vertical range larger than a few meters, and the time for a few minutes. However, for those smaller scale turbulent motions, coming from the advective terms in the NS equations, the above resolution is insufficient. These relative small-scale processes play important roles in larger scale oceanic dynamic and thermodynamic quantities. A parameterization method is generally used to associate such small scale motions with resolved larger scale fields, so that the subgrid scale (SGS) physics can be presented in models and the equations can be closed as well. The SGS terms ($D^{\mathbf{U}}$, D^S , D^T) in primitive equations (2.6a, 2.6d and 2.6e) are divided into vertical components $D^{v\mathbf{U}}$, D^{vS} , D^{vT} and horizontal components $D^{l\mathbf{U}}$, D^{lS} , D^{lT} .

The vertical components of the turbulent fluxes are assumed to be linearly dependent on the gradients of large-scale quantities, which is a similar form to that of molecular diffusion and dissipation. In our model, the vertical expressions of momentum, temperature, and salinity are:

$$D^{v\mathbf{U}} = \frac{\partial}{\partial z} \left(A^{vm} \frac{\partial \mathbf{U}_h}{\partial z} \right) \quad (2.14)$$

$$D^{vT} = \frac{\partial}{\partial z} \left(A^{vT} \frac{\partial T}{\partial z} \right) \quad (2.15)$$

$$D^{vS} = \frac{\partial}{\partial z} \left(A^{vT} \frac{\partial S}{\partial z} \right) \quad (2.16)$$

where A^{vm} and A^{vT} represent the vertical eddy viscosity diffusivity coefficients, respectively. A^{vm} and A^{vT} are constants, with values of $1 \times 10^{-4} m^2 s^{-1}$ and $1 \times 10^{-5} m^2 s^{-1}$, under non-turbulent conditions. For turbulent conditions, the two coefficients are computed via the scheme of vertical turbulent fluxes, which will be introduced in the following part. As the scales of vertical motions are much smaller than that of the vertical grid spacing, the vertical acceleration is a parametrized quantity.

Under the conditions of turbulence, the vertical eddy viscosity and diffusivity coefficients are calculated using a turbulent kinetic energy (TKE) scheme according to initial conditions

(Gaspar et al., 1990; Blanke and Delecluse, 1993; Madec et al., 1997; Witek et al., 2011; Zhang et al., 2018). The turbulent closure model is established based on the TKE scheme ($\bar{\epsilon}$), which can be expressed as:

$$\bar{\epsilon} = \frac{1}{2} \left(\overline{u'^2} + \overline{v'^2} + \overline{w'^2} \right) \quad (2.17)$$

$$\frac{\partial \bar{\epsilon}}{\partial t} = \frac{A^{vm}}{e_3} \left[\left(\frac{\partial u}{\partial k} \right)^2 + \left(\frac{\partial v}{\partial k} \right)^2 \right] - A^{vT} N^2 + \frac{1}{e_3} \frac{\partial}{\partial k} \left(\frac{A^{vm}}{e_3} \frac{\partial \bar{\epsilon}}{\partial k} \right) - c_\epsilon \frac{\bar{\epsilon}^{-\frac{3}{2}}}{l_\epsilon} \quad (2.18)$$

$$A^{vm} = c_k l_k \sqrt{\bar{\epsilon}} \quad (2.19)$$

$$A^{vT} = \frac{A^{vm}}{P_{rt}} \quad (2.20)$$

where u', v' and w' are the velocity turbulent components of the flow, k represents the vertical direction, $N = \sqrt{-\frac{g}{\rho_\sigma} \frac{d\rho}{dz}}$ is the local Brunt-Vaisälä (buoyancy) frequency, $c_\epsilon = \sqrt{2}/2$ and $c_k = 0.1$ are two constants, $P_{rt} = \frac{\nu}{\alpha}$ is the Prandtl number (a function of local Richardson number, R_i), the dissipation (l_ϵ) and mixing length (l_k) scales are estimated as:

$$l_k = l_\epsilon = \frac{\sqrt{2\bar{\epsilon}}}{N} \quad (2.21)$$

$$\frac{1}{e_3} \left| \frac{\partial l}{\partial k} \right| \leq 1 \text{ with } l = l_k = l_\epsilon$$

For the horizontal components (or along isopycnals), a Laplacian operator ($\nabla \cdot \nabla$) is used for both temperature and salinity diffusion (z-coordinates), which is defined by:

$$D^{lT} = \nabla \cdot (\mathbf{A}^{lT} \mathfrak{R} \nabla T) \text{ with } \mathfrak{R} = \begin{pmatrix} 1 & 0 & -r_1 \\ 0 & 1 & -r_2 \\ -r_1 & -r_2 & r_1^2 + r_2^2 \end{pmatrix} \quad (2.22)$$

where T stands for the tracer (temperature and salinity), r_1 and r_2 represent the slopes between the surface along which the diffusive operator acts and the model vertical level (e.g. z- or s-surfaces). In the case of z-coordinate, the above slopes are all zeros, that is, $r_1 = r_2 = 0$.

Equation 2.22 can then be simplified into the following form:

$$D^{lT} = \frac{1}{e_1 e_2} \left[\frac{\partial}{\partial i} \left(\frac{e_2}{e_1} A^{lT} \frac{\partial T}{\partial i} \Big|_z \right) \Big|_z + \frac{\partial}{\partial j} \left(\frac{e_1}{e_2} A^{lT} \frac{\partial(T)}{\partial j} \Big|_z \right) \Big|_z \right] \quad (2.23)$$

A Laplacian operator on a vector could be separated into the divergent and rotational parts of the flow (see details in appendix). The horizontal divergence is given by:

$$\chi = \nabla \cdot \mathbf{U}_h = \frac{1}{e_1 e_2} \left[\frac{\partial(e_2 u)}{\partial i} + \frac{\partial(e_1 v)}{\partial j} \right] \quad (2.24)$$

The rotational part (relative vorticity) is defined as:

$$\zeta = \nabla \times \mathbf{U} \cdot \mathbf{k} = \frac{1}{e_1 e_2} \left[\frac{\partial(e_2 v)}{\partial i} - \frac{\partial(e_1 u)}{\partial j} \right] \quad (2.25)$$

The horizontal second order diffusion is given as:

$$D^l \mathbf{U} = \Delta_h (A^{lm} \mathbf{U}) \quad (2.26)$$

$$= \nabla_h (\nabla_h \cdot A^{lm} \mathbf{U}_h) + \Delta_h \times (\Delta_h \times A^{lm} \mathbf{U}_h) \quad (2.27)$$

$$= \nabla_h (A^{lm} \chi) + \Delta_h \times (A^{lm} \zeta \mathbf{k}) \quad (2.28)$$

$$= \begin{pmatrix} \frac{1}{e_1} \frac{\partial(A^{lm} \chi)}{\partial i} - \frac{1}{e_2 e_3} \frac{\partial(A^{lm} e_3 \zeta)}{\partial j} \\ \frac{1}{e_2} \frac{\partial(A^{lm} \chi)}{\partial j} - \frac{1}{e_1 e_3} \frac{\partial(A^{lm} e_3 \zeta)}{\partial i} \end{pmatrix} \quad (2.29)$$

A fourth order (bilaplacian) operator is used for the momentum diffusion in the configuration of this thesis, rather than a second order operator. In practice, a bilaplacian operator is done by applying the second order operator twice (Equation 2.26).

2.1.5 Time Discretization

The calculation of the result of equations will go to the next time step when the equations are solved in space (\mathbf{i} , \mathbf{j} and \mathbf{k}). To ensure the movement of a virtual particle, which is induced by the fluid velocity, being less than one grid cell in each time step, the value (in seconds) of time step has to be set carefully. This condition is called Courant-Friedrichs-Lewy (CFL) condition, which is given as:

$$C = \frac{u \Delta t}{e_1} + \frac{v \Delta t}{e_2} < C_{max} \quad (2.30)$$

where, u and v are the largest velocities in the \mathbf{i} and \mathbf{j} direction. This above equation should satisfy less than $C_{max} = 1$. According to the close relationship between the resolution of the spatial discretization and time steps, we often choose $\Delta t = 1080s$ and $180s$ for the horizontal resolution of $1/4^\circ$ or $1/12^\circ$, respectively in our model.

The time step we use in NEMO is a three level scheme, which is expressed as:

$$x^{t+\Delta t} = x^{t-\Delta t} + 2\Delta t RHS_x^{t-\Delta t, t, t+\Delta t} \quad (2.31)$$

where x is the prognostic variable (u, v, T or S), RHS stands for the Right-Hand-Side of the corresponding time evolution equation, Δt is the time step, and the superscripts indicate the time level at which the variable is evaluated.

During the non-diffusive processes, including the Coriolis, momentum and tracer advection, and pressure gradient terms (Equation 2.6a), the Leapfrog scheme (Mesinger and Arakawa, 1976), which has second-order accuracy, is used for the time stepping (a time centered scheme as shown in Figure 2.6). For one dimension, it is an explicit centered in time and centered in space (CTCS) finite difference formula of an advection equation $\frac{\partial f}{\partial t} = c \frac{\partial f}{\partial x}$ as follows:

$$\frac{f_j^{n+1} - f_j^{n-1}}{2\Delta t} + \frac{f_{j+1}^n - f_{j-1}^n}{2\Delta x} = 0 \quad (2.32)$$

However, the disadvantage of using Leapfrog scheme is the differencing decouples odd and even grid points at any given time step. To prevent the computational mode, a Robert-Asselin time filter (Robert, 1966; Asselin, 1972) with the Leapfrog scheme is applied, mixing the odd and even time steps. The Robert-Asselin time filter is defined as:

$$x_F^t = x^t + \gamma[x_F^{t-\Delta t} - 2x^t + x^{t+\Delta t}] \quad (2.33)$$

where F denotes the filtered values and γ is the Asselin filter coefficient. In the simulated experiments, γ is set to 0.1.

For diffusive processes, such as tracer restoring and horizontal diffusion terms, Leapfrog scheme can not be used because all the coefficients of even derivative terms are zero. Also this CTCS scheme will be unconditionally unstable. Instead, a forward or backward (implicit)

time differencing scheme is employed. The forward time discretization scheme is given by:

$$x^{t+\Delta t} = x^{t-\Delta t} + 2\Delta t D_x^{t-\Delta t} \quad (2.34)$$

where D indicates the diffusive term.

Based on Griffies (2018), the following conditions must be satisfied for numerical stability:

$$A_h < \begin{cases} \frac{e^2}{8\Delta t} & \text{laplacian diffusion} \\ \frac{e^4}{64\Delta t} & \text{bilaplacian diffusion} \end{cases} \quad (2.35)$$

where A_h is the coefficient of mixing and e is the size of the largest horizontal grid. As we focus on $1/4^\circ$ horizontal resolution, a baroclinic time step with the value of 1080 s is used. In our simulations, the largest grid cell is 27,799.7 m. Applying Equation 2.35, the upper bound for A_h is then $A_h < 8.94 \times 10^4 \text{ m}^2/\text{s}$ for Laplacian diffusion, and $A_h < 8.64 \times 10^{12} \text{ m}^4/\text{s}$ for bilaplacian diffusion. The lower bound to A_h is determined by model stability. Similarly, the values for $1/12^\circ$ horizontal resolution are $5.26 \times 10^4 \text{ m}^2/\text{s}$ for Laplacian diffusion and $4.98 \times 10^{11} \text{ m}^4/\text{s}$ for bilaplacian diffusion.

For vertical diffusion, an implicit (backward) time differencing scheme, which is unconditionally stable, is used, and is expressed as:

$$x^{t+\Delta t} = x^{t-\Delta t} + 2\Delta t RHS_x^{t+\Delta t} \quad (2.36)$$

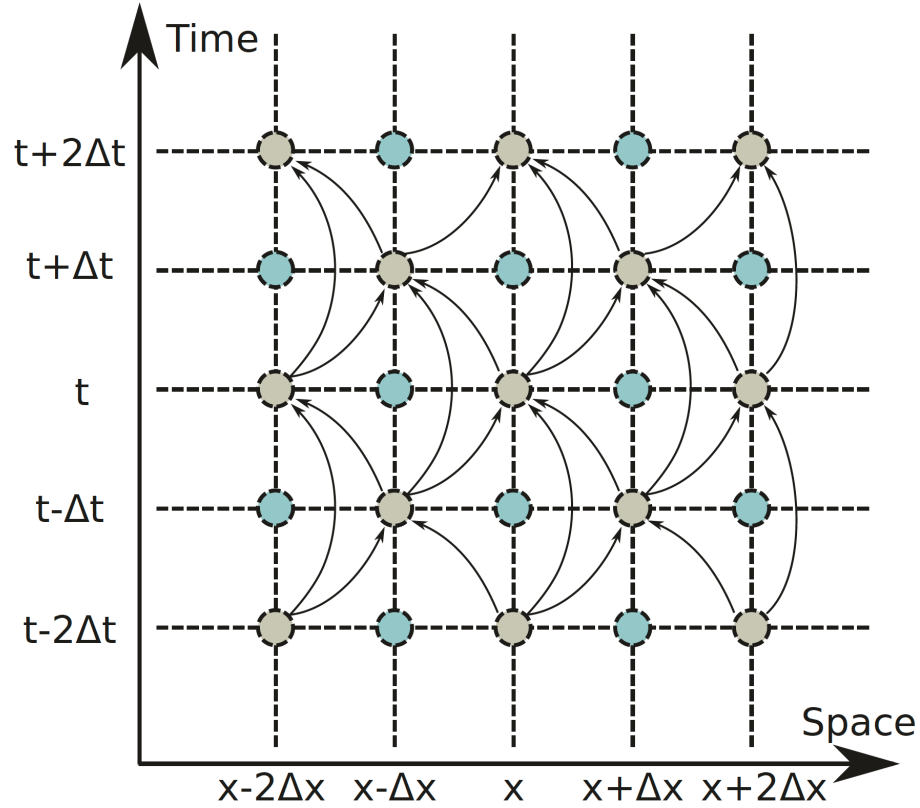


Figure 2.6: Temporal and spatial pattern of the time stepping in the Leapfrog scheme is used for non-diffusive processes. Inputs from different time and space steps are shown by the terminal points of arrows, while the points of using output as input are shown by the beginning of arrows.

2.2 Sea-Ice Component

In NEMO, the Louvain-la-Neuve sea-Ice Model version 2 (LIM2; Fichefet and Maqueda, 1997) is the sea ice model used in this thesis. LIM2 is a C-grid dynamic-thermodynamic sea ice model. It is based on a three-layer ice model (Semtner Jr, 1976), including a snow layer on the top, and the other two ice layers with equal thickness below. The internal stress of ice is computed based on a theory of elastic-viscous-plastic (EVP) rheology (Hunke and Dukowicz, 1997). For the description of this model, more information can be available in Semtner Jr (1976); Fichefet and Maqueda (1997). Additionally, for readers who are interested in, descriptions about the latest Louvain-la-Neuve sea-Ice Model version 3 (LIM3) can be found in Rousset et al. (2015); Buchart (2021).

2.2.1 Sea-Ice Dynamics

The sea ice is assumed to move in a two-dimensional (2D) plane with a momentum balance defined by:

$$m \frac{\partial \mathbf{u}}{\partial t} = \underbrace{A(\tau_a + \tau_w)}_{\text{Atmospheric forcing}} - \underbrace{mf\mathbf{k} \times \mathbf{u}}_{\text{Coriolis}} - \underbrace{mg\nabla\eta}_{\text{Pressure}} + \underbrace{\nabla \cdot \sigma}_{\text{Internal stress}} \quad (2.37)$$

where m is the mass of per unit area of snow and ice, A is the ice concentration, τ_a and τ_w are the atmosphere-ice and water-ice interfacial stresses, g, f, η and \mathbf{k} are the acceleration of gravity, the Coriolis parameter, the sea surface height and vertical upwards unit vector, respectively. $\nabla \cdot \sigma$ is the internal stress term.

The air and water stress terms (τ_a and τ_w , where a stands for 'air' and w stands for 'water') are calculated from the input wind data and ocean currents from simulations, following the two formulas:

$$\tau_a = \rho_a C_a |\mathbf{u}_a| \mathbf{u}_a \quad (2.38a)$$

$$\tau_w = \rho_w C_w |\mathbf{u}_w - \mathbf{u}_i| (\mathbf{u}_w - \mathbf{u}_i) \quad (2.38b)$$

where \mathbf{u}_i is the ice velocity, \mathbf{u}_a is the surface wind velocity (typically at 10m height), \mathbf{u}_w is the surface layer ocean velocity, C_a and $C_w = 0.0055$ stand for the air and ocean drag coefficients, ρ_w is the seawater density. The CORE bulk formula can produce the air drag coefficient (Large and Yeager, 2004). From the content of Thorndike (1986), the advective momentum can be neglected under the condition of large time scale (more than 30 minutes) in the model. The approximation of equation (2.37) is applied in the sea-ice model.

The force due to sea ice internal stress is given by the divergence of the stress tensor σ . The internal horizontal stress tensor is defined as:

$$\nabla_h \cdot \sigma = \left(\frac{\partial \sigma_1}{\partial i}, \frac{\partial \sigma_2}{\partial j} \right) \quad (2.39)$$

Here, σ_1 and σ_2 are the principal direction of the internal stress. Thus, with the EVP approach, we have:

$$\sigma_1 = \sigma_{11} + \sigma_{22} \quad (2.40a)$$

$$\sigma_2 = \sigma_{11} - \sigma_{22} \quad (2.40b)$$

$$D_D = \frac{1}{e_1 e_2} \left(\frac{\partial(e_2 u)}{\partial i} + \frac{\partial(e_1 v)}{\partial j} \right) = \epsilon_{i1} + \epsilon_{j2} \quad (2.40c)$$

$$D_T = \frac{1}{e_1 e_2} \left(e_2^2 \frac{\partial(u/e_2)}{\partial i} - e_1^2 \frac{\partial(v/e_1)}{\partial j} \right) = \epsilon_{i1} - \epsilon_{j2} \quad (2.40d)$$

$$D_S = \frac{1}{e_1 e_2} \left(e_1^2 \frac{\partial(u/e_1)}{\partial j} - e_2^2 \frac{\partial(v/e_2)}{\partial i} \right) = 2\epsilon_{i2} \quad (2.40e)$$

where ϵ_{i1} , ϵ_{i2} , and ϵ_{j2} are from the symmetric strain rate tensor matrix that can be found in Hunke (2001). D_D is the sea-ice divergence, D_T is the horizontal tension strain rate, D_S is shearing strain rate, and in the EVP rheology of Hunke and Dukowicz (1997), there are:

$$2T_e \frac{\partial \sigma_1}{\partial t} + \sigma_1 = \left(\frac{D_D}{\nabla} - 1 \right) P \quad (2.41a)$$

$$\frac{2T_e}{e^2} \frac{\partial \sigma_2}{\partial t} + \sigma_2 = \frac{D_T}{e^2 \Delta} P \quad (2.41b)$$

$$\frac{2T_e}{e^2} \frac{\partial \sigma_{12}}{\partial t} + \sigma_{12} = \frac{D_S}{2e^2 \Delta} P \quad (2.41c)$$

$$\Delta = \sqrt{D_D^2 + \frac{1}{e^2}(D_T^2 + D_S^2)} \quad (2.41d)$$

where T_e is an elastic time scale (this term needs to be small enough to damp the elastic waves), e is the eccentricity of the ice elliptical curve, describing the relation of the two principal components of a two dimensional stress tensor, and Δ is the deformation rate. P is the ice compressive strength given by a function of mean ice thickness (h) and concentration (A),

$$P = P^* h e^{-C_{reh}(1-A)} \quad (2.42)$$

where $P^* = 5000 \text{ N m}^{-2}$ and $C_{reh} = 20$ are two empirical constants, and h is sea-ice thickness.

In each equation (2.41), compared to the viscous-plastic (VP) rheology (Hibler, 1979), an additional time dependent artificial elastic term introduces a split time step to the ice model, updating the ice stress on a short time step and resolving the elastic wave velocity. There are lots of numerical computation advantages for using EVP equations. For instance, it allows a fully explicit discretization (Hunke and Dukowicz, 1997).

2.2.2 Sea-Ice Thermodynamics

Ice thermodynamics are the processes associated with the heat exchanging through or stored in the sea ice. The processes are concerned with the sea-ice growth and melt (vertical and lateral evolution) in LIM2. More thermodynamics processes of creation of new ice in open water, basal ice growth, ice melt at the air and ocean interfaces, snow-ice formation, brine drainage, and ice ageing are described in the LIM3 (Rousset et al., 2015; Buchart, 2021).

2.2.2.1 Vertical Growth and Decay

To determine rates of decay or growth in subsequent steps and calculate the conductive heat flux (Q_c) in the vertical (z), a one-dimensional heat diffusion equation is used to describe the conduction and storage of energy in the system (Fichefet and Maqueda, 1997):

$$\rho c_p \frac{\partial T}{\partial t} = Gk \frac{\partial^2 T}{\partial z^2} \quad (2.43)$$

where T is the temperature, t is the time, G is a correction factor applied to transfer the variations of heat conduction to the corresponding variations of ice thickness (Fichefet and Maqueda, 1997). ρ , k and c_p denote the ice/snow density, thermal conductivity, and the specific heat accordingly.

There are five components of the snow-ice surface heat flux balance (B_{si}), a function of surface temperature T_{su} , including sensible heat (Q_h), latent heat (Q_{le}), conductive heat (Q_c) from below, shortwave solar radiation (Q_{sw}), and longwave radiation (Q_{lw}). The heat budget is expressed as:

$$B_{si}(T_{si}) = Q_{sw} + Q_{lw} + Q_h + Q_{le} + Q_c \quad (2.44)$$

where T_{si} is a temperature function at the surface.

In terms of the first four quantities in Equation 2.44, they are calculated from bulk formula provided by Large and Yeager (2004) as follows:

$$Q_{sw} = (1 - i_0)(1 - \alpha)Q_{ds} \quad (2.45a)$$

$$Q_{lw} = \epsilon(Q_{dl} - \sigma SST^4) \quad (2.45b)$$

$$Q_h = \rho_a c_p C_h (T_a - SST) |\mathbf{u}_a - \mathbf{u}_o| \quad (2.45c)$$

$$Q_{le} = \rho_a L_e C_e (q - q_s) |\mathbf{u}_a - \mathbf{u}_o| \quad (2.45d)$$

where i_0 is the fraction of net shortwave radiation that penetrates the snow-ice, α is the ocean albedo, ϵ is the emissivity, Q_{ds} and Q_{dl} are the downwelling shortwave and longwave flux from the atmosphere, T_a and q are the near surface (10m) atmosphere temperature and specific humidity, q_s is the specific humidity, a function of sea surface temperature (SST), at the ocean surface, $\sigma = 5.67 \times 10^{-8} W m^{-2} K^{-4}$ is the Stefan-Boltzmann constant, $L_e = 2.5 \times 10^6 J kg^{-1}$ is the latent heat of vaporization of water, C_h, C_e are the transfer coefficients of sensible heat and latent heat, respectively. The excess of energy will be applied for ice or snow melting when the surface temperature T_{sf} is larger than the melting point. The mathematical expression is:

$$\left(\frac{\partial h_*}{\partial t} \right)_{surface} = \frac{B_{si}}{L_*} \quad (2.46)$$

where the ice or snow thickness is represented as h_* , L is the volumetric latent heat of fusion. The subscript $*$ represents the snow (s) if it exists, otherwise it represents the ice (i).

At the interface between sea ice and ocean, for example on the bottom of an ice slab, the ice transformation (formation or melting) can be produced by utilizing any imbalance in energy between the conductive heat flux ($Q_{c,bot}$) and heat flux from the ocean (Q_{oi}), and this process follows:

$$\left(\frac{\partial h_i}{\partial t} \right)_{oi} = \frac{Q_{c,bot} - Q_{oi}}{L_i} \quad (2.47)$$

Therefore, ice growth occurs when $Q_{c,bot} - Q_{oi} > 0$.

2.2.2.2 Lateral Growth and Decay

There is another important ice quantity, sea ice concentration (A), which is closely related to the lateral growth and decay of the sea ice. Mathematically, it is defined as a fraction of the grid cell area covered by ice. The evolution of A is associated with the heat flux budget from the open water (B_l):

$$\frac{\partial A}{\partial t} = \sqrt{1 - A^2} \frac{(1 - A) B_l}{L_i h_0} \quad (2.48)$$

where h_0 is the ice thickness formed in a polynya or on the side of the ice floe. When B_l is positive, ice melting occurs from below through Q_{oi} in Equation 2.47, otherwise there is a

formation of sea ice.

2.2.3 Ocean-Ice Coupling

The sea ice influences the upper ocean temperature, salt and momentum fluxes. For instance, at the ocean surface, the shortwave radiation fluxes (Q_{swoc}) with sea ice cover can be written as:

$$Q_{swoc} = AQ_{str} + (1 - A)(1 - \alpha_w)Q_{ds} \quad (2.49a)$$

$$Q_{str} = i_0(1 - \alpha)Q_{ds}e^{-1.5(h_i-0.1)} \quad (2.49b)$$

where Q_{str} is the amount of shortwave radiation reaching the bottom of an ice slab, and α_w is the open water albedo.

Generally, there is a well-mixed layer on the top of the ocean, which is named the 'mixed layer' (ML). Within this layer, the assumptions of the vertical homogeneous temperature (T_m) and salinity (S_m) will be made. Considering the thermodynamic balance with the existence of ice, the temperature of the ML is set to the freezing point (T_{fw} , a function of ML salinity). Hence, the net heat gain of the ML must be balanced by the sensible heat flux from the ocean to the ice (Q_{oi}):

$$Q_{oi} = (1 - i_w|_{z=-h_m})Q_{str} + \Gamma \left[\frac{(1 - A)B_l}{A} \right] + Q_{ent} + Q_{dif} + Q_{ovT}|_{z=-h_m} + Q_{fus} \quad (2.50)$$

where h_m is the mixed layer depth (MLD), the part of net shortwave radiation penetrating the ocean is given as i_w , which is a function of z . Γ is the Heaviside unit function, the last four terms on the righthand side (RHS) of Equation 2.50 (Q_{ent} , Q_{dif} , $Q_{ovT}|_{z=-h_m}$, and Q_{fus}) are the heat fluxes due to entrainment, diffusion, overturning and changes in salinity, respectively. The ocean mixed layer model computes the last four terms on the RHS.

The heat flux budget of the leads, such as polynyas, (B_l) in equation (2.50) is expressed as:

$$B_l = (1 - i_w|_{z=-h_m})(1 - \alpha_w)Q_{sw} \quad (2.51)$$

$$+ \exp_w(Q_{lw} - \sigma T_m^4) \quad (2.52)$$

$$+ Q_h + Q_{le} + Q_{lsi} - Q_{lpr} \quad (2.53)$$

$$+ Q_{ent} + Q_{dif} + Q_{ovT}|_{z=-h_m} + Q_{fus} \quad (2.54)$$

where Q_{lsi} and Q_{lpr} are the latent heat released during snow/ice formation and snow falling onto the ocean, respectively, and \exp_w is the ocean water emissivity.

Apart from the heat fluxes, the ice or snow also has influences on the salt flux at the surface of ocean into the ML. The surface salt flux is given as:

$$\begin{aligned} Q_{salt} = & \underbrace{S_m \frac{\partial m_s}{\partial t}}_{\text{snow melt}} + \underbrace{(S_m - S_i) \frac{\partial m_i}{\partial t}}_{\text{ice melt}} \\ & + \underbrace{(S_m - S_i) \left(\frac{\partial m_s}{\partial t} + \frac{\partial m_i}{\partial t} \right)}_{\text{salt rejection}} + \underbrace{S_i \frac{\partial m_s}{\partial t}}_{\text{artificial meteoric ice}} \\ & + \underbrace{S_m (AE - P_w)}_{\text{evaporation \& precipitation}} \end{aligned} \quad (2.55)$$

where P_w is the freshwater change from the total precipitation, E is the evaporation rate over the leads and polynyas, m_i and S_i are the mass and salinity of ice, and m_s is the snow mass per unit area. Here, the influence of ice/snow formation is taken into account by the salt rejection term. In addition, to add salinity into the meteoric ice, the term of artificial meteoric ice is considered in Equation 2.55.

Bibliography

- Asselin, R., 1972: Frequency filter for time integrations. *Monthly Weather Review*, **100** (6), 487–490.
- Bénard, P., and M. R. Ginton, 2019: Circumventing the pole problem of reduced lat–lon grids with local schemes. Part I: Analysis and model formulation. *Quarterly Journal of the Royal Meteorological Society*, **145** (721), 1377–1391.
- Bernard, B., and Coauthors, 2006: Impact of partial steps and momentum advection schemes in a global ocean circulation model at eddy-permitting resolution. *Ocean dynamics*, **56** (5), 543–567.
- Blanke, B., and P. Delecluse, 1993: Variability of the tropical Atlantic Ocean simulated by a general circulation model with two different mixed-layer physics. *Journal of Physical Oceanography*, **23** (7), 1363–1388.
- Buchart, L., 2021: Sea Ice Modelling in the Pikialasorsuaq: Parameters Sensitivities and Future Prospects. M.S. thesis, Department of Earth and Atmospheric Science, University of Alberta.
- Deremble, B., A. McC. Hogg, P. Berloff, and W. Dewar, 2011: On the application of no-slip lateral boundary conditions to ‘coarsely’ resolved ocean models. *Ocean Modelling*, **39** (3), 411–415.
- Fichefet, T., and M. M. Maqueda, 1997: Sensitivity of a global sea ice model to the treatment of ice thermodynamics and dynamics. *Journal of Geophysical Research: Oceans*, **102** (C6), 12 609–12 646.
- Foreman, M., and B. A.F., 1988: On no-slip boundary conditions for the incompressible Navier-Stokes equations. *Dynamics of Atmospheres and Oceans*, **12** (1), 47–70.
- Gaspar, P., Y. Grégoris, and J.-M. Lefevre, 1990: A simple eddy kinetic energy model for simulations of the oceanic vertical mixing: Tests at station Papa and Long-Term Upper Ocean Study site. *Journal of Geophysical Research: Oceans*, **95** (C9), 16 179–16 193.

- Gjesteland, A., and M. Svård, 2022: Entropy stability for the compressible Navier-Stokes equations with strong imposition of the no-slip boundary condition. *Journal of Computational Physics*, **470**, 111–572.
- Griffies, S., 2018: *Fundamentals of ocean climate models*. Princeton university press.
- Haidvogel, D. B., and A. Beckmann, 1999: *Numerical ocean circulation modeling*. World Scientific.
- Hibler, W. D., 1979: A dynamic thermodynamic sea ice model. *Journal of physical oceanography*, **9** (4), 815–846.
- Huang, R. X., 1999: Mixing and energetics of the oceanic thermohaline circulation. *Journal of Physical Oceanography*, **29** (4), 727–746.
- Hunke, E. C., 2001: Viscous–plastic sea ice dynamics with the EVP model: Linearization issues. *Journal of Computational Physics*, **170** (1), 18–38.
- Hunke, E. C., and J. K. Dukowicz, 1997: An elastic–viscous–plastic model for sea ice dynamics. *Journal of Physical Oceanography*, **27** (9), 1849–1867.
- Large, W. G., and S. G. Yeager, 2004: Diurnal to decadal global forcing for ocean and sea-ice models: The data sets and flux climatologies. National Center for Atmospheric Research Boulder.
- Madec, G., P. Delecluse, M. Imbard, and C. Levy, 1997: Ocean general circulation model reference manual. *Note du Pôle de modélisation*.
- Madec, G., P. Delecluse, M. Imbard, and C. Levy, 1998: OPA 8 Ocean General Circulation Model - Reference Manual. Tech. rep., LODYC/IPSL Note 11.
- Madec, G., and M. Imbard, 1996: A global ocean mesh to overcome the North Pole singularity. *Climate Dynamics*, **12** (6), 381–388.
- Madec, G., and the NEMO team, 2008: NEMO ocean engine. Project report, *Note du Pôle de modélisation*, Institut Pierre-Simon Laplace (IPSL), France. No 27, ISSN No 1288-1619.

- Madec, G., and Coauthors, 2017: NEMO ocean engine. Zenodo.
- Mesinger, F., and A. Arakawa, 1976: *Numerical methods used in atmospheric models*, Vol. 17. Global Atmospheric Research Programme (GARP).
- Murray, R. J., 1996: Explicit generation of orthogonal grids for ocean models. *Journal of Computational Physics*, **126** (2), 251–273.
- Prabhakara, S., and M. Deshpande, 2004: The no-slip boundary condition in fluid mechanics. *Resonance*, **9** (5), 61–71.
- Prusa, J., 2018: Computation at a coordinate singularity. *Journal of Computational Physics*, **361**.
- Reynolds, O., 1895: IV. On the dynamical theory of incompressible viscous fluids and the determination of the criterion. *Philosophical Transactions of the Royal Society of London. (A.)*, **186**, 123–164.
- Robert, A. J., 1966: The integration of a low order spectral form of the primitive meteorological equations. *Journal of the Meteorological Society of Japan. Ser. II*, **44** (5), 237–245.
- Roberts, J. L., P. Heil, R. J. Murray, D. S. Holloway, and N. L. Bindoff, 2006: Pole relocation for an orthogonal grid: an analytic method. *Ocean Modelling*, **12** (1-2), 16–31.
- Roullet, G., and G. Madec, 2000: Salt conservation, free surface, and varying levels: a new formulation for ocean general circulation models. *Journal of Geophysical Research: Oceans*, **105** (C10), 23 927–23 942.
- Rousset, C., and Coauthors, 2015: The Louvain-La-Neuve sea ice model LIM3. 6: global and regional capabilities. *Geoscientific Model Development*, **8** (10), 2991–3005.
- Semtner Jr, A. J., 1976: A model for the thermodynamic growth of sea ice in numerical investigations of climate. *Journal of Physical Oceanography*, **6** (3), 379–389.
- Stull, R. B., 1988: *An introduction to boundary layer meteorology*, Vol. 13. Springer Science & Business Media.

- Thorndike, A. S., 1986: Kinematics of sea ice. *The geophysics of sea ice*, Springer, 489–549.
- Williamson, D., 2007: The Evolution of Dynamical Cores for Global Atmospheric Models. *J. Royal Met. Soc. Japan*, **85B**, 241–269.
- Witek, M. L., J. Teixeira, and G. Matheou, 2011: An Eddy Diffusivity–Mass Flux Approach to the Vertical Transport of Turbulent Kinetic Energy in Convective Boundary Layers. *Journal of the Atmospheric Sciences*, **68 (10)**, 2385–2394.
- Zhang, X., J.-W. Bao, B. Chen, and E. D. Grell, 2018: A Three-Dimensional Scale-Adaptive Turbulent Kinetic Energy Scheme in the WRF-ARW Model. *Monthly Weather Review*, **146 (7)**, 2023–2045.

Chapter 3

Experiment Setup

3.1 Numerical Modelling of the Ocean and Sea Ice

Numerical ocean modeling is a widely used computational approach that aims to simulate the interactions between the ocean and atmosphere and to provide a better understanding of the properties of the ocean. This method is based on the physical and mathematical representation and parameterization of the complex geophysical system related to climate and the ocean. Three different types of vertical coordinates, including z -coordinates, isopycnal ρ -coordinates, and σ -coordinates, are used in these models with different Arakawa grids. However, there is no standard vertical coordinate system, which results in the use of mixed modeling techniques. The Coordinated Ocean-Ice Reference Experiments (CORE) framework serves as a common reference for scientists to develop and evaluate global ocean-ice models (Griffies et al., 2009).

Numerical modeling of ocean properties provides a valuable tool for oceanographers to gain insights into the underlying mechanics of ocean phenomena. The evaluation of the results from numerical models typically involves comparing simulated results with observations over long time scales, under the same atmospheric forcing conditions. The choice of diagnostics depends on the research goals and can vary greatly. The resolution, parameterization, and parameters used in the models can also greatly impact the results.

The placement of factors such as tracer, density, layer thickness, and surface height in the models can vary depending on the grid used. The B grid is commonly used in coarse-resolution models, while the C grid is typically employed in high-resolution models. The B grid performs well in simulating geostrophic processes, while the C grid, which is more dependent on the

high resolution of the velocity field, provides better resolution for wave measurement. Z-models tend to perform well with the B grid, while models related to density often use the C grid. The representation of Rossby waves or boundary waves can also differ significantly between the B and C grid (Griffies et al., 2000).

Numerical modeling is essential in the study of the Arctic Ocean and the Canadian Arctic Archipelago (CAA) due to limited observations in these regions. Modeling helps to interpret observed data and gain a deeper understanding of the physical processes in the CAA. For example, quantifying and estimating the variance of sea ice in the CAA is critical for validating future predictions of ice conditions, including ice melting and break-up potential. Furthermore, numerical simulations can provide valuable information for planning shipping routes and seasons along the Northwest Passage (NWP).

However, the modeling process in the CAA can be challenging due to the sparse observations available for validation and the complex topography in the region. Studies have shown that sea-ice models often lack the parameterization of landfast sea ice. To accurately simulate the static landfast sea ice in the North Canadian Archipelago, high-resolution bathymetry and coastal currents data need to be incorporated into the sea-ice models.

3.2 Method and Theoretical Background

3.2.1 Configuration

The NEMO version 3.6 numerical framework (Madec, 2012) is used for setting up experiments. Experiments with the ANHA4 (Arctic and Northern Hemisphere Atlantic) configuration are applied in a tri-polar grid with a $1/4^\circ$ resolution. This gives a resolution of 10 – 16 km in the HBC, which is enough for studying the influence of far field behavior on the HBC (Figure 3.1B). Thus, in this thesis, we apply this configuration to all experiments within the HBC. The ANHA4 configuration contains the entire Arctic region and was enclosed by two open boundaries, one settled down in the Bering Strait and the other located at 20° S in the Atlantic Ocean (shown with mesh grids in Figure 3.1A). The ANHA4 configuration has 50 uneven vertical levels and its horizontal mesh is a sub-domain of the global tri-polar ORCA025 mesh (Madec, 2012; Bernard et al., 2006). Partial step is also enabled to better resolve the

bathymetry (Lemari'e et al., 2013).

3.2.2 Initial Conditions

In order to avoid damping the runoff and climate signals that we are interested in, no temperature or salinity restoring is applied. The model baroclinic timestep is 1080 s. Tidal forcing is considered by specifying geopotential tidal forcing with 9 constituents in the momentum equations (K1, K2, M2, M4 N2, O1, P1, Q1, S2), as well as at the lateral open boundaries (Le Moigne et al., 2012). Initializing experiments are conducted from 1981 with climatological ocean temperature data from the Polar Hydrographic Climatology version 3.0 (Steele et al., 2001).

Initial conditions are such that the ocean is initially at rest, and sea ice is initially 3 m thick in all grid-cells where the ocean temperature is close to the freezing temperature (following the UNESCO (United Nations Educational, Scientific and Cultural Organization) formulation to find the freezing temperature based off of ocean temperature and salinity of Steele et al., 2001).

3.2.3 Ensemble Climate Data

In this study, we utilize the atmospheric fields from the Coupled Model Inter-comparison Project 5 (CMIP5) model experiments to drive the ocean/sea-ice model (Braun et al., 2020). The ensemble members were selected to encompass a range of potential future changes in temperature and precipitation across the Hudson Bay domain to maximize climatic variability (Braun et al., 2020). To satisfy the configuration and fields of the NEMO, we selected and utilized five ensemble members that came from three general circulation models (GCM). The first GCM is the Meteorological Research Institute Coupled General Circulation Model (MRI-CGCM3) with atmospheric resolution of T159 and oceanic horizontal resolution of 1 degree in longitude and 0.5 in latitude (Yukimoto et al., 2012). The second GCM is the Model for Interdisciplinary Research On Climate (MIROC5) with atmospheric resolution T85 and oceanic equivalent resolution of 1.4 degrees except near the Equator (Watanabe et al., 2010). The third GCM is the Geophysical Fluid Dynamics Laboratory Community Model (GFDL-CM3) developed at the NOAA Geophysical Fluid Dynamics Laboratory with a cube-sphere

grid and a C48 horizontal resolution (Donner et al., 2011).

Precipitation, temperature, and wind data were obtained from Watch Forcing Data, ERA-Interim (or WFDEI) with bias correction, as previously mentioned in Braun et al. (2020); Kuzyk and Candlish (2019). The two Representative Concentration Pathways (RCP) 4.5 and 8.5 were used for both MRI-CGCM3 and MIROC5, while the GFDL-CM3 was forced only with RCP4.5 during future time scales. The Coordinated Ocean-ice Reference Experiments bulk formulae were applied to calculate the fluxes of heat, water, and momentum (Large and Yeager, 2009) for each model time step. We used monthly averaged boundary conditions at the model open boundaries of the Bering Strait and 20° S taken from the output of the given CMIP5 experiment. An additional historical control experiment was conducted from 1980–2018 using ERA-Interim forcing (Dee et al., 2011) and historical runoff. The NEMO’s on-the-fly interpolation function was implemented to ensure that all forcing fields were mapped to the NEMO grid. More information about the chosen ensemble members from GCM models can be found in Braun et al. (2020); Kuzyk and Candlish (2019).

3.2.4 Runoff Forcing Fields

To study freshwater dynamics within the HBC, runoff forcing played a significant role in the modeling experiments. Hydrological simulations were performed using a modified version of Arctic-HYPE, a hydrological model, which was improved and calibrated for the HBC region (Ridenour et al., 2019; Stadnyk et al., 2020). Arctic-HYPE was forced by the same bias-corrected atmospheric forcing sets as those used to drive the NEMO simulations described above. The hydrological discharge scenarios were produced for each GCM/RCP pair. For the HBC, two versions of Arctic-HYPE were run for each climate simulation, one naturalized scenario, and one including river regulation (Stadnyk et al., 2021). Additionally, historical WFDEI fields were used to produce naturalized and regulated runoff over 1980-2018 to drive a historical control simulation. An additional set of Arctic-HYPE simulations was carried out for the Pan-Arctic domain, again driven by the same 5 bias-corrected GCM/RCP forcing sets for 1980-2070, plus the WFDEI historical forcing over 1980-2018 (Stadnyk et al., 2020). For both regions, the HYPE output, for all simulations, was regridded from the river mouth positions onto the NEMO model grid using the approach discussed in Hu and Myers

(2015) and Hayashida et al. (2019). For the rest of the model domain, river runoff was taken from the Canadian Centre for Climate Modelling and Analysis (CCCMA) CanESM2 model (Swart et al., 2019), based on historical (1950–2005), RCP4.5 (2006–2070), and RCP8.5 (2006–2070) experiments and a variable velocity flow river routing algorithm (Lenaerts et al., 2015; Buchart, 2021).

Freshwater is also added to the high-latitude ocean by discharge from the Greenland Ice Sheet. Liquid melt, including tundra discharge, is added to the model in the same way as river runoff. Solid discharge or calving is included in the model through a Lagrangian iceberg module (Fichefet et al., 2003; Devilliers et al., 2021; Wouters and Sasgen, 2022). This module includes the modification to apply ocean fields vertically through the thickness of the iceberg, as discussed in Devilliers et al. (2021). As outlined in Gillard et al. (2020), the solid ice discharge of the Greenland Ice Sheet in Lenaerts et al. (2015) for the historical period is derived from remote sensing records from 2000–2012 (Ettema et al., 2009). The freshwater forcing from liquid runoff originating from the Greenland Ice Sheet is obtained from the Regional Atmospheric Climate Model version 2.1 (RACMO2.1; van Meijgaard et al., 2008). RACMO2.1 has a spatial resolution of 11 km, is forced by ERA-Interim fields at its lateral boundaries, has a Greenland Ice Sheet surface mass balance (Noël et al., 2020), and improvements for the climate over Greenland (Ettema et al., 2009). Runoff is allocated with spatial variability by subdividing it into eight basins. Runoff is computed for each basin based on RACMO2.1 (1960–2012) in the historical scenario. For the meltwater calculations beyond 2012, the regional climate model is forced with the atmospheric circulation climate model HadGEM2-ES. Runoff is distributed uniformly to the ocean grid points along each individual basin and incorporated into the coupled land-atmosphere-ocean climate model Community Earth System Model (CESM, version 1.1.2). The CESM is used to simulate multiple scenarios, including a historical (1850–2005) and two future climate scenarios (2006–2200). Further information on how the RACMO fields are integrated into the NEMO model can be found in Gillard et al. (2020). Over the 2004–2016 period, Gillard et al. (2020) showed that using the RACMO fields in NEMO results in comparable findings to the more observationally based product of Bamber et al. (2012, 2018) over the sub-Polar North Atlantic Ocean.

3.2.5 Remapping Method

To add the rivers into our NEMO model, we need to apply a method called "Remapping". According to Hu and Myers (2015), shown in the Figure 3.2, the processes for us to remap the river runoff on the ocean model grid mainly include the steps as follows:

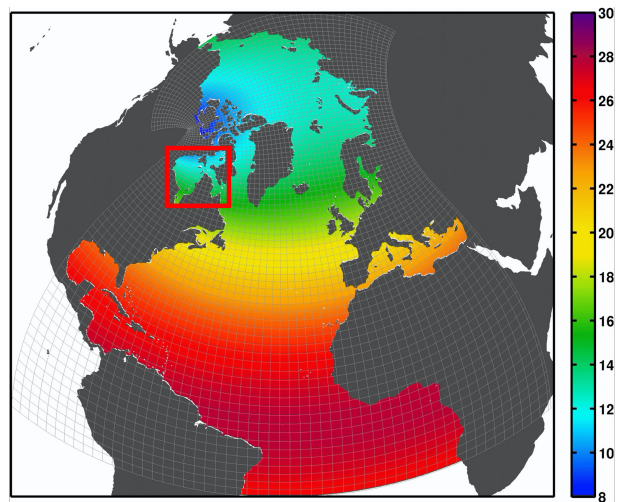
- (1) Drawing buffer-zone-like polygons that are along the coast. The polygons should cover both the land and ocean. Then, for each non-zero data point, we need to judge which polygons it belongs to. Additionally, finding the closest water point (i_0, j_0) in current model-grid polygon. If necessary, re-editing the polygon until there is a large enough water proportion in it.
- (2) Given that we need volume flux of freshwater in the NEMO model, the river runoff data need to be converted from $\text{kg m}^{-2}\text{s}^{-1}$ to m^3s^{-1} , conversion formula is expressed as:

$$\frac{\text{kg}}{\text{m}^2\text{s}} \cdot \frac{\text{m}^2}{\text{kgm}^{-3}} = \frac{\text{m}^3}{\text{s}} \quad (3.1)$$

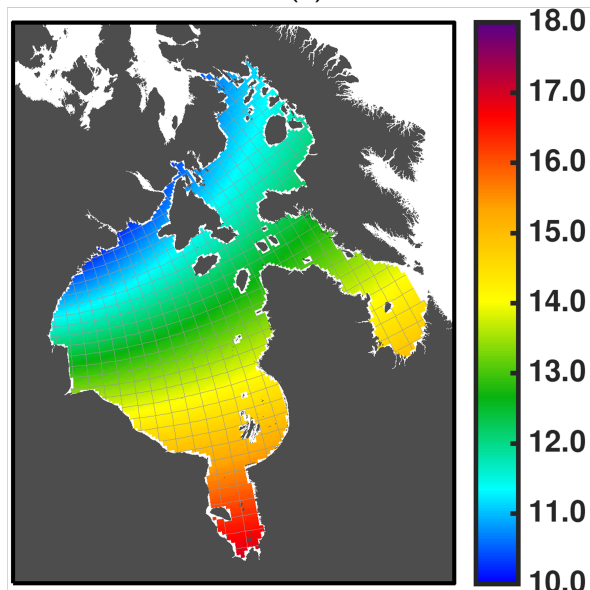
where the area of the HBC in NEMO is with unit m^2 and the kg m^{-3} is the unit of pure water density, generally, chosen as 1,000.

- (3) Finally, after the remapping, it is important to check if the remapped runoff matches up with pre-remapped runoff.

Compared to the simple interpolation method, the remapping method improves the amount of freshwater received by the ocean in the numerical model. Moreover, as it is a point-to-grid remapping method, multiple data sources can be included conveniently.



(A)



(B)

Figure 3.1: The Arctic and Northern Hemispheric Atlantic $1/4^\circ$ (ANHA4) horizontal mesh (every 10 grids, color shows the resolution in kilometers). (A) The entire ANHA4 configuration with $544 \times 800 \times 50$ grid points. (B) The same configuration as in (A) where zoom in the HRC.

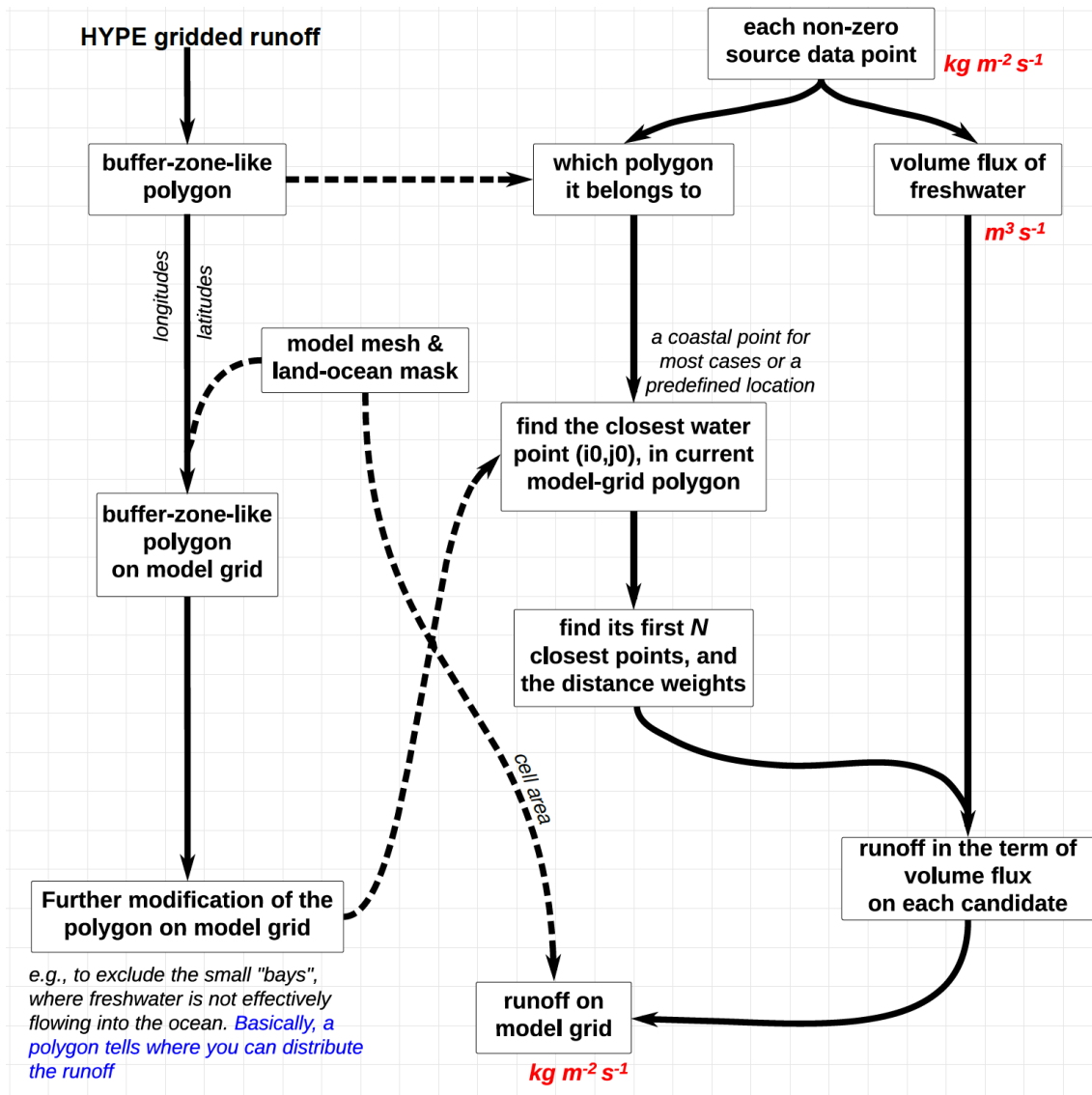


Figure 3.2: The river runoff mapping flow chart. Based on Figure 2 in Hu and Myers, 2015.

Bibliography

- Bamber, J., A. Tedstone, M. King, I. Howat, E. Enderlin, M. Van den Broeke, and B. Noel, 2018: Land ice freshwater budget of the Arctic and North Atlantic Oceans: 1. Data, methods, and results. *Journal of Geophysical Research: Oceans*, **123** (3), 1827–1837.
- Bamber, J., M. Van Den Broeke, J. Ettema, J. Lenaerts, and E. Rignot, 2012: Recent large increases in freshwater fluxes from Greenland into the North Atlantic. *Geophysical Research Letters*, **39** (19).
- Bernard, B., and Coauthors, 2006: Impact of partial steps and momentum advection schemes in a global ocean circulation model at eddy-permitting resolution. *Ocean dynamics*, **56** (5), 543–567.
- Braun, M., A. Thiombiano, M. Vieira, and T. Stadnyk, 2020: The changing climatology of hudson bay (1981–2070). *Elementa: Science of the Anthropocene*.
- Buchart, L., 2021: Sea Ice Modelling in the Pikialasorsuaq: Parameters Sensitivities and Future Prospects. M.S. thesis, Department of Earth and Atmospheric Science, University of Alberta.
- Dee, D. P., and Coauthors, 2011: The ERA-Interim reanalysis: Configuration and performance of the data assimilation system. *Quarterly Journal of the royal meteorological society*, **137** (656), 553–597.
- Devilliers, M., D. Swingedouw, J. Mignot, J. Deshayes, G. Garric, and M. Ayache, 2021: A realistic Greenland ice sheet and surrounding glaciers and ice caps melting in a coupled climate model. *Climate Dynamics*, **57** (9-10), 2467–2489.
- Donner, L. J., and Coauthors, 2011: The dynamical core, physical parameterizations, and basic simulation characteristics of the atmospheric component am3 of the gfdl global coupled model cm3. *Journal of Climate*, **24** (13), 3484–3519.
- Ettema, J., M. R. van den Broeke, E. van Meijgaard, W. J. van de Berg, J. L. Bamber, J. E. Box, and R. C. Bales, 2009: Higher surface mass balance of the Greenland ice sheet revealed by high-resolution climate modeling. *Geophysical Research Letters*, **36** (12).

- Fichefet, T., C. Poncin, H. Goosse, P. Huybrechts, I. Janssens, and H. Le Treut, 2003: Implications of changes in freshwater flux from the Greenland ice sheet for the climate of the 21st century. *Geophysical Research Letters*, **30** (17).
- Gillard, L. C., X. Hu, P. G. Myers, M. H. Ribergaard, and C. M. Lee, 2020: Drivers for Atlantic-origin waters abutting Greenland. *The Cryosphere*, **14** (8), 2729–2753.
- Griffies, S. M., and Coauthors, 2000: Developments in ocean climate modelling. *Ocean Modelling*, **2** (3-4), 123–192.
- Griffies, S. M., and Coauthors, 2009: Coordinated ocean-ice reference experiments (cores). *Ocean modelling*, **26** (1-2), 1–46.
- Hayashida, H., and Coauthors, 2019: Csib v1 (canadian sea-ice biogeochemistry): a sea-ice biogeochemical model for the NEMO community ocean modelling framework. *Geoscientific Model Development*, **12** (5), 1965–1990.
- Hu, X., and P. Myers, 2015: An Effective Approach to Remap Runoff onto an Ocean Model Grid. CMOS Congress, Poster presented at the 2015 CMOS Congress, Whistler, BC.
- Kuzyk, Z., and L. Candlish, 2019: From science to policy in the greater hudson bay marine region: An integrated regional impact study (iris) of climate change and modernization. *ArcticNet, Québec City*, 424.
- Large, W., and S. Yeager, 2009: The global climatology of an interannually varying air–sea flux data set. *Climate dynamics*, **33** (2), 341–364.
- Le Moigne, P., T. Penduff, M. Juza, L. Brodeau, A.-M. Treguier, B. Barnier, and G. Madec, 2012: Nemo on the shelf: assessment of the iberia-biscay-ireland configuration. *Ocean Modelling*, **52**, 1–18.
- Lemari’e, F., E. Cauquil, V. Thierry, and R. Benshila, 2013: A new 1/12 ° global coastlines and continental shelf dataset for the analysis of coupled human-ocean systems. *Ocean Modelling*, **69**, 1–10.

- Lenaerts, J. T., D. Le Bars, L. Van Kampenhout, M. Vizcaino, E. M. Enderlin, and M. R. Van Den Broeke, 2015: Representing Greenland ice sheet freshwater fluxes in climate models. *Geophysical Research Letters*, **42** (15), 6373–6381.
- Madec, G., 2012: Nemo ocean engine. *Note du Pole de modelisation*, **27**, 503.
- Noël, B., L. Van Kampenhout, W. J. Van De Berg, J. Lenaerts, B. Wouters, and M. R. Van Den Broeke, 2020: Brief communication: CESM2 climate forcing (1950–2014) yields realistic Greenland ice sheet surface mass balance. *The Cryosphere*, **14** (4), 1425–1435.
- Ridenour, N. A., and Coauthors, 2019: Sensitivity of freshwater dynamics to ocean model resolution and river discharge forcing in the Hudson Bay Complex. *Journal of Marine Systems*, **196**, 48–64.
- Stadnyk, T. A., M. K. MacDonald, A. Tefs, S. J. Déry, K. Koenig, D. Gustafsson, K. Isberg, and B. Arheimer, 2020: Hydrological modeling of freshwater discharge into Hudson Bay using HYPE. *Elementa: Science of the Anthropocene*, **8**.
- Stadnyk, T. A., and Coauthors, 2021: Changing freshwater contributions to the Arctic: A 90-year trend analysis (1981–2070). *Elem Sci Anth*, **9** (1), 00098.
- Steele, M., R. Morley, and W. Ermold, 2001: Phc: A global ocean hydrography with a high-quality arctic ocean. *Journal of Climate*, **14** (9), 2079–2087.
- Swart, N. C., and Coauthors, 2019: The Canadian earth system model version 5 (CanESM5.0.3). *Geoscientific Model Development*, **12** (11), 4823–4873.
- van Meijgaard, E., L. Van Uft, W. Van de Berg, F. Bosveld, B. Van den Hurk, G. Lenderink, and A. Siebesma, 2008: *The KNMI regional atmospheric climate model RACMO, version 2.1*. KNMI De Bilt, The Netherlands.
- Watanabe, M., and Coauthors, 2010: Improved climate simulation by MIROC5: mean states, variability, and climate sensitivity. *Journal of Climate*, **23** (23), 6312–6335.
- Wouters, B., and I. Sasgen, 2022: Increasing freshwater fluxes from the Greenland Ice Sheet observed from space. *Oceanography*, **35** (3/4), 103–105.

Yukimoto, S., and Coauthors, 2012: A new global climate model of the meteorological research institute: Mri-cgcm3—model description and basic performance—. *Journal of the Meteorological Society of Japan. Ser. II*, **90**, 23–64.

Chapter 4

Influences of Climate Change and River Regulation on Hudson Bay Complex Freshwater Dynamics

In Chapter 4, P.G. Myers and L. Castro de la Guardia designed and conducted the naturalized and regulated experiments. T. Andrew did the regulations for all rivers around the Hudson Bay Complex. N. Ridenour taught and provided me assistance on remapping, and with the majority of work from her, we remapped runoff data from HYPE model to our ANHA4 grid. I was responsible for analyzing different physical variables with MATLAB scripts and writing the content of this chapter. N. Grivault and L. Castro de la Guardia provided assistance on codes for some calculations. P.G. Myers provided advice, guidance, and further edits.

Abstract

The Hudson Bay Complex (HBC), a region including Foxe Basin, Hudson Strait, Ungava Bay, Hudson Bay, and James Bay, is experiencing major changes in its freshwater supply and sources. As compared to the Arctic Ocean, the HBC is much smaller. However, there is about 900km^3 of river discharge feeding into this region per year ($\sim 25\%$ of that which enters the Arctic Ocean).

One of the main freshwater sources here is river runoff, changing due to anthropogenic diversions, dams, and reservoirs. Another important source of freshwater is sea ice melt and freeze cycle, which is very sensitive to climate change. To assess river regulation and climate change impacts on HBC's freshwater dynamics, we employed the NEMO ocean sea-ice model with the Arctic and Northern Hemisphere Atlantic (ANHA) configuration. Utilizing an ensemble of five climate simulations from the fifth Coupled Model Inter-comparison Project (CMIP5), initialized between 1980 and 2005, driven by naturalized and regulated river runoff with different representative concentrations of CO_2 (RCP4.5 and RCP8.5) over 2006–2070, we observed increased freshwater content and diminished sea ice thickness and concentration in the future. Within HBC, maximum mixed layer depth (MMLD) of approximately 230 m near the northern Hudson Strait is anticipated. However, augmented freshwater from rivers and ice melting are projected to lead to slightly shallower mixed layers in the future, compared to historical conditions.

Furthermore, analysis of annual and seasonal atmospheric forcing fields uncovers intricate ocean-sea ice-atmosphere interplay within a changing climate. Notably, salinity and freshwater content variations manifest unique influences by different ensemble members, capturing hydrological cycle evolution within climate models. Variations between naturalized and regulated regimes are attributed to factors like freshwater residence time and discharge timing.

4.1 Introduction

The HBC is connected to the Canadian Arctic Archipelago and the Arctic Ocean through FB in its northern part, and to the Atlantic Ocean via HS in its eastern part (Figure 4.1). The general cyclonic circulation pattern in HB brings approximately $760\text{ km}^3\text{yr}^{-1}$ freshwater

within the bay before exporting via HS. The freshwater mainly comes from river discharges and runoff around HB plus cold freshwater from the Arctic Ocean via FB (JafariKhasragh et al., 2019; Déry et al., 2011).

HS connects the Atlantic Ocean and the Labrador Sea to Hudson Bay in the northeast of Canada. The strait is a long (~ 700 km), wide (an average width of 125 km) channel, which is covered by ice seasonally. Previous studies have indicated that in HS sea ice typically starts to form in mid-November, completely covering the strait during December and disappearing by July (Andrews et al., 2018; Houser and Gough, 2003; Drinkwater, 1986). Specifically, the open water season (i.e. the number of days between ice breakup and freeze-up) in HS is from July to October when most of the shipping occurs (Babb et al., 2021). Results from Babb et al. (2021) demonstrated that the ice pack has moved to the southeast of HS, away from Baffin Island and against Nunavik, induced by the prevailing northwesterly winds.

For the large subarctic estuarine system of the Hudson Bay Marine Region (HBMR; including Foxe Basin, Hudson Bay, and James Bay), two entrances are located in the north of Foxe Basin called Fury and Hecla Strait (FHS) and the HS. The HS is a significant transport pathway for freshwater from the HBMR into the Labrador Sea (McCullough et al., 2019; Straneo and Saucier, 2008; Drinkwater, 1986) and a principal channel and seasonal habitat for a large amount of fish and marine mammals (Elliot et al., 2013; Westdal et al., 2010).

Hudson Bay (HB), a large (8×10^5 km²) and shallow (averaged depth ~ 150 m) inland sea, is located in the Arctic and subarctic areas of Canada. The bay is relatively isolated from open ocean circulation and thus acts as an independent system from the Arctic and Atlantic Oceans (Ingram and Prinsenberg, 1998; Stewart and Barber, 2010). As an inland sea, it is fed by large amounts of freshwater mainly from river runoff and ice melt, where the annual mean circulation is stably cyclonic (Dunbar, 1982; Ingram and Larouche, 1987; Prinsenberg, 1988; Lavoie et al., 2013).

The seasonal ice variations in HB are significantly affected by atmospheric forcing rather than transports of ice or water from other basins (Saucier and Dionne, 1998a). The majority of sea ice in the HBC is called "mobile pack ice", which is a mass of ice floating in the sea that moves following ocean currents and winds (Rampal et al., 2009). However, during the period of ice generation in the study region, some "landfast" ice can be formed coastally several weeks

after freeze-up. Unlike the "mobile pack ice", landfast ice is defined as relatively fastened to the coastline, to the sea floor, or to grounded icebergs (Leppäranta, 2011; Yu et al., 2014). A change of ice breakup and freeze-up patterns between 1980 and 2014 in the study area were found by Andrews et al. (2018), where the breakup grew from the southeast and the northwest of HB, and substantially longer open water seasons were observed in HS than in HB. Andrews et al. (2018) also projected that the majority of offshore waters in the HBC would experience extended open water durations in the future. Studies from Hochheim and Barber (2014) indicated that the earliest open water time was found in HS, in the eastern HB, and in the centre of the HBC.

As the mobile ice in HB flows along with the inner counter-clockwise circulation pattern (Landy et al., 2017), a polynya can be found recurrently in the northwest part of the bay, which is driven by strong offshore northwesterly winds. In addition, there is an ice thickness gradient from west to east because of the existence of new, thin ice within the polynya and the afterwards accumulation of ice in eastern HB (Saucier et al., 2004; Landy et al., 2017). Therefore, sea ice distribution in HB is asymmetric with thinner ice in the west and accumulated thicker sea ice in the east (Gagnon and Gough, 2006; Landy et al., 2017; Kirillov et al., 2020).

Generally, a polynya is a persistent region of open water surrounded by ice that appears at times (Stringer and Groves, 1991). Under the circumstances of climate, this area will be thickened and reinforced (Smith et al., 1990; Tamura and Ohshima, 2011). The polynya in northwestern HB is called the Kivalliq Polynya by Bruneau et al. (2021), defined according to Gunn (2015) who divided HB into nine subregions. The Kivalliq Polynya was studied and observed to have great contributions in HB climate as the brine rejection due to ice production increases ocean salinity along the western coastline of HB (Saucier et al., 2004; Burt et al., 2016), enhances deep water mixing within the bay (Stewart and Barber, 2010; Granskog et al., 2011), and therefore accelerates heat loss from the ocean to atmosphere, which further warms the above air column and alters mesoscale atmospheric processes (Morales Maqueda et al., 2004). Beside this polynya, Rankin Inlet, Nunavut (62° N, 92.1° W) is a community with approximately 2,850 people (Canada, 2017). Research in Andrews et al. (2018) found that an average open water season (1996–2016) with less than 20% sea ice concentration was

about 16 weeks in the Rankin Inlet community. Their study also suggested that the shipping accessibility for this region was typically limited by the timing of ice within its area.

Foxe Basin (FB), a 550 km long, 360 km wide and relatively shallow basin, is bounded to the north and east by Baffin Island and to the west by Melville Peninsula and Southampton Island. This inland sea communicates with the Canadian Arctic in the north by Fury and Hecla Strait, with HB in the southwest via Roes Welcome Sound, and with HS in the south through Foxe Channel. Ambient waters in FB are covered by sea ice during most times of the year, primarily consisting of first-year ice and some second-year ice closer to the coastline.(Prinsenber, 1986a; Laidler et al., 2009; Ford et al., 2009).

James Bay (JB) is located between northern Ontario and Quebec. This bay is 443 km long, 217 km wide and generally < 60 m deep. JB is fed by many rivers, including Nottaway, Harricana, Moose, Albany, Attawapiskat, La Grande, Eastmain, Rupert, Broadback, and Ekwan, which are responsible for the freshening occurred in this region. Results from Prinsenber (1980) demonstrated that the lowest salinity was presented in JB compared with the other subregions of the HBC. Freshwater from river runoff in this domain accounted for over 50% of the total runoff (Prinsenber, 1980). Seasonal ice period in this bay varies spatially from 5 to 10 months each year (Hochheim and Barber, 2014). Usually, freeze-up develops during the second half of November in JB because the bay is shallow that ice spreads quickly to completely cover it by early December (Andrews et al., 2016).

With regard to the freshwater budget system in the HBC, the complex is fed by approximately $940 \text{ km}^3\text{yr}^{-1}$ amount of freshwater coming from rivers, which is comparable to the combined outflows of the Mackenzie and St Lawrence rivers. Due to the restriction of the counterclockwise current mainly within Hudson Bay, river runoff is firstly transported along the coastline then secondly to Hudson Strait and the Labrador Sea, and finally joined with other water sources in the North Atlantic Ocean. The annual ice-melting freshwater to the surface of the whole region is $\sim 1500 \text{ km}^3$. Within the majority area of the HBC, evaporation surpasses precipitation. The James Bay holds the only exception where the precipitation surpasses evaporation (Hamilton, 2013).

It should be noted that the response of ocean and ice properties under the circumstance of climate change and river regulation is important for better understanding the marine con-

ditions in the HBC. In this study, the description of methods and data with the model and experiments is provided in section 4.2. Section 4.3 will present the results of different physical variables associated with the atmosphere, the sea ice, and the ocean. Section 4.4 will discuss the findings from previous results and make conclusions, ending up with the current limitations of our model simulations and insights into how further research could be conducted and improved.

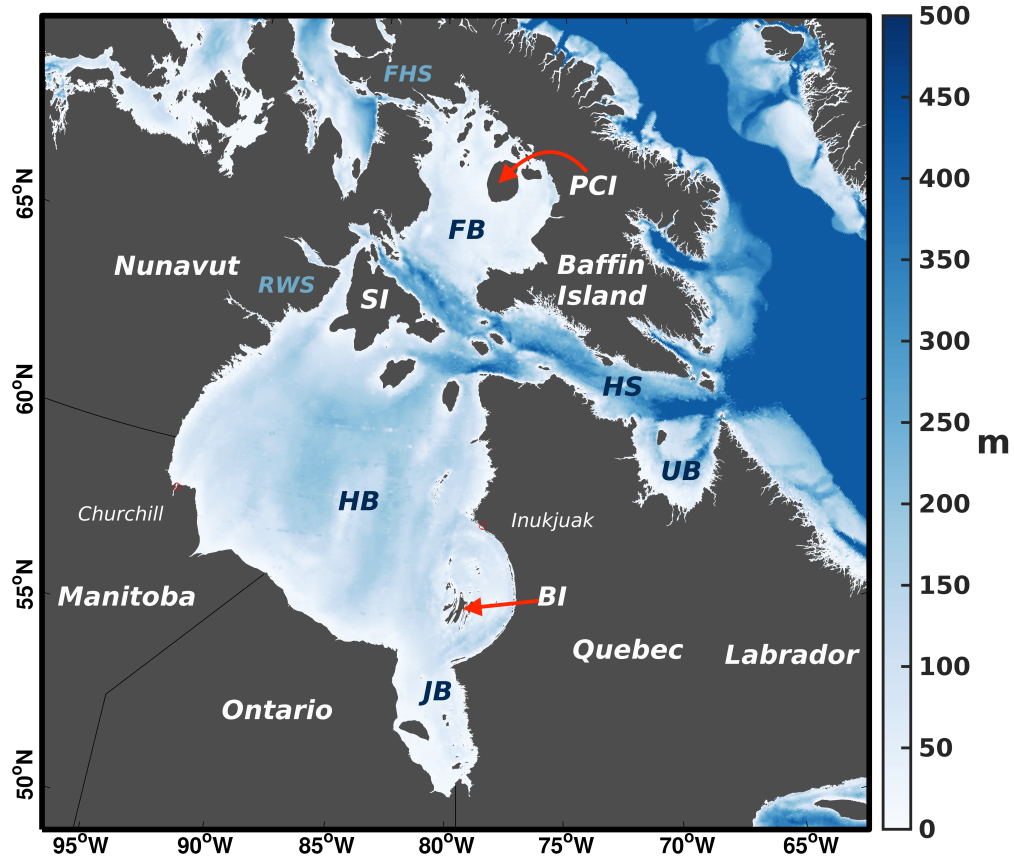


Figure 4.1: The Hudson Bay Complex (HBC) Bathymetry. Abbreviations for specific geographic locations stands for FB = Foxye Basin, HS = Hudson Strait, UB = Ungava Bay, HB = Hudson Bay, JB = James Bay, PCI = Prince Charles Island, SI = Southampton Island, FHS = Fury and Hecla Strait, RWS = Roes Welcome Sound, and BI = Belcher Islands. Modified based on Ridenour et al., 2019b.

4.2 Methods and Data

Given that there is almost no ice during summer (June to August) in the HBC, the oceanic properties in summer months are not the focus of our discussion. The remaining three seasons are studied and taken here as spring (March to May), fall (September to November) and winter

(December to February). However, the duration selected for each season can be different from the real as seasonal months are significantly regional dependent (Déry et al., 2016). The 90-year study period is divided into three parts as historical period (1981–2005), near-future period (2030–2049) and far-future (2050–2070).

4.2.1 Statistical Analyses Method

For the entire future period (2006–2070), the mean, standard deviation (SD), coefficient of variation (CV, calculated as SD/mean) and components (slope and intercept) of linear regression using the least-squares method are calculated and listed in tables for different ice and oceanic variables. The Sen’s slope estimator provides the magnitude of the trend while a probability value (p value) of 0.05 quantifies statistically significant trends in this thesis (Déry et al., 2016).

4.2.2 Climate Ensemble

The Coupled Model Inter-comparison Project 5 (CMIP5) model experiments are applied in this study to provide the atmospheric fields to drive the ocean/sea-ice model. The members were chosen to bracket future changes in temperature and precipitation across the Hudson Bay domain, and thus maximize climatic variability (Braun et al., 2020). To satisfy the configuration and fields of the NEMO, the five ensemble members were selected and used. These experiments came from three general circulation models (GCM): the Meteorological Research Institute Coupled General Circulation Model (MRI-CGCM3) with atmospheric resolution of T159 and oceanic horizontal resolution of 1 degree in longitude and 0.5 in latitude (Yukimoto et al., 2012), the Model for Interdisciplinary Research On Climate (MIROC5) with resolution T85 for the atmosphere and the equivalent 1.4 degrees for the ocean except near the Equator (Watanabe et al., 2010), and the Geophysical Fluid Dynamics Laboratory Community Model (GFDL-CM3) developed at the NOAA Geophysical Fluid Dynamics Laboratory with a cube-sphere grid, giving a C48 horizontal resolution (Donner et al., 2011).

There are two Representative Concentration Pathways (RCP) 4.5 and 8.5 used for both MRI-CGCM3 and MIROC5, while the GFDL-CM3 was forced only with RCP4.5 during future time scale. Precipitation, temperature and wind data with bias correction were selected from

Watch Forcing Data, ERA-Interim (or WFDEI), as mentioned in Braun et al. (2020); Kuzyk and Candlish (2019). The Coordinated Ocean-ice Reference Experiments bulk formulae were applied to compute fluxes of heat, water, and momentum (Large and Yeager, 2009) for each model time step. Monthly averaged boundary conditions at the model open boundaries of Bering Strait and 20° S were also taken from the output of the given CMIP5 experiment. An additional historical control experiment was run from 1980–2018 using ERA-Interim forcing (Dee et al., 2011) and historical runoff. The NEMO’s on-the-fly interpolation function was implemented to ensure all forcing fields are mapped to the NEMO grid. More information about the chosen ensemble members from GCM models can be referred to Braun et al. (2020); Kuzyk and Candlish (2019).

4.2.3 River Runoff Datasets

To investigate the freshwater properties within the HBC, river runoff plays a significant role in model simulations. As there is no runoff forcing provided from the CMIP experiments, external runoff outputs are considered. Arctic-Hydrological Predictions for the Environment (Arctic-HYPE) was applied to the HBC region for adding runoff. Arctic-HYPE was forced by the same bias corrected atmospheric forcing sets as used to drive the NEMO simulations described above.

In all cases, monthly river discharge for the HBC were produced for each GCM/RCP pair, using the GCM’s historical forcing simulation for 1981–2005 and the future simulation for 2006–2070. Two versions of Arctic-HYPE were run for each climate simulation, one naturalized scenario and one including river regulation (Stadnyk et al., 2021). As such, two sets of 90 year long hydrological discharge scenarios were produced to drive NEMO-naturalized and regulated, for each bias corrected GCM/RCP pair. Additionally, historical WFDEI fields were used to produced naturalized and regulated runoff over 1980–2018 to drive a historical control simulation.

An additional set of Arctic-HYPE simulations were carried out (Stadnyk et al., 2021) for the Pan-Arctic domain, again driven by the same 5 bias corrected GCM/RCP forcing sets for 1980–2070, plus the WFDEI historical forcing over 1980–2018. Given a lack of details on regulation on Russian rivers, only naturalized output was produced for the Pan-Arctic

domain (Stadnyk et al., 2021). For both regions and all simulations, the HYPE output was then regridded from the river mouth positions onto the NEMO model grid using the approach discussed in Hu and Myers (2015) and Hayashida et al. (2019).

4.3 Results

In this section, contributions from climate change and river discharge regulation on the HBC system over the historical (1981–2005) and future (2006–2070) 90-year periods will be examined. First, an analysis of how different climate scenarios affect a variety of atmospheric, ice, and oceanic variables will be conducted. This will be followed by a comparison of runs with regulated and unregulated rivers. Results in terms of atmospheric forcing fields, sea ice, and the ocean are summarized below.

4.3.1 Analysis of Atmospheric Forcing Fields

As mentioned in Section 4.2 and the summary of the naturalized (i.e., only driven by climate change) and regulated runs in Figure 4.2, the five-member ensemble of climate-driven data are from the fifth Coupled Model Intercomparison Project (CMIP5; Taylor et al. 2012). Experiments with atmospheric forcing fields including 3-hourly sea surface temperature, precipitation (including snow), evaporation, humidity, short- and longwave radiation, surface pressure, and zonal and meridional surface winds which are applied to the NEMO model. Among these atmospheric fields, Watch Forcing Data, ERA-Interim (WFDEI) are employed for bias correction of wind, temperature, and precipitation. These atmospheric variables are characterized by comparing historical (1981–2005) and future (2006–2070) scenarios. Specifically, for the Hudson Bay System Study (BaySys) project, the three historical components come from the Meteorological Research Institute Coupled General Circulation Model (MRI-CGCM3), the Geophysical Fluid Dynamics Laboratory Community Model (GFDL-CM3), and the Fifth Model for Interdisciplinary Research On Climate (MIROC5). In terms of the future scenarios, the representative concentration pathways (RCP; defined as the different representative concentrations of CO₂) are considered. The two experiments with RCP4.5 and RCP8.5 are generated from the MRI-CGCM3 and MIROC5. For the GFDL-CM3, only

RCP4.5 is chosen for study. Further information concerning ensemble data, details can be found in Stadnyk et al. (2019) and Braun et al. (2021).

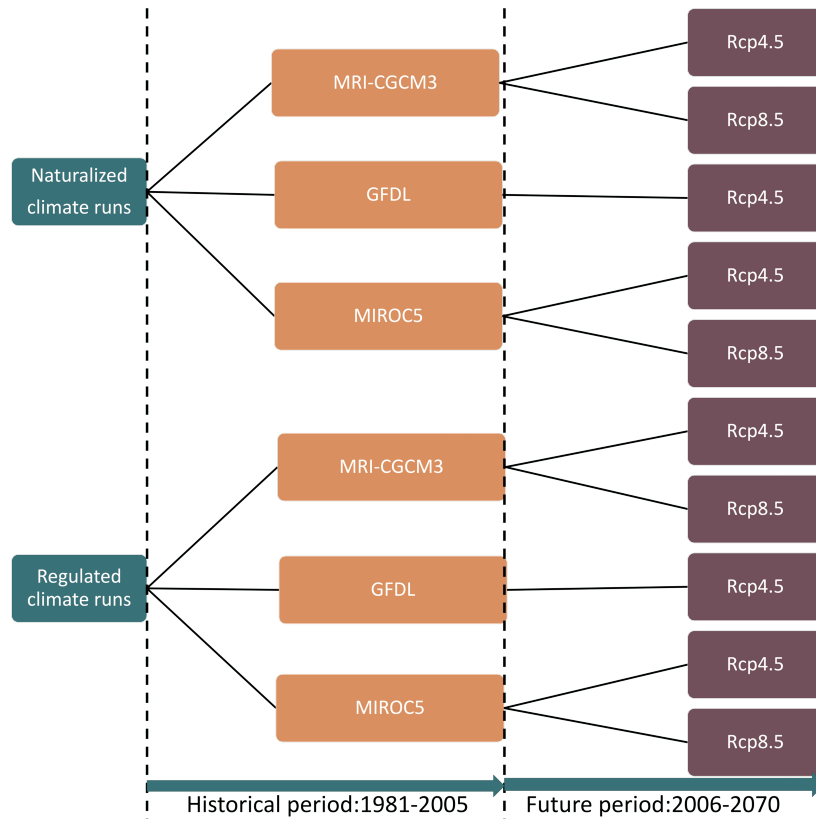


Figure 4.2: The schematic of ensemble runs with the impacts of climate change and river regulation (Note that naturalized runs are with unregulated rivers and regulated runs are with regulated rivers). Data are from the Meteorological Research Institute Coupled General Circulation Model (MRI-CGCM3), the Geophysical Fluid Dynamics Laboratory Community Model (GFDL-CM3), and the Fifth Model for Interdisciplinary Research On Climate (MIROC5). Orange boxes to the left represent sources of data for the initialized historical period: 1981–2005, while the ten brown boxes to the right are the future experiments which run from 2006 to 2070.

General increases in surface air temperature (SAT) is considered a precursor, symptom and consequence of climate change. This can be readily observed in simulations of SAT ranging from 1981 to 2070 in Figure 4.3A. To illustrate the mean changes, an ensemble mean of the five climate-driven data is presented by the black dashed line. In the historical period, the surface air temperature was about -9 ± 0.50 °C, and is projected to grow by 4.93 °C from -7.68 °C to -2.75 °C between 2006 and 2070. With regards to the seasonal changes (Figure 4.3B), the SAT is only above 0 °C in autumn for future scenarios, and this is predicted to increase from -0.95 °C in 2006 to 3.12 °C in 2070. By contrast, the winter SAT shows the greatest future variability, where linear trends range from -21.37 °C to -12.01 °C. Among all the five members of the annual air temperature ensemble, the GFDL-CM3 experiment

with RCP4.5 forcing experiences the most significant increase, even larger than the MIROC5 RCP8.5 simulation, which is with a higher radiative forcing, after 2021 and reaches a peak of 0.1 °C in 2062. Generally, during the far-future period (2050–2070), a substantial gap (4 – 5 °C) in SAT can be found between the GFDL RCP4.5, which shares a similar trend with the MIROC5 RCP8.5, and three other simulations (MRI-CGCM3 RCP4.5, MRI-CGCM3 RCP8.5 and MIROC5 RCP4.5). Distinct from trends observed in SAT, the annual mean precipitation is projected to grow from 0.46 m/year to 0.57 m/year, an increase more than 24% (Figure 4.3C). Seasonally, precipitation rates are expected to increase by 18.60%, 25.05%, and 62.58% in the spring, fall and winter, respectively (Figure 4.3D). Based on the above simulation results, considering future elevated SATs and precipitation rates, the ocean and sea ice are likely to both receive more heat and freshwater from the atmosphere, particularly during the winter months (December–February).

Unlike previous atmospheric variables, there are only slight differences in surface wind speed (U_{10}) on either seasonal or yearly scales. As shown in Figure 4.3E, the annual trends of MRI-CGCM3 RCP4.5, MRI-CGCM3 RCP8.5, MIROC5 RCP4.5, and MIROC5 RCP8.5 remains at approximately 6.45 m/s over the study period. The greatest seasonal increase in U_{10} is predicted to be measured at 6.75 m/s within the winter months of 2006–2070 (Figure 4.3F). Differing from the prior four experiments, as the GFDL wind speed data is non-bias corrected, its simulated U_{10} is markedly lower, ranging from a maximum of 5.60 m/s in 2006 to a minimum of 4.55 m/s in 2053. A difference of ~ 1 m/s can be identified between the sole non-bias corrected experiment (i.e., GFDL) and bias corrected experiments (all other experiments). Overall, such intensified wind forcing fields even if minor can enhance atmosphere-ocean-ice interactions.

Bias corrected data has the advantage of being able to more closely simulate the real atmosphere (Teutschbein and Seibert, 2012; Akhter et al., 2017) and this is important as small deviations in simulated wind speeds from the actual can lead to radically different outcomes in the predictions of future wind changes (Chen et al., 2000; Xu et al., 2021). However, in this study, the interactions among the atmosphere, ice, and ocean are mainly considered rather than future forecasts. Therefore, the GFDL wind speed data without bias correction will not be discussed in detail in this thesis.

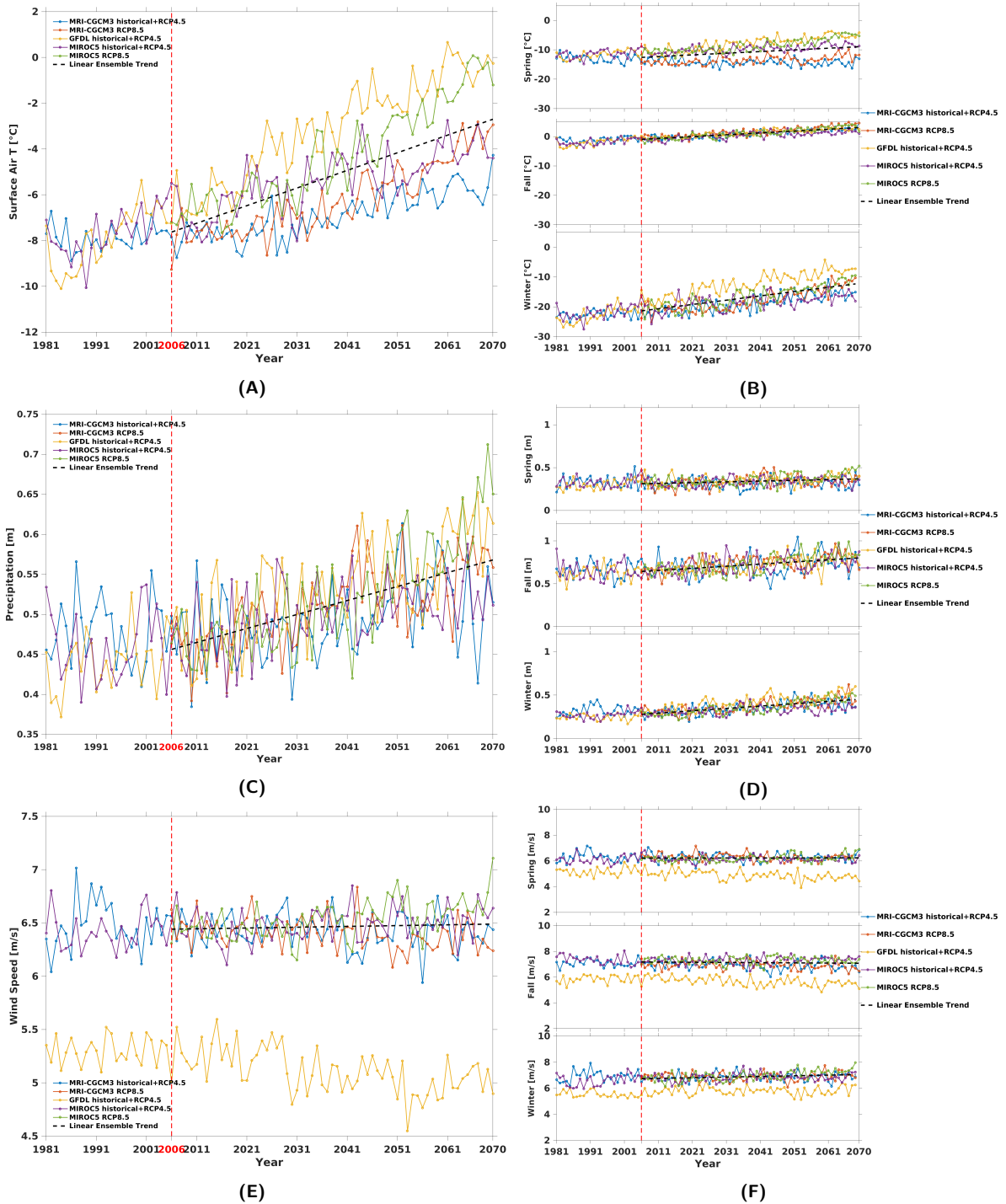


Figure 4.3: Time series of annual (A) air temperature at 2 m height ($^{\circ}\text{C}$), (C) precipitation (m), and (E) wind speed (m/s) averaged over the HBC from 1981 to 2070 for 5 climate runs. Seasonal time series of these variables are given in (B), (D), and (F) respectively.

4.3.2 Net heat flux

The net heat flux (NHF) reflects the total heat exchange between the ocean and atmosphere and is an essential factor in determining the evolution of the Earth’s climate system (Tomita et al., 2021). Due to the existence of sea ice in the HBC, interactions among the atmosphere, ice, and oceans are considered in NHF calculations. Within experiments based on the NEMO model, the heat flux at the interface of the ocean and ice already includes fluxes affected by ice. The net downward heat flux, by contrast, only considers the net flux between atmosphere and ocean without considering the sea-ice. According to JafariKhasragh et al. (2019); Tomita et al. (2021), NHF can be calculated by summing four components: net longwave radiation (LWR), net shortwave radiation (SWR), latent heat flux (LHF), and sensible heat flux (SHF):

$$Q_{NHF} = Q_{LW} + Q_{SW} + Q_{LHF} + Q_{SHF} \quad (4.1)$$

Here, all heat fluxes are assigned positive values when their direction is downward, away from the atmosphere to the ocean surface and negative when the heat is lost from the ocean.

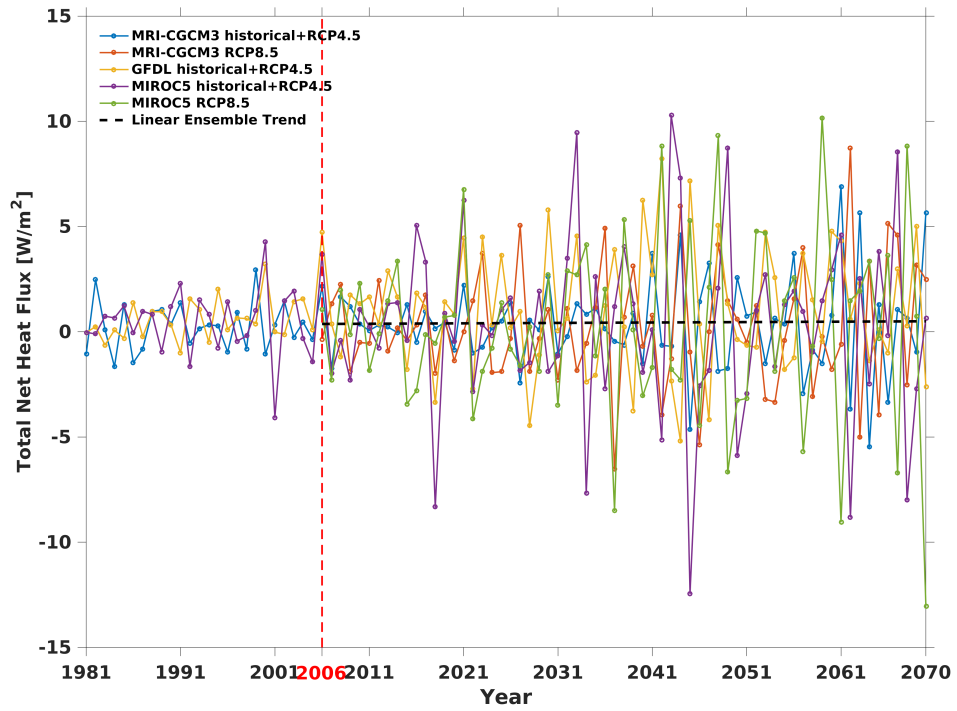
There is little long-term change in the net heat flux (Figure 4.4A), although there is a large increase in the year-to-year variability. According to results in section 4.3.1, a warming climate leads to higher air temperatures in the region. This enhances the ocean heat input in spring (the top panel in Figure 4.4B) averaged from 0.48 Wm^{-2} to 15.86 Wm^{-2} and summer (not shown), while reducing the heat loss in fall (the middle panel in Figure 4.4B) averaged from -67.16 Wm^{-2} to -54.63 Wm^{-2} over the 65-year future time range. However, the changes in these seasons are compensated by significant heat loss from the basin in winter (the bottom panel in Figure 4.4B), where its average NHF is projected to increase by 119.84% from -54.47 Wm^{-2} to -119.75 Wm^{-2} over the 2006–2070 period. Although it may be counter-intuitive since the air temperature also warms in winter (the bottom panel in Figure 4.3B), the enhanced heat loss is linked to the significant reduction in the sea-ice cover through the winter season (the bottom panel in Figure 4.7B). Sea ice insulates the ocean below from the cold air temperatures. Thus, when the bay is completely ice-covered, the net heat flux is very small. However, as the ice cover reduces, exposing the ocean below to cold winter atmospheric temperatures, significant latent and sensible heat loss occurs (unless

sufficient heat is removed from the upper layer to lead to ice formation). The large heat losses seen by 2070 in the winter (the bottom panel in Figure 4.4B) are now consistent with other marginal sea ice regions, such as the Labrador Sea (Pennelly and Myers, 2021).

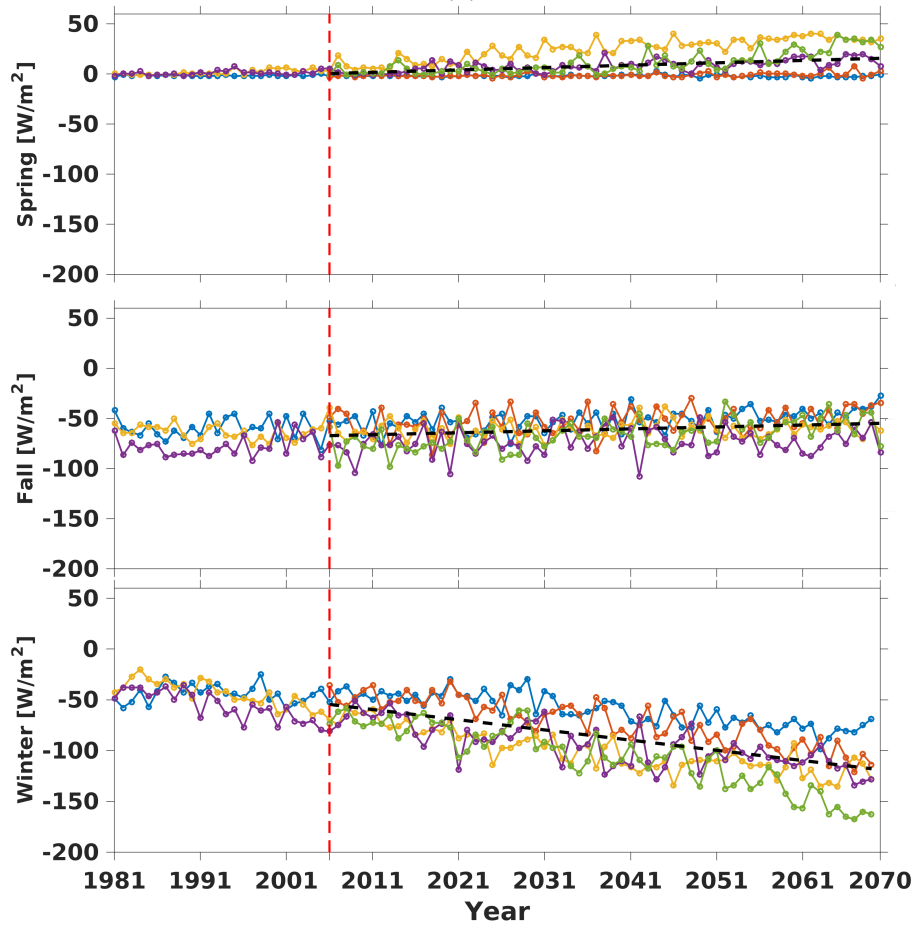
4.3.3 Maximum Mixed Layer Depth

Oceanic conditions in the HBC are controlled by strong vertical stratification, with the upper ocean layer being less dense than the lower layers (Stewart and Lockhart, 2005a; Lavoie et al., 2013). As sea ice forms during winter months, salt is ejected from the forming ice to the ocean, which increases the upper ocean layer density and weakens stratification (Bouttes et al., 2010; Eastwood et al., 2020). The weakened stratification causes the mixed layer depths to be deeper in the winter. Additionally, during winter cooling, the ocean surface is exposed to the cold air, loses buoyancy, and promotes deeper mixed layers (Somavilla et al., 2017; Abdulla et al., 2018). Studies in Prinsenbergl (1986b); Ferland et al. (2011) suggest that the winter mixing can reach up to 90 m in the central part of HB, compared to summer vertical mixing, which is prevented by a sharp pycnocline at the depth of 15-25 m. The maximum mixed layer depth (MMLD) studied in this thesis is based on the GCM mixing scheme, which is the same as the scheme in Lavoie et al. (2013). GFDL model simulations are shown to have a better representation of the MMLD in the central part of the HBC, with an annual average varying between 18–50 m (Lavoie et al., 2013). The reason for deeper mixed layers in the central part of the bay is less sea ice, which exposes the ocean surface to the winter air, cools it, and results in mixing and sinking. Lavoie et al. (2013) concluded that no trends were found for the MMLD in HB over the next 50 years.

Our results show that the MMLD in the HBC is projected to decrease significantly from the ensemble of all five member climate-induced simulations over the period of 1981–2021 (Figure 4.5), especially for the recent decade (2011–2021) when the MMLDs reached their smallest value (~ 140 m). Such phenomenon suggests a general increase in oceanic heat content and strengthening of oceanic stratification, congruent with other projections (Eastwood et al., 2020; Lavoie et al., 2013). Specifically, the historical MMLD ranges from approximately 140 m to 232 m. The MIROC5 model shows its two peaks in 1986 and 1990. The GFDL also peaks in 1990 for its historical run. With respect to the predicted results after 2021, there is



(A)



(B)

Figure 4.4: Annual (A) and seasonal (B) time series of the total net heat flux (Wm^{-2}) that are averaged over the HBC from 1981 to 2070 for 5 climate runs.

a slight increase of the MMLD from the ensemble, with a positive linear trend. The annual MMLD is predicted to rise by 4.87% from 172.19 m in 2021 to 180.57 m in 2070 (Figure 4.5). The future predictions of MIROC5 with RCP4.5 and RCP8.5 indicate the largest MMLDs among all the experiments, with the MMLD of the RCP8.5 experiment likely to be as deep as 220 m by the end of 2070.

The decrease in MMLD in the HBC observed in the recent decades (1981–2021) could be attributed to several physical factors. One possible explanation is the increase in freshwater input from river runoff and sea ice melt due to climate change. Freshwater input can create stratification by reducing the salinity of the surface layer, which in turn reduces the vertical mixing and leads to a shallow MMLD (Liang and Losch, 2018; Nummelin et al., 2016; Davis et al., 2016). Another important factor is the warming of the upper ocean due to climate change, which can have a significant impact on the MMLD. As the surface waters warm, their density decreases, making it more difficult for them to mix with the colder, denser water below. This can result in a shallower MMLD and limit the exchange of heat, freshwater, and nutrients between the surface and subsurface layers (Somavilla et al., 2017; Abdulla et al., 2018; Sallée et al., 2021).

Sea ice formation have influences on changes in mixed layer depth. As ice forms, salt is dumped into the surrounding seawater and raises upper ocean density, thereby weakening stratification and contributing to a deeper mixed layer (Eastwood et al., 2020). Over the future study period, sea ice in the HBC is projected to retreat rapidly from its concentration and thickness (as shown later in section 4.3.4). The reduction of ice in the future years (2021–2070) is likely to weaken stratification within the upper water column, which consequently leads to deeper mixed layers. The vertical stratification in the HBC is also related to the increased heat stored within the upper ocean over time, which coincides with the later study of ocean temperature and heat content in Section 4.3.5.1. Changes in surface heat fluxes across the air-sea interface contribute to the heat changes, with future winters experiencing the greatest increases in SAT and a corresponding decrease in downwelling heat fluxes at the ice-ocean interface (Ridenour et al., 2021; Lukovich et al., 2021). Changes in wind patterns can affect the mixing of the water column, and thus the depth of the mixed layer. In the HB region, increased westerly winds can enhance the mixing and deepening of the mixed layer. In

addition, ocean circulation patterns can affect the mixing of the water column and the depth of the mixed layer. Within the HBC, changes in the inflow of warm, saline water from the North Atlantic could increase the density gradient and lead to deeper mixing (Sallée et al., 2021; Ridenour et al., 2019a; Sandeep and Pant, 2019).

In addition to studying one-dimensional seasonal and annual MMLD trends, two-dimensional spatial structures can reveal a wealth of information. Figure 4.6 shows the five different distributions of the MMLD (MRI-CGCM3 historical and RCP4.5, MRI-CGCM3 RCP8.5, GFDL historical and RCP4.5, MIROC5 historical and RCP4.5, and MIROC5 RCP8.5) around the HBC individually. It is remarkable that, excluding the GFDL dataset which can reach as deep as ~ 170 m in the interior part of the bay, all others have MMLDs generally not larger than 150 m. Generally, MMLDs are deeper in the western HB than in the east. Additionally, seawater surrounding the Rankin Inlet indicates intensified vertical mixing. Such intensification of the mixing in this area can be attributed to the weaker stratification in March, the open water, polynyas and thus strong air-sea fluxes, as a result of brine rejection from continual ice formation. Evidence of the salt release from the ice to the ocean is that the maximum values of salinity in March (> 40 psu) on the top 50 m of the ocean are all found in this location (not shown), consistent with studies by Saucier et al. (2004); Burt et al. (2016). Such phenomenon of increased salinity can be attributed to the polynyas adjoining the Rankin Inlet (Saucier et al., 2004; Gunn, 2015; Kirillov et al., 2020), where northwesterly winds drive ice offshore (Saucier et al., 2004; Landy et al., 2017), opening water for strong heat loss (Morales Maqueda et al., 2004). This forms ice, leading to brine rejection. And then the process repeats, decreasing buoyancy and driving deeper mixed layers (Stewart and Barber, 2010; Granskog et al., 2011). As supported from one of the latest experiments conducted by Bruneau et al. (2021), within the polynyas of HB, the largest amount of ice occurred in the south of Rankin Inlet during the winter between 2002 and 2019, likely arising due to higher wind speeds over the south of Rankin Inlet than the north of it.

With respect to the mixing features in HS, the largest MMLD is expected to be over 200 m, which was found to have the greatest values in the GFDL and MIROC5 historical runs. These results are congruent the peaks of the MMLD time series shown in Figure 4.5. Here, the MMLDs are induced by the barotropic flow along the northern coast of HS that is consistent

with the conclusion from Ridenour et al. (2019a). The strongest vertical mixing phenomenon can be found around the southwestern side of Baffin Island and the area between the FB and the Southampton Island along the coastline of Melville Peninsula.

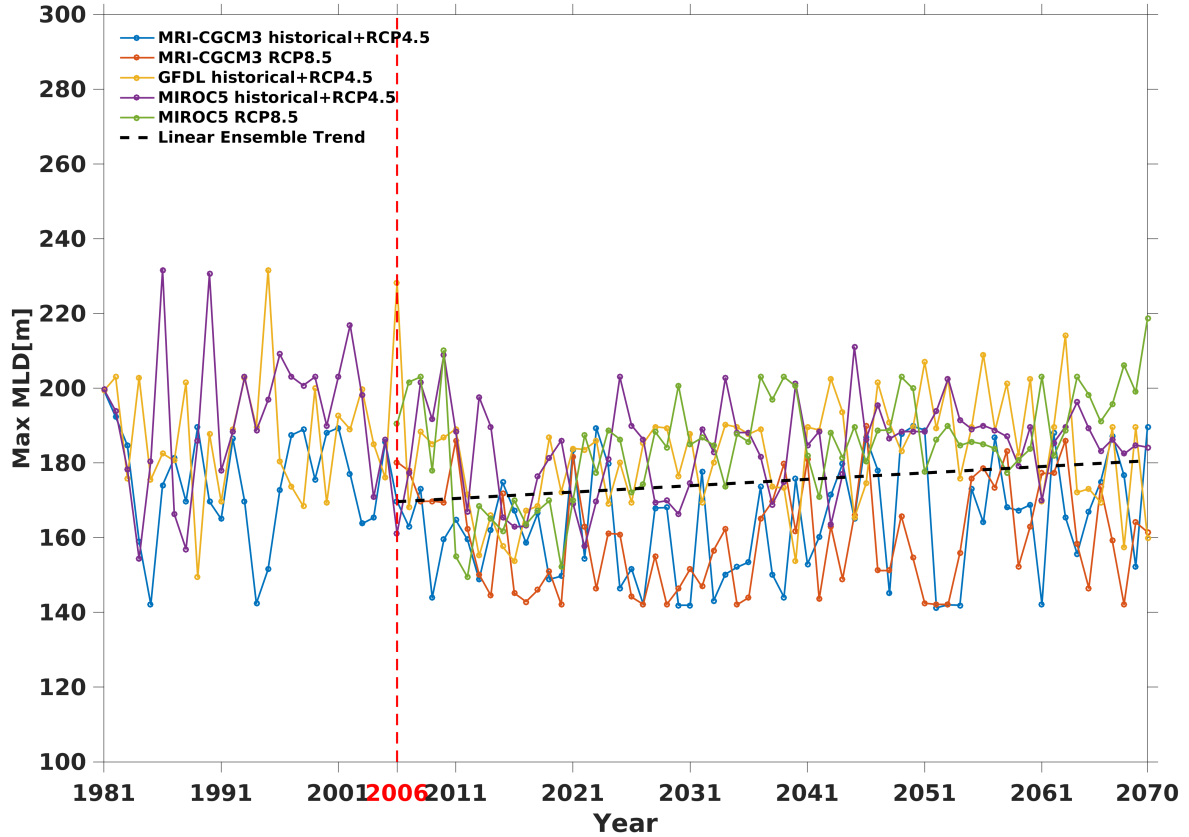


Figure 4.5: Annual maximum mixed layer depths (MMLDs; in m) in the HBC.

4.3.4 Sea Ice Properties

Within the HBC, the seasonal sea-ice cover can affect the ecology of the marine system, the animals and plants living in this region profoundly and significantly. The ice cover directly influences atmosphere-ice-sea connections and the conditions of sea ice is both an indicator of climate change and a crucial driver of regional climate (Hamilton, 2013). Therefore, many investigations, such as Gagnon and Gough (2005); Hochheim and Barber (2010); Andrews et al. (2017, 2018); Bruneau et al. (2021), have been conducted into the links between atmospheric forcing and the timing of freeze-up and breakup of ice. In light of the snow and ice cover in the HBC, the fate of solar energy from the sun to the surface of the Earth is largely

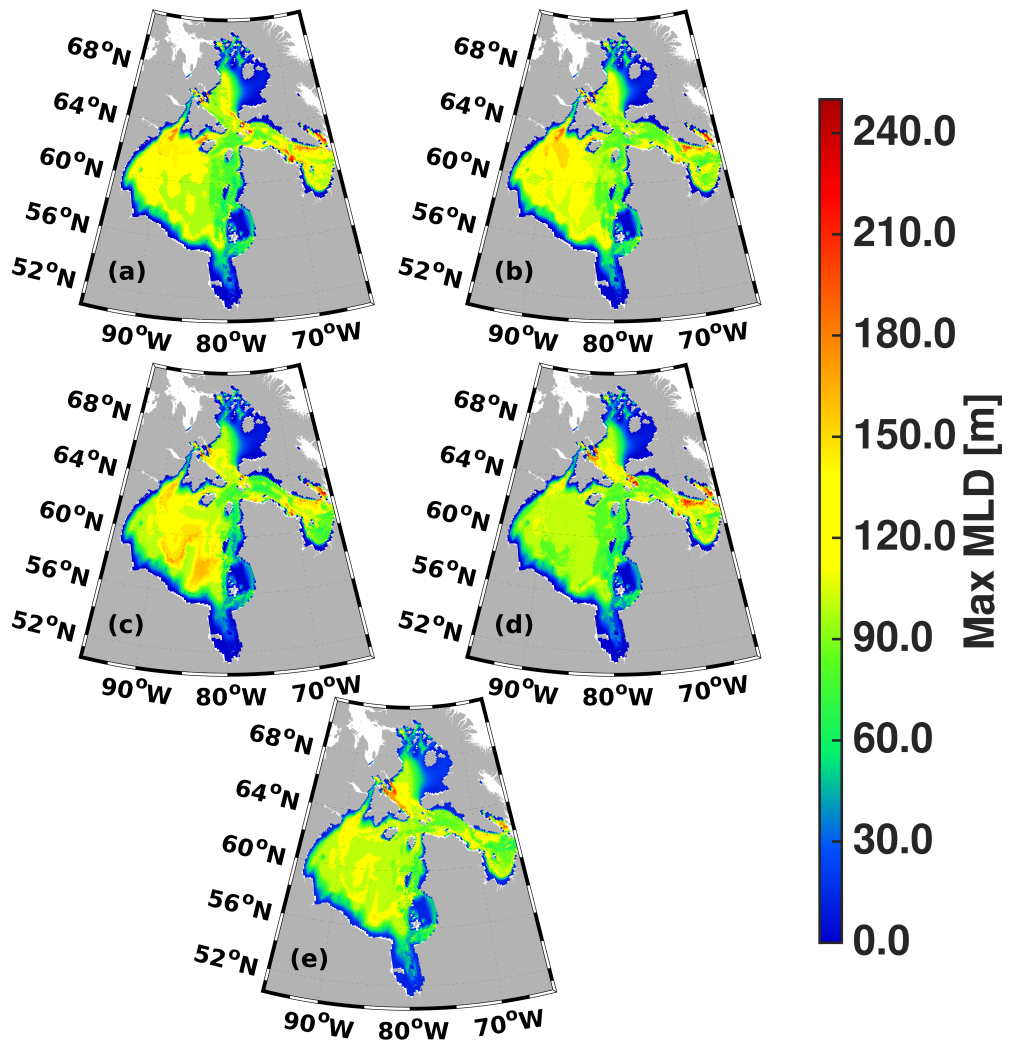


Figure 4.6: Annual MMLD spatial distributions for five model experiments (A) MRI-CGCM3 historical and RCP4.5, (B) MRI-CGCM3 RCP8.5, (C) GFDL historical and RCP4.5, (D) MIROC5 historical and RCP4.5, and (E) MIROC5 RCP8.5.

different from the area that the atmosphere directly communicate with the ocean. Typically, an ice-free sea surface receives about 90–95 % of solar radiation into the water body, while the surface covered by ice and snow is reflected about 80 % radiation back to the atmosphere. The received energy thus is able to speed up the ice melting process and delay the dates for ice generation during fall and winter. Besides, as the effects of increasing climate warming, this received energy increases, further advancing the melt dates and delaying the formation dates. All the processes leads to a longer open water season in the future (Stewart and Lockhart, 2005b; Hamilton, 2013). As one of the main sources of freshwater into the HBC, the melting of sea ice adds at an average volume of approximately 1500 km m^{-1} to the surface of the complex (Stewart and Lockhart, 2005b; Hamilton, 2013).

In terms of different types of sea ice within the HBC, multi-year ice (MYI) barely exists (Landy et al., 2017), though small extents of second-year ice is likely to be observed in Foxe Basin and then migrate into northeastern Hudson Bay (Gagnon and Gough, 2006; Tivy et al., 2011; Environment and Climate Change Canada). The majority can be observed as first-year ice (FYI) (with thickness typically ranging from 30 to 120 cm) and young and new ice (with thickness < 30 cm) (Stewart and Lockhart, 2005a; Tivy et al., 2011).

According to our study, in general, the annual and seasonal variations of sea ice concentration (SIC) and sea ice thickness (SIT) from naturalized (Figure 4.7) and regulated (Figure 4.8) model simulations are all found to decrease over the entire time period. The corresponding annual and seasonal statistics and trend analyses for each figure is listed in Table 4.1 and Table 4.2. In consideration of naturalized runs, the annual mean SIC (Figure 4.7A) is projected to reduce from $50 \pm 2\%$ for historical control to $39 \pm 9\%$ for future scenario, representing an overall 22% decrease. A linear declining trend through the entire 65-year future study period of $-0.28\% \text{ yr}^{-1}$ ($p < 0.05$) is found. The GFDL experiment among all ensemble members shows the largest decrease (-44%) of SIC since 1992, dropping sharply from 52% to the lowest point of 8% in 2061. Seasonal trends (Figure 4.7B; Table 4.2) are significantly different that fall SIC is from a historical mean of $3 \pm 2\%$ approaching to 0% by the end of 2070, which means a future extension of open water season can be as long as to the fall months (September to November). Meanwhile spring and winter SICs are projected to significantly decline. Specifically, SIC in spring is found to decline from a historical mean of $92 \pm 1\%$ to a

near-future mean of $80 \pm 3\%$ (-13%) and a far-future mean of $74 \pm 3\%$ (-20%). The amount of diminishing winter mean SIC is more than twice as large as that of spring, decreasing by -30% ranging from $81 \pm 5\%$ for historical period to $57 \pm 5\%$ for near-future period and by -43% when dropping to $46 \pm 5\%$ for far-future period. In winter, the experiment of GFDL forced by RCP4.5 is predicted to have the lowest proportion of ice cover in 2060, which is less than 10%.

Annual mean SIT (Figure 4.7C) of the 5-member ensemble of climate simulations is projected to be 0.37 ± 0.04 m in the near future (2030–2049) and 0.28 ± 0.04 m in the far future (2050–2070). Compared to the historical mean of 0.57 ± 0.07 m, the two future periods are expected to experience 35% and 51% reduction of ice thickness. Together, the whole future time frame (2006–2070) experiences a negative linear regression trend of 0.0042 m yr^{-1} ($p < 0.05$). Figure 4.7D and Table 4.2 reveal seasonal SIT features that the HBC is almost ice-free (the mean is only 0.012 m) during fall seasons over the whole study period. In spring, ice thickness decreases from the historical ensemble mean of 1.29 ± 0.12 m to 0.90 ± 0.07 m (-30%) and 0.73 ± 0.08 m (-43%) as the near- and far-future averages. The decline of SIT in winter months is larger, with the means of 0.46 ± 0.05 m and 0.34 ± 0.05 m for 2030–2049 and 2050–2070 from 0.70 ± 0.05 m for the mean of historical runs. The winter SIT prediction represents 34% and 51% losses with respect to its historical control.

Experiments with consideration of river regulation (given the anthropogenic intervention of dams, diversions, and reservoirs) share similar trends and variabilities with the unregulated counterparts, annually and seasonally over the study period. From Table 4.1 and 4.2, differences between naturalized and regulated regimes are less than 0.8% for means of ice concentration and 0.01 m for means of ice thickness, respectively. In terms of the variability of annual and seasonal ice properties for paired unregulated and regulated systems, it is quantified by the coefficient of variation (CV). The annual ice variabilities are relatively low of 0.14 for concentration and 0.21 for thickness. Nonetheless, there is an obvious seasonality for the two ice variables. The greatest variability seen in Fall is, $CV = 0.44$ for SIC and $CV = 0.45$ for SIT, following $CV = 0.18$ or 0.17 for SIC and $CV = 0.23$ or 0.22 for SIT in winter. The lowest variability is during spring for both ice concentration and thickness, with $CV = 0.081$ and $CV = 0.18$, respectively. These highly consistent results between the two

regimes show that sea ice properties in the HBC are barely affected by the construction of river regulation. And thus the changes are driven by climate change.

The spatial and regional analyses of sea ice distribution are also carried out by considering outputs from different CMIP5-forced experiments. In terms of the distribution of annual SIC (Figure 4.9A), as the representative concentrations of greenhouse gases in simulations are getting higher, sea ice concentration is getting lower over the entire region of HBC, which means less ice coverage is found in the complex. Generally, with stronger atmospheric forcing in response to climate change, the decline of ice within the whole complex starts from southeast to northwest. The four subregions constituting the HBC demonstrate different ice conditions. On the one hand, James Bay experiences the lowest percentage of SIC over all simulations, values always less than 45%. On the other hand, from Figure 4.9A, Foxe Basin is typically with the largest ice coverage (60% – 75%) over the years. The highest SIC (75%) is observed along the northwest coasts of Foxe Basin, especially around the Prince Charles Island. Similar results were documented in previous studies and Foxe Basin is rarely ice-free until September with its north mostly covered by landfast ice and its south dominated by pack ice (Andrews et al., 2018; Ford et al., 2009; Prinsenberg, 1986a). Within Hudson Strait, the majority of ice is located in the northern part along Baffin Island, where maintaining polynyas, and the south side of Ungava Bay. The SIC in the last subregion Hudson Bay ranges from 26% to 50%. Under the circumstances of climate warming, Hudson Bay experiences the greatest differences in ice concentration between its southeast and northwest sides. Among all individual experiments, the GFDL forced by RCP4.5 exhibits the largest variability of SIC, annual averages of less than 50% over the entire region for 2006–2070. This spatial trend in GFDL RCP4.5 is also consistent with the counterpart in annual SIC time series (Figure 4.7A).

In consideration of regional SIC distributions near winter months (January–March) (Figure 4.9B), the HBC is completely ice frozen for historical time frame (1981–2005). As time goes by plus stronger greenhouse gas forcing, the SIC drops to as low as approximately 70%, which is found near the offshore region in southern HB, located to the west of the Belcher Island (BI). During the three months, no matter historical or future periods, the SIC in Foxe Basin remains about 99% that the area is fully ice covered.

Research from Gagnon and Gough (2006) analyzing datasets based on ice thickness mea-

measurements at seven landfast ice locations in the HBC for 45 years (1958—2003) showed that the mean maximum ice thickness in HB was 1.75 m. The maximum ice thickness was found to increase from south to north and west to east, as a result of the temperature gradient across HB and the ice motion toward the east of HB driven by prevailing westerly winds (Gagnon and Gough, 2006). The ice is not only influenced by temperature and winds, but also by other local variations such as current, freshwater transport, precipitation, and large tidal ranges (Environment and Climate Change Canada; Gagnon and Gough, 2006; Laidler and Elee, 2008; Galley et al., 2012).

Our results in Figure 4.10A show annual characteristics of ice thickness. Overall, there is a significant trend towards thicker ice in northern HBC (mainly within FB) and thinner ice in the south of the complex, where the lowest annual ice thickness is observed in JB, ranging from 0 m to 0.6 m for all simulations. Thinner mobile pack ice locates in the central HB with a decrease of annual thickness from approximately 0.5 m for historical time frame to less than 0.2 m for future scenarios. While thicker ice along HB coasts varies from about 1 m to 0.4 m for historical and future experiments, respectively. Sea ice floating on HS does not exceed 1 m for long-term annual mean. The maximum value of annual SIT reaching 2.3 m is found near Bowman Bay along southeastern coast of FB. According to previous research from Andrews et al. (2018); Ford et al. (2009), even if typically having the shortest open water season, Foxe Basin is covered mostly by first-year ice, rarely more than 1.5 m in thickness. Frequently, second-year and multi-year ice is found first in northern FB, then rapidly spreading southward along the coasts to completely cover FB early in November (Environment and Climate Change Canada; Andrews et al., 2018; Ford et al., 2009). Thus, the accumulated highest value of ice thickness around Bowman bay is probably from second-year or multi-year ice.

With similar trends to annual distributions, the SIT from January to March in HBC is simulated to be as large as 4.25 m around Bowman bay. The other regions among all historical and future scenarios are covered with ice more than 1 m in thickness except for an area located in the southeastern part of HB that is ambient to the northwest of Belcher Islands (BI) with thinner ice cover (< 0.5 m). Such thinner-ice area is also with a lower percentage of ice concentration, corresponding with the estimated results in Figure 4.9B.

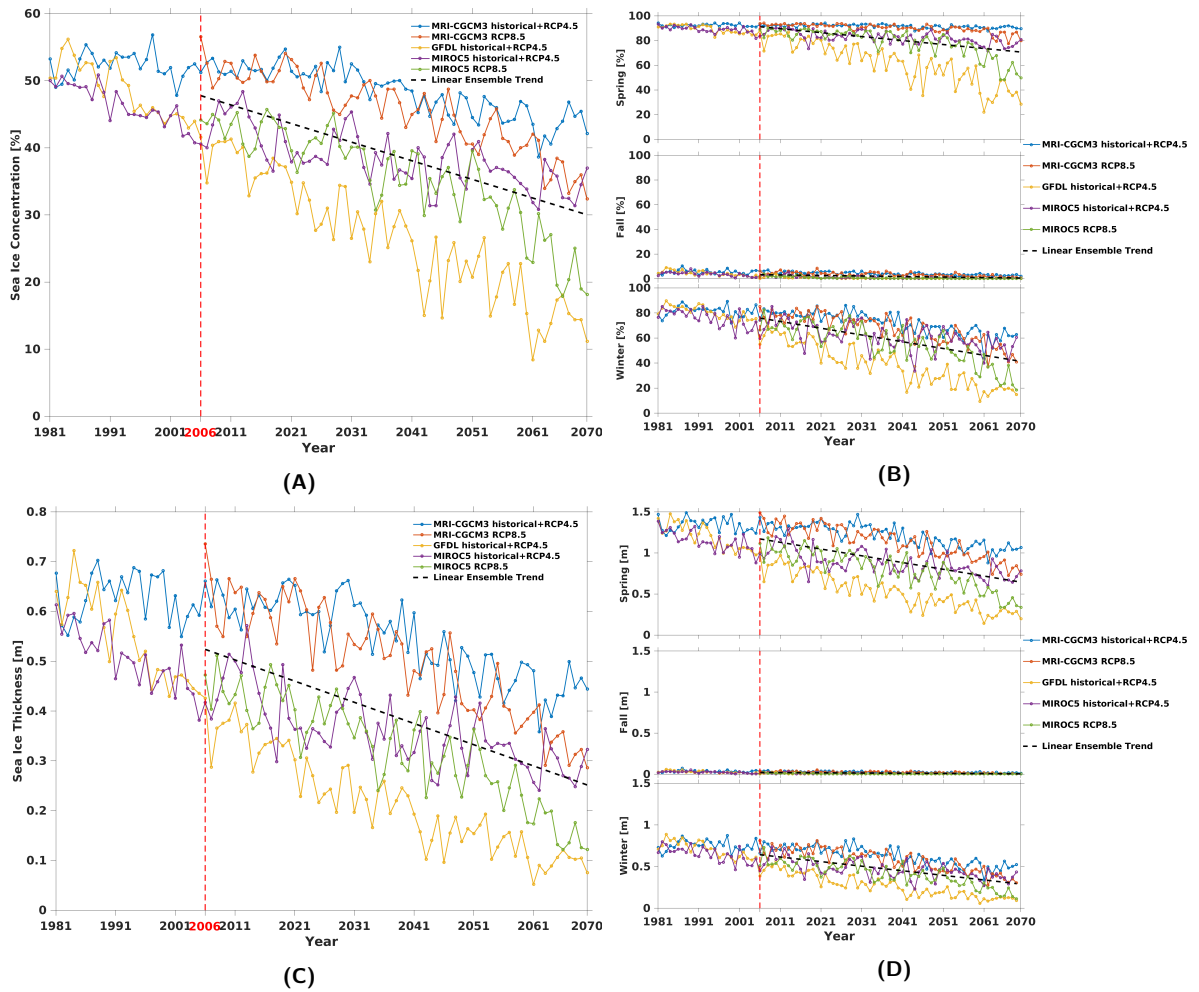


Figure 4.7: Time series of annual (A) sea ice concentration (SIC; in %) and (B) sea ice thickness (SIT; in m) over the HBC from 1981 to 2070 for 5 naturalized runs only influenced by climate change. Seasonal time series of the two variables are given in (B) and (D).

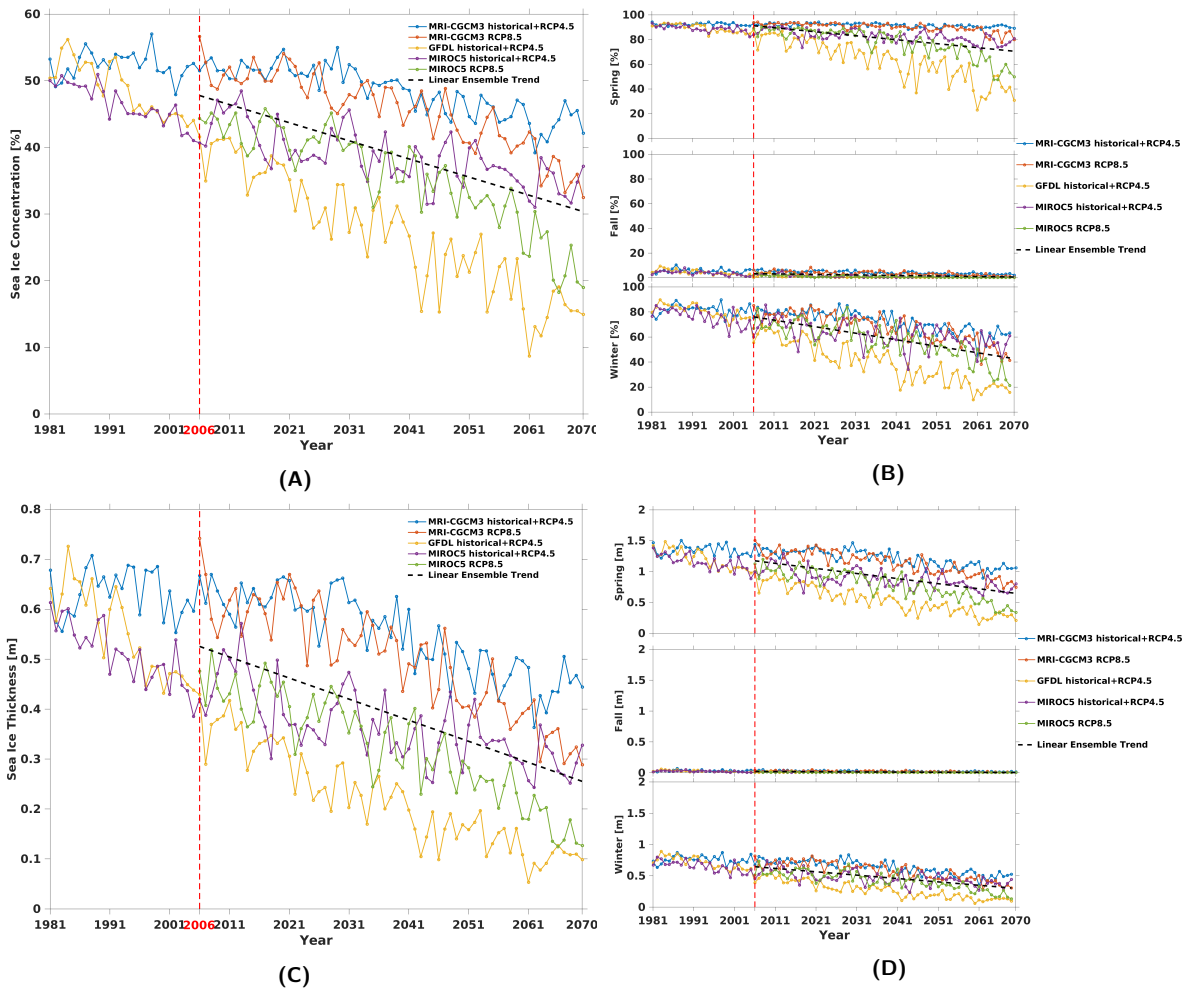


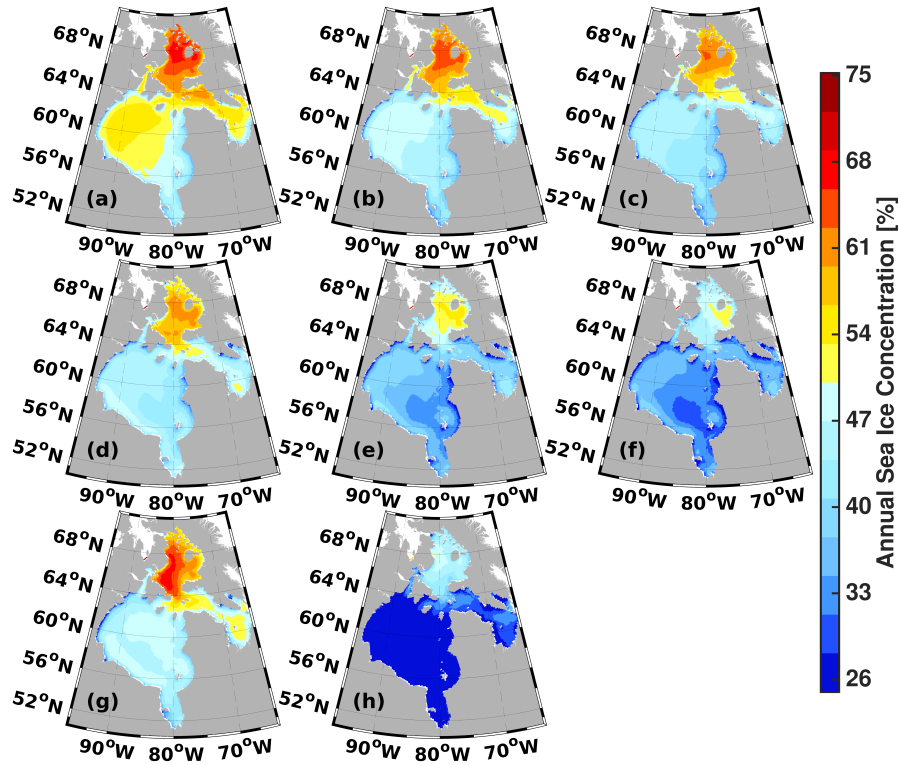
Figure 4.8: Similar to Figure 4.7 but considering impacts of both river regulation and climate change. Time series of annual (A) sea ice concentration (SIC; in %) and (C) sea ice thickness (SIT; in m) over the HBC from 1981 to 2070 for 5 regulated runs. Seasonal time series of the two variables are given in (B) and (D).

Table 4.1: The mean, standard deviation (SD), coefficient of variation (CV) in annual ice concentration and ice thickness time series with slope and intercept (Inter) of the linear regressions (The trend starts in year 2006).

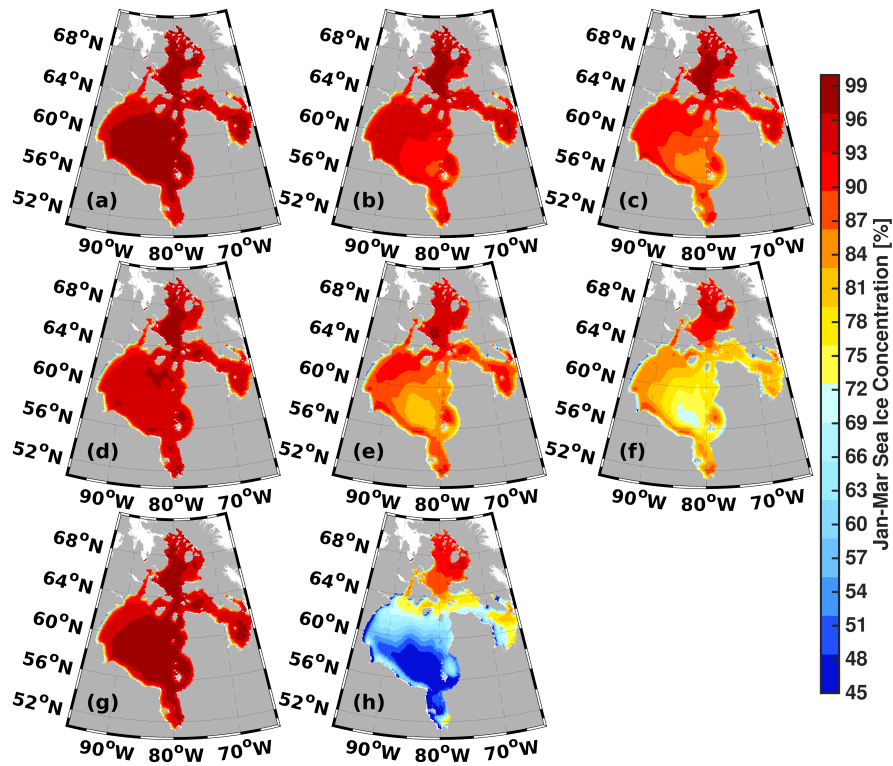
Variables	Climate runs	Mean	SD	CV	Slope	Inter
		(%)	(%)		(% yr^{-1})	(%)
Ice concentration	Naturalized	38.91	5.41	0.14	-0.28	47.78
	Regulated	39.08	5.30	0.14	-0.27	47.78
Ice thickness	Climate runs	Mean	SD	CV	Slope	Inter
		(m)	(m)		(m yr^{-1})	(m)
Ice thickness	Naturalized	0.39	0.083	0.21	-0.0043	0.52
	Regulated	0.39	0.082	0.21	-0.0042	0.53

Table 4.2: The mean, standard deviation (SD), coefficient of variation (CV) in spring (MAM), fall (SON), and winter (DJF) ice concentration and ice thickness time series with slope and intercept (Inter) of the linear regressions (The trend starts in year 2006).

Variables	Climate runs	Seasons	Mean	SD	CV	Slope	Inter
			(%)	(%)		(% yr^{-1})	(%)
Ice concentration	Naturalized	Spring	80.96	6.60	0.081	-0.32	91.22
		Fall	2.00	0.88	0.44	-0.043	3.37
		Winter	58.92	10.56	0.18	-0.54	75.94
	Regulated	Spring	80.88	6.59	0.081	-0.32	91.21
		Fall	2.02	0.88	0.44	-0.043	3.38
		Winter	59.70	10.23	0.17	-0.52	76.13
Ice thickness	Climate runs	Seasons	Mean	SD	CV	Slope	Inter
			(m)	(m)		(m yr^{-1})	(m)
Ice thickness	Naturalized	Spring	0.91	0.16	0.18	-0.0082	1.17
		Fall	0.012	0.0055	0.45	-0.00027	0.021
		Winter	0.47	0.11	0.23	-0.0055	0.64
	Regulated	Spring	0.91	0.16	0.18	-0.0082	1.17
		Fall	0.012	0.0055	0.45	-0.00026	0.021
		Winter	0.48	0.10	0.22	-0.0054	0.65

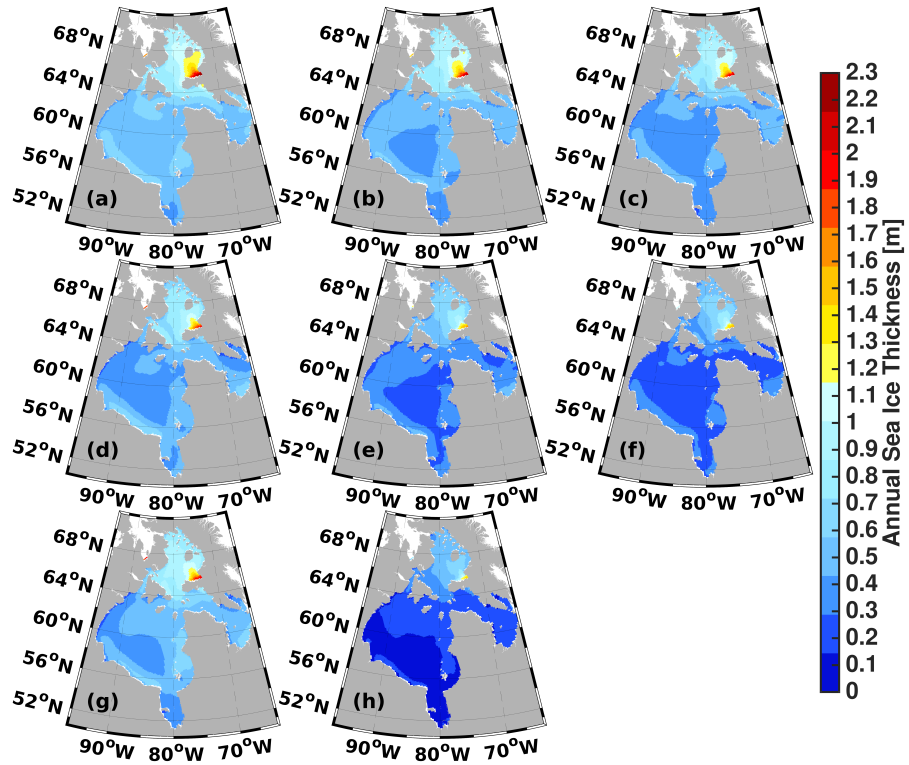


(A)

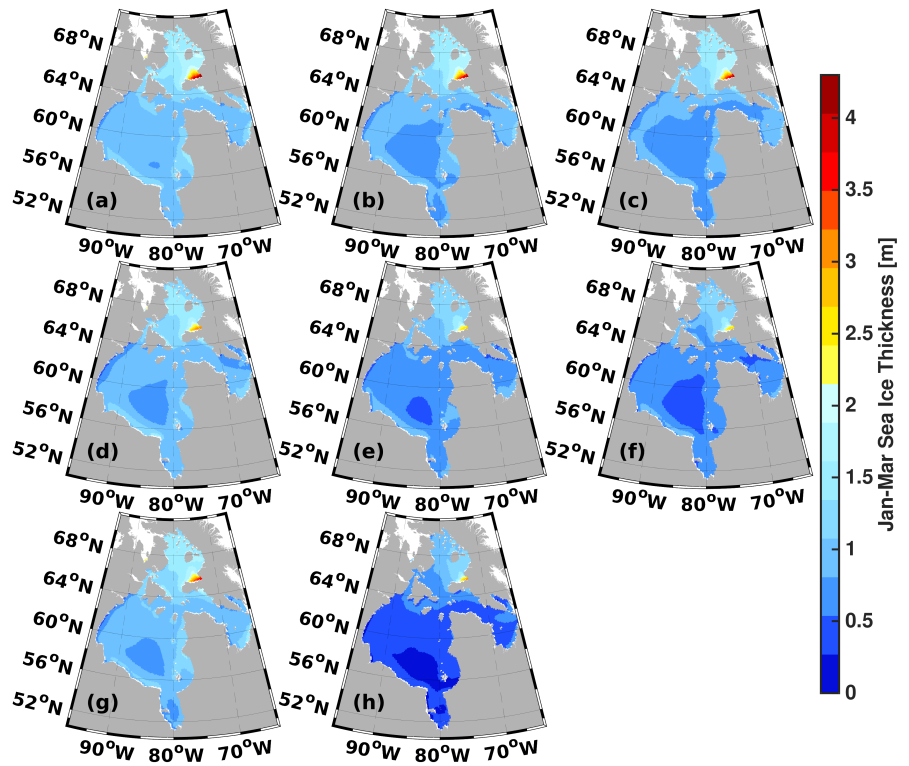


(B)

Figure 4.9: Spatial distributions of (A) annual and (B) January–March sea ice concentration (SIC; in %) in the HBC. Shown for outputs from MRI-CGCM3 (top: a, b, c), MIROC5 (middle: d, e, f), and GFDL (bottom: g, h). Columns from left to right represent historical forcing simulations for 1981–2005, RCP4.5 forcing simulations for 2006–2070, and RCP8.5 forcing simulations for 2006–2070.



(A)



(B)

Figure 4.10: Spatial distributions of (A) annual and (B) January–March sea ice thickness (SIT; in *m*) in the HBC. Shown for outputs from MRI-CGCM3 (top: a, b, c), MIROC5 (middle: d, e, f), and GFDL (bottom: g, h). Columns from left to right represent historical forcing simulations for 1981–2005, RCP4.5 forcing simulations for 2006–2070, and RCP8.5 forcing simulations for 2006–2070.

4.3.5 Oceanic Properties

4.3.5.1 Temperature and Heat Content

Approximately 90% of the heat built up in the climate system has been found to be received by the global ocean since 1970 (Von Schuckmann et al., 2020). With the acceleration of climate warming, it is increasingly critical to understand the variations of ocean temperature and heat content (Sohail et al., 2021). Thus, to investigate how these two variables in the HBC could respond to the changing climate and river regulation, we selected two-layer depths (top 50 m and 250 m) for study. Here, the temperature-determined heat content (HC) is vertically integrated as:

$$HC(x, y) = \int_{z=-h}^0 \rho_w C_p (T(x, y, z) - T_{\text{ref}}) dz \quad (4.2)$$

where $-h$ and 0 stands for the bottom and surface of the layer being studied, z is the vertical coordinate, $T(x, y, z)$ is the temperature at a given point, T_{ref} is a reference temperature (chosen as -1.8 °C, which is the freezing point of sea ice), ρ_w is the density of ocean water (a mean density averaged from all data sets within the depth of 50 m/250 m), and $C_p = 4000$ J/kg/K is the ocean specific heat.

Integrating equation (4.2) within area of the HBC, the total heat content can be computed:

$$HC = \iiint_{z=-h}^0 \rho_w C_p (T(x, y, z) - T_{\text{ref}}) dx dy dz \quad (4.3)$$

where x and y is the horizontal coordinates.

Figure 4.11 presents temporal distribution characteristics of annual and seasonal ocean temperature and heat content affected by climate change alone, whereas Figure 4.12 is the counterpart of Figure 4.11 with the additional consideration of regulated rivers. Specific statistical information of these time series can be found in Table 4.3 and 4.4. The annual temperature averaged over the top 50 m (Figure 4.11A) in the HBC is projected to arise from -0.02 °C in the historical mean to 0.85 °C (+39.4%) in the near-future period and 1.30 °C (+59.9%) in the far-future period. The monotonically increasing trend of the entire future time frame is 0.02 °C yr⁻¹ ($p < 0.05$) that the ensemble average of temperature is

anticipated to increase by 1.43 °C. Figure 4.11B reveals that the rate of temperature over top 50 m in fall is expected to be 0.037 °C yr⁻¹, as the largest seasonal increase peaking in 2070 (4.92 °C). Meanwhile, a gradual rise (+1.11 °C) is predicted to warm the ocean during winter from 2006 to 2070. In spring months, ocean temperature over the upper 50 m persists a relative steady condition with a mean value of -1.50 °C. Within the deeper top 250 m, annual temperature (Figure 4.11E) shares a similar trend with the counterpart on top 50 m but the future ensemble mean reduces by 0.68 °C (from 0.78 °C on top 50 m to 0.10 °C on top 250 m). Compared to the historical control of temperature over the top 250 m, there is a 126.9% increase in the near-future period and a sustained increase of 189.7% in the far-future period. Rates of variations in three seasons of ocean temperature on the upper 250 m (Figure 4.11F) are comparable to that on the upper 50 m. Unlike the spring and winter where only minor decreases are observed in the future ensemble mean from top 50 m to top 250 m, the fall temperature declines notably from 3.69 °C to 1.54 °C (-58.3%). Among all individual experiments estimating ocean temperature, the GFDL simulation shows the greatest warming over the 90-year study period while the two MRI-CGCM simulations (RCP8.5 and RCP4.5) experience the slowest rate of increase in ocean temperature. Moreover, after river regulation, the annual variabilities of ocean temperature on the upper 50 m and the upper 250 m are found to decrease by 5.6% and 42.8%, respectively. This finding accords with earlier observations in the Eurasian Ob and Yenisei rivers from Yang et al. (2004a,b), which concluded that flow regulation generally suppresses variability (quantified by CV) compared to matching unregulated rivers (Déry et al., 2016).

As computed based on seawater temperature (shown in Equation (4.3)), annual and seasonal trends of heat content share great similarities with that of corresponding temperature. Heat content within the top 50 m water column presents sustained growth both annually and seasonally. From historical frame to near-future and far-future periods, annual mean (Figure 4.11C) increases by 48.3% and 73.4%. The fall heat content over the top 50 m has a mean of 1.22×10^{21} J and a rate of 8.18×10^{18} J yr⁻¹ for the future study period, standing for the largest increase among three seasons. The mean value of winter heat content is found to peak in 2070 reaching 3.44×10^{20} J. In contrast to the temperature which declines with depth in the HBC, more heat content is observed to be stored within the increasing depth. This

is because of the integration method we applied for computing the heat content. Over the top 250 m, the annual heat content (Figure 4.11G) increases by 55.0% and 82.3% from the historical 1981–2005 to the 2030–2049 and 2050–2070 study periods, respectively. The seasonal variability on the upper 250 m can be found in Figure 4.11H and Table 4.4. The spring heat content has a future mean of 4.26×10^{20} J with a slope of 4.00×10^{18} J yr⁻¹. During fall months, there is more heat absorbed into the ocean as a mean of 1.82×10^{21} J from 2006 to 2070. For the last 65-year study period, given the rapid retreat of sea ice cover, the heat content in winter is found to be even +69.7% more than that in fall. Similar to the annual and seasonal characteristics of individual experiments in temperature, the GFDL output in heat content always depicts the largest increase ($> +150\%$) from year 1981 to 2070 among the five experiments.

From the above analysis, it is found that the basin warms with a warming climate, increasing temperature and heat content, and reducing ice concentration and thickness. In regard to the river regulation, there are little influences of regulated rivers on any of the heat impacted quantities.

4.3.5.2 Salinity and Freshwater Content

To estimate the salt-determined stratification and its changes in the HBC, characteristics associated with freshwater input to the ocean are intensely studied (Saucier and Dionne, 1998b; Stewart and Lockhart, 2005b; St-Laurent et al., 2012; Ridenour et al., 2019b). By freshwater, this refers not merely to river runoff or atmospheric precipitation (e.g., rain or snow), but within an oceanographic context, refers to a mass of water with significantly less salt content than surrounding waters. In the HBC, the reference salinity (S_{ref}), following an averaging over the 1981–2070, 90-yr period, is measured at 33. Following Aagaard and Carmack (1989), liquid freshwater content (FWC) can then be estimated at a given location (x, y) by the following equation:

$$FWC(x, y) = \int_{z=-h}^0 1 - \frac{S(x, y, z)}{S_{\text{ref}}} dz \quad (4.4)$$

where $-h$ is the depth of the water column, $S(x, y, z)$ is the salinity and z is the vertical coordinate.

Integrating equation (4.4) within area of the HBC, the freshwater storage (FWS) can be estimated:

$$FWC = FWS = \iiint_{z=-h}^0 1 - \frac{S(x, y, z)}{S_{\text{ref}}} dx dy dz \quad (4.5)$$

Here, it is noted that a reference value is just used for comparison. As none of the ocean water can be considered as absolutely fresh, the FWC is calculated to estimate how much freshwater would be needed to change water of a given salinity to that reference.

As shown in Figure 4.13 with naturalized river runoff, the ensemble means of salinity and freshwater content present opposite trends. Specifically, the ensemble means of annual salinity in the top 50 m and 250 m ocean layers only decrease by 0.2 and 0.3, respectively, which corresponding to the increase of freshwater content by 211.25 km³ and 728 km³ from 2006 to 2070. Over this future study period, higher ocean salinities (+2.4%) and freshwater contents (+33.5%) are found in deeper ocean layer from the upper 50 m to 250 m. Unlike the previous oceanic variables which are well represented by the ensemble mean of all scenarios, there are large discrepancies of salinity and freshwater content among the five ensemble members. The top 50 m and 250 m annual salinity under naturalized regimes (Figure 4.13A and 4.13E) shows that MRI-CGCM3 experiments forced by RCP4.5 and RCP8.5 both suggest strong freshening of the HBC. The reduction of top 50 m annual salinity for MRI-CGCM3 RCP8.5 simulation is suggested to be the largest of ~ 1.25 from 2006 to 2070. However, other simulations depict slight variations or even a gradual increase (~ 0.50 in GFDL RCP4.5 naturalized run) in the top 50 m ocean salinity. What stands out among the future ensemble members is the MIROC5 RCP8.5, where salinity is projected to decline rapidly to a low point of 31.25 in 2029 and then rise to 31.88 at the end of 2070. In terms of the seasonal changes in salinity (Figure 4.13B and 4.13B), the ensemble and individual trends are similar to their annual counterparts. In contrast to the characteristics of trends in salinity, the changing trends in each experiment of freshwater content are reversed. For instance, the largest increase of top 50 m freshwater content among all future runs is from MRI-CGCM3 RCP8.5, which suggests a ~ 1800 km³ growth from 2006 to 2070.

Given the regulated rivers that involve water management for hydropower production, trends of individual simulations are expected to share better similarities with that of their relevant ensemble means, which can be observed in Figure 4.14. With regulated river runoff, the reduction of ensemble means of annual salinity in the top 50 m and 250 m ocean columns over the future period are slightly larger than the same conditions with unregulated rivers, as 0.39 and 0.38, respectively. While there is no indication for the increase of the HBC salinity, the trends in freshwater content of all regulated ensemble members in future period are positive, where means of the top 50 m and 250 m FWCs are suggested to increase by 564.20 km³ and 1225.25 km³ from 2006 to 2070.

Based on these findings, we make a conclusion that the turbulence of the salinity and freshwater are more intensive than that of the other sea-ice and oceanic quantities. On the other hand, we shall mention that the variations of freshwater content and salinity are not consistent in different members of the ensemble. This is because such variations depend on how the hydrological cycle for the climate model changes, especially for the salinity, which relies on how the climate scenario's precipitation evolves.

Regulation impacts on these two variables are secondary, but do play a role in the freshwater budget. To be more specific, the differences in salinity and freshwater content between naturalized and regulated regimes are inferred to be associated with the freshwater residence time and the timing of the discharge. More freshwater inflow can be found within HB than the outflow transported via HS during the years with strong river discharges. Such increased freshwater decreases the value of salinity and extends the residence time. Years with weak river discharges are projected to have the opposite effect.

The findings suggest that the turbulence of the salinity and freshwater is more significant in the upper 50 m of the ocean layer, while the deeper layers remain more stable. The large discrepancies of salinity and freshwater content among the ensemble members indicate that the results are uncertain and sensitive to the choice of the climate model.

4.4 Discussion and conclusion

One overall objective in this study was designed to understand the influences of climate change and river regulation using ocean and atmospheric modelling in the HBC. To summarize, we conclude the results from above analysis that:

- (1) The surface air temperature and precipitation are linked with the ocean and ice properties. Compared to the melting ice and river runoff, precipitation makes less contributions to the freshwater changes.
- (2) In the HBC, the MMLDs can reach ~ 230 m along the north side of HS. This result is related to the loss of sea-ice and the exposure of the surface water to cold winter conditions, that drive deep mixing. However, augmented freshwater from rivers and ice melting are projected to lead to slightly shallower mixed layers in the future (2006–2070), compared to historical period (1981–2005).
- (3) With the regulation of rivers, higher volume of freshwater was transported into the HBC. As the global warming intensifies, attributed to different representative greenhouse gases concentrations (RCP4.5 and RCP8.5), it was observed that a dramatic increase in both freshwater and heat content is projected. However, a steep decrease in sea ice thickness (~ 0.3 m) and concentration ($\sim 22\%$) by 2070 will be indicative of the strong warming effects.
- (4) The temperature of the HBC will warm over the 65-year future period and sea-ice concentration and thickness in the complex will significantly decrease over the next 50 years. However, changing from naturalized to regulated river runoff has little impact on the warming of ocean temperature and the averaged sea ice variations. In other words, river regulation has little impact on any of these heat impacted quantities.
- (5) The variations of salinity and FWC are found to be highly relevant to different members of the ensemble, which is attributed to how the climate model's hydrological cycle evolves. In addition, changes in inflow and residence time affect the overall freshwater budget changes. The differences in salinity and freshwater content between naturalized

and regulated regimes are inferred to be associated with the freshwater residence time and the timing of the discharge. These two factors are regarded at least as important as the total long term freshwater input for the salinity within the HBC.

The limitations of the study are also found as follows:

- (1) The accuracy of representing the amount of river flow in the simulations is inadequate. The representation of river discharge relies on data from the hydrological model, which is influenced by various factors including dam operations, precipitation patterns across the continent and other complex processes that may not have been fully considered.
- (2) The bathymetric details of the Hudson Bay are not well-established, leading to uncertainty that can affect the accuracy of tidal simulations.
- (3) The sea ice model utilized in this study has potential for improvement. Incorporating a more advanced sea ice model could allow for a more comprehensive analysis of additional variables such as ice fluxes.

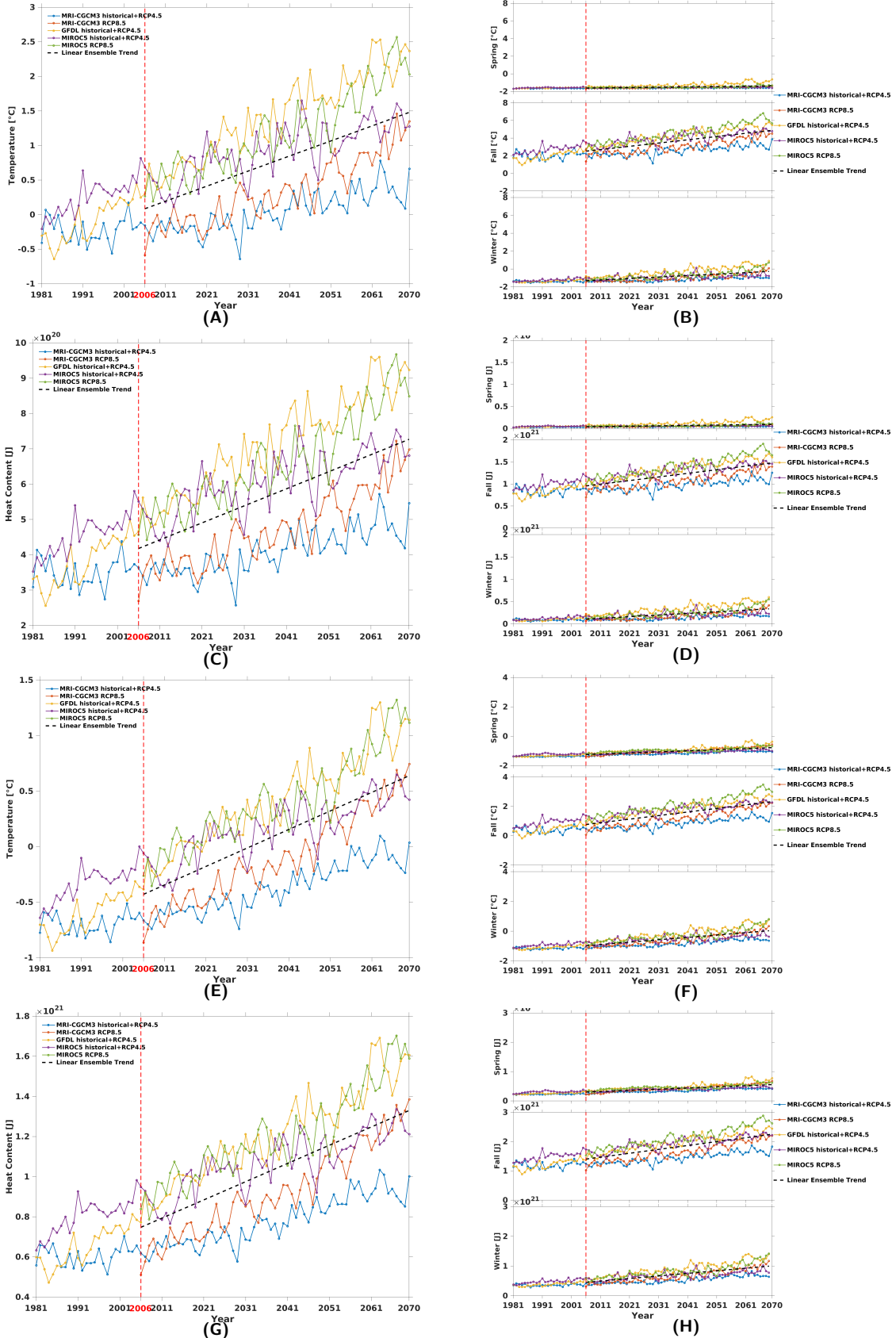


Figure 4.11: Annual (left column) and seasonal (right column) time series of temperature (T ; in $^{\circ}\text{C}$) and heat content (HC ; in J) over the HBC from 1981 to 2070 for 5 naturalized runs only influenced by climate change. Upper panels (A-D) depict the two variables averaged on top 50 m and lower panels (E-H) depict the two variables averaged on top 250 m.

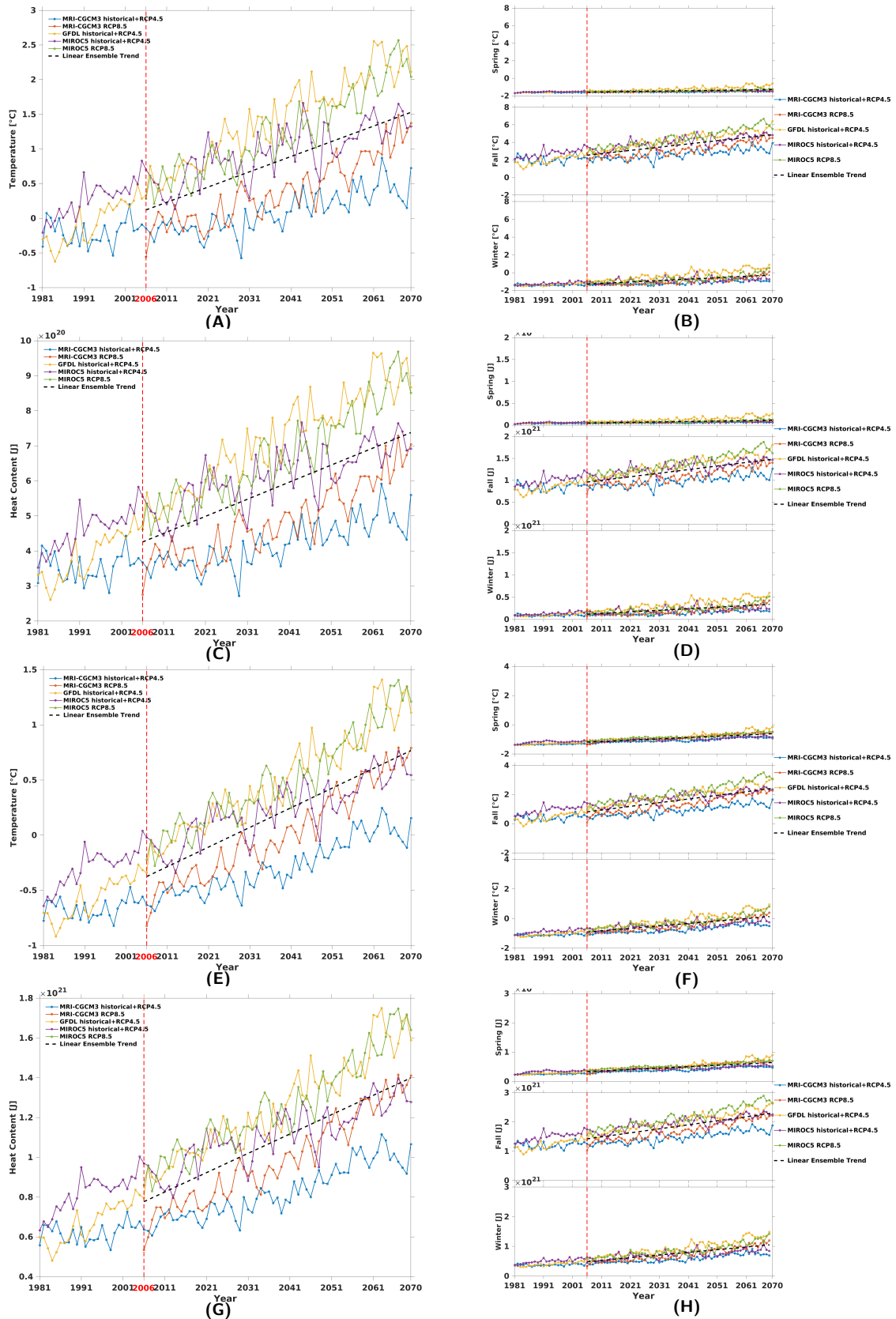


Figure 4.12: Similar to Figure 4.11 but considering impacts of both river regulation and climate change. Annual (left column) and seasonal (right column) time series of temperature (T ; in $^{\circ}\text{C}$) and heat content (HC ; in J) over the HBC from 1981 to 2070 for 5 regulated runs. Upper panels (A-D) depict the two variables averaged on top 50 m and lower panels (E-H) depict the two variables averaged on top 250 m.

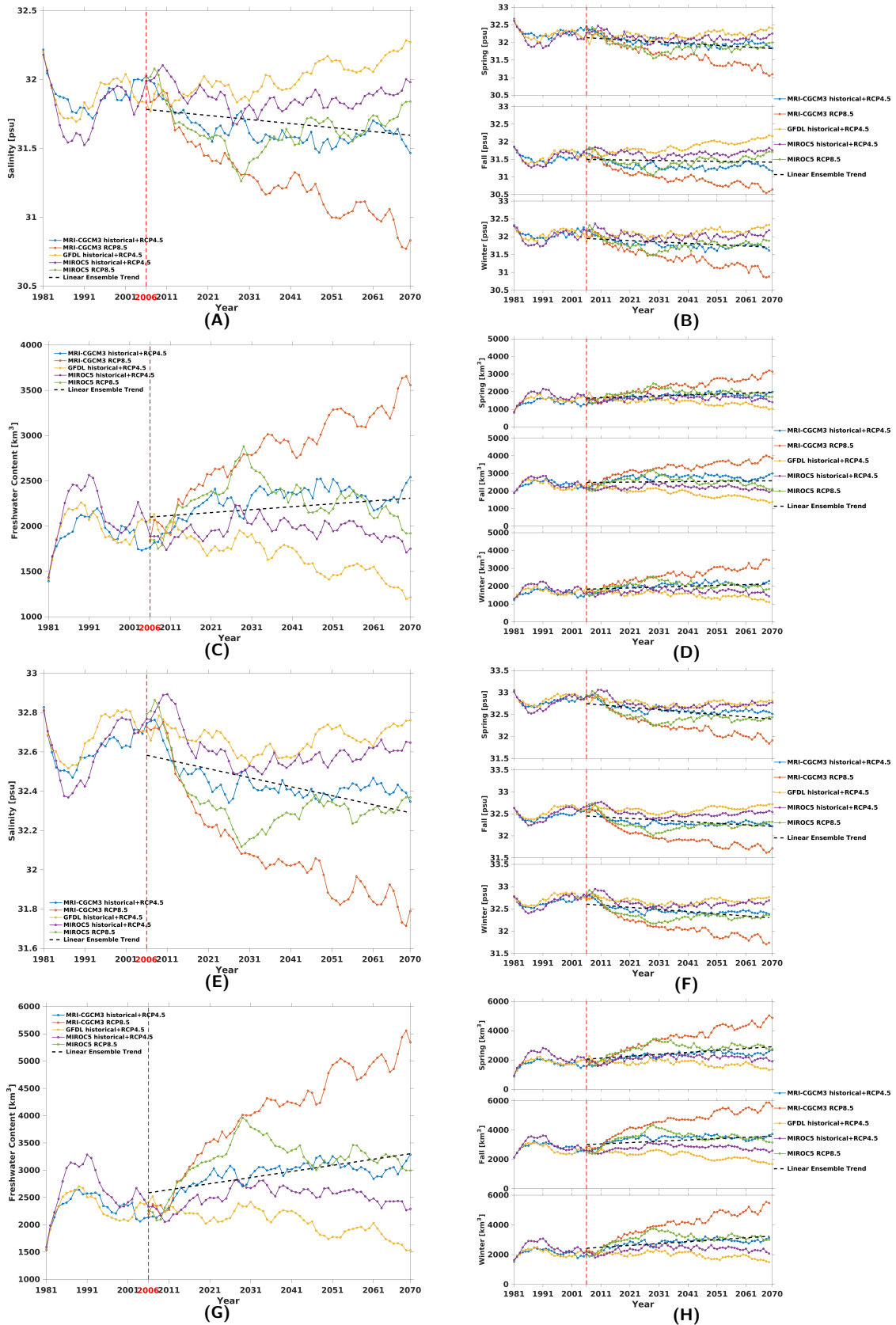


Figure 4.13: Annual (left column) and seasonal (right column) time series of salinity (S ; in psu) and freshwater content (FWC; in km^3) over the HBC from 1981 to 2070 for 5 naturalized runs only influenced by climate change. Upper panels (A-D) depict the two variables averaged on top 50 m and lower panels (E-H) depict the two variables averaged on top 250 m.

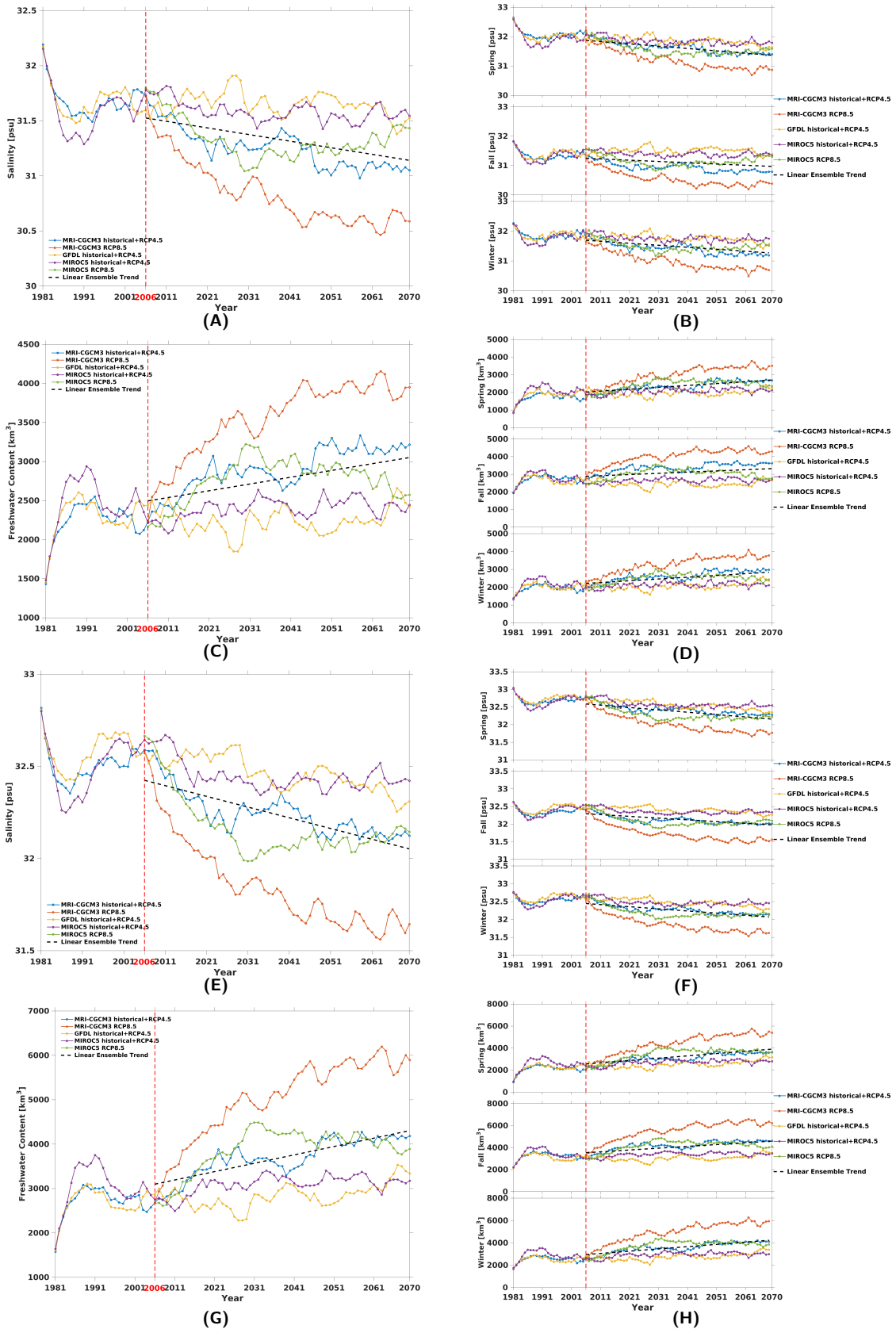


Figure 4.14: Similar to Figure 4.13 but considering impacts of both river regulation and climate change. Annual (left column) and seasonal (right column) time series of salinity (S ; in psu) and freshwater content (FWC; in km^3) over the HBC from 1981 to 2070 for 5 regulated runs. Upper panels (A-D) depict the two variables averaged on top 50 m and lower panels (E-H) depict the two variables averaged on top 250 m.

Table 4.3: The mean, standard deviation (SD), coefficient of variation (CV) in annual heat content, temperature, freshwater content, and salinity time series with slope and intercept (Inter) of the linear regressions (The trend starts in year 2006).

Variables	Climate runs	Depth (m)	Mean (J)	SD (J)	CV	Slope (J yr ⁻¹)	Inter (J)
Heat content	Naturalized	50	5.72×10^{20}	9.34×10^{19}	0.16	4.83×10^{18}	4.18×10^{20}
		250	1.04×10^{21}	1.75×10^{20}	0.17	9.10×10^{18}	7.48×10^{20}
	Regulated	50	5.82×10^{20}	9.41×10^{19}	0.16	4.88×10^{18}	4.26×10^{20}
		250	1.09×10^{21}	1.86×10^{20}	0.17	9.72×10^{18}	7.77×10^{20}
	Climate runs	Depth (m)	Mean (°C)	SD (°C)	CV	Slope (°C yr⁻¹)	Inter (°C)
Temperature	Naturalized	50	0.78	0.42	0.54	0.022	0.086
		250	0.10	0.32	3.06	0.017	-0.43
	Regulated	50	0.82	0.42	0.51	0.022	0.12
		250	0.20	0.34	1.75	0.018	-0.37
	Climate runs	Depth (m)	Mean (km³)	SD (km³)	CV	Slope (km³yr⁻¹)	Inter (km³)
Freshwater content	Naturalized	50	2204.82	120.36	0.055	3.25	2100.79
		250	2943.51	281.94	0.096	11.20	2585.24
	Regulated	50	2773.38	187.18	0.067	8.68	2495.69
		250	3701.18	387.28	0.11	18.85	3098.03
	Climate runs	Depth (m)	Mean (psu)	SD (psu)	CV	Slope (psu yr⁻¹)	Inter (psu)
Salinity	Naturalized	50	31.69	0.096	0.0030	-0.0029	31.78
		250	32.44	0.12	0.0037	-0.0046	32.58
	Regulated	50	31.33	0.13	0.0041	-0.0060	31.53
		250	32.24	0.13	0.0039	-0.0058	32.42

Table 4.4: The mean, standard deviation (SD), coefficient of variation (CV) in spring (MAM), fall (SON), and winter (DJF) heat content and temperature time series with slope and intercept (Inter) of the linear regressions (The trend starts in year 2006).

Variables	Climate runs	Depth (m)	Seasons	Mean (J)	SD (J)	CV	Slope (J yr ⁻¹)	Inter (J)
Heat content	Naturalized	50	Spring	6.63×10^{19}	1.78×10^{19}	0.27	8.49×10^{17}	3.91×10^{19}
			Fall	1.22×10^{21}	1.58×10^{20}	0.13	8.18×10^{18}	9.55×10^{20}
			Winter	2.22×10^{20}	7.20×10^{19}	0.32	3.65×10^{18}	1.07×10^{20}
		250	Spring	4.26×10^{20}	7.81×10^{19}	0.18	4.00×10^{18}	2.98×10^{20}
			Fall	1.82×10^{21}	2.55×10^{20}	0.14	1.33×10^{19}	1.40×10^{21}
			Winter	7.23×10^{20}	1.66×10^{20}	0.23	8.66×10^{18}	4.50×10^{20}
	Regulated	50	Spring	8.06×10^{19}	2.01×10^{19}	0.25	9.98×10^{17}	4.87×10^{19}
			Fall	1.22×10^{21}	1.57×10^{20}	0.13	8.15×10^{18}	9.59×10^{20}
			Winter	2.27×10^{20}	6.97×10^{19}	0.31	3.54×10^{18}	1.15×10^{20}
		250	Spring	4.86×10^{20}	9.45×10^{19}	0.19	4.88×10^{18}	3.30×10^{20}
			Fall	1.86×10^{21}	2.63×10^{20}	0.14	1.37×10^{19}	1.42×10^{21}
			Winter	7.67×10^{20}	1.72×10^{20}	0.22	9.02×10^{18}	4.82×10^{20}
Temperature	Naturalized	50	Spring	-1.50	0.080	-0.05	0.0038	-1.62
			Fall	3.69	0.71	0.19	0.037	2.51
			Winter	-0.80	0.33	-0.41	0.017	-1.32
		250	Spring	-1.02	0.14	-0.14	0.0074	-1.25
			Fall	1.54	0.47	0.30	0.024	0.76
			Winter	-0.47	0.30	-0.65	0.016	-0.97
	Regulated	50	Spring	-1.44	0.091	-0.063	0.0045	-1.58
			Fall	3.71	0.71	0.19	0.037	2.53
			Winter	-0.78	0.31	-0.41	0.016	-1.28
		250	Spring	-0.90	0.17	-0.19	0.0090	-1.19
			Fall	1.61	0.48	0.30	0.025	0.81
			Winter	-0.39	0.32	-0.81	0.017	-0.91

Table 4.5: The mean, standard deviation (SD), coefficient of variation (CV) in spring (MAM),fall (SON), and winter (DJF) freshwater content and salinity time series with slope and intercept (Inter) of the linear regressions (The trend starts in year 2006).

Variables	Climate runs	Depth	Seasons	Mean	SD	CV	Slope	Inter
		<i>(m)</i>		<i>(km³)</i>	<i>(km³)</i>		<i>(km³yr⁻¹)</i>	<i>(km³)</i>
Freshwater content	Naturalized	50	Spring	1796.41	133.61	0.074	5.17	1631.06
			Fall	2532.11	123.28	0.049	1.50	2484.13
			Winter	1978.12	131.11	0.066	4.75	1828.61
	Regulated	250	Spring	2483.63	300.96	0.12	13.20	2061.11
			Fall	3297.60	266.39	0.081	9.01	3009.42
			Winter	2832.57	303.53	0.11	12.87	2427.28
	Regulated	50	Spring	2361.57	220.45	0.093	10.74	2017.83
			Fall	3102.40	163.38	0.053	6.84	2883.46
			Winter	2527.51	201.06	0.080	9.94	2214.44
Salinity	Naturalized	250	Spring	3230.44	421.65	0.13	21.01	2558.15
			Fall	4061.04	352.24	0.087	16.51	3532.80
			Winter	3586.66	403.46	0.11	20.32	2946.44
	Regulated	50	Spring	31.98	0.12	0.0038	-0.0048	32.14
			Fall	31.46	0.084	0.0027	-0.0012	31.50
			Winter	31.83	0.10	0.0033	-0.0039	31.95
	Regulated	250	Spring	32.57	0.13	0.0041	-0.0055	32.75
			Fall	32.33	0.11	0.0034	-0.0037	32.45
			Winter	32.45	0.12	0.0038	-0.0048	32.61
Regulated	50	Spring	31.62	0.16	0.0052	-0.0080	31.87	
		Fall	31.11	0.10	0.0033	-0.0043	31.25	
		Winter	31.48	0.14	0.0043	-0.0067	31.69	
Regulated	250	Spring	32.37	0.14	0.0044	-0.0067	32.59	
		Fall	32.14	0.11	0.0035	-0.0049	32.29	
		Winter	32.26	0.12	0.0039	-0.0060	32.45	

Bibliography

- Aagaard, K., and E. C. Carmack, 1989: The role of sea ice and other fresh water in the arctic circulation. *Journal of Geophysical Research: Oceans*, **94 (C10)**, 14 485–14 498.
- Abdulla, C. P., M. A. Alsaafani, T. M. Alraddadi, and A. M. Albarakati, 2018: Mixed layer depth variability in the Red Sea. *Ocean Science*, **14 (4)**, 563–573.
- Akhter, J., L. Das, and A. Deb, 2017: CMIP5 ensemble-based spatial rainfall projection over homogeneous zones of India. *Climate Dynamics*, **49**.
- Andrews, J., D. Babb, D. G. Barber, and S. F. Ackley, 2017: Climate change and sea ice: Shipping accessibility on the marine transportation corridor through hudson bay and hudson strait (1980–2014). *Elementa: Science of the Anthropocene*, **5**.
- Andrews, J., D. Babb, D. G. Barber, and S. F. Ackley, 2018: Climate change and sea ice: shipping in hudson bay, hudson strait, and foxe basin (1980–2016). *Elementa: Science of the Anthropocene*, **6**.
- Andrews, J., D. Babb, M. McKernan, B. Horton, and D. Barber, 2016: Climate Change in the Hudson Bay Complex: Opportunities and Vulnerabilities for the Port of Churchill’s Marine Operations. Tech. rep., University of Manitoba, Centre for Earth Observation Science.
- Babb, D., and Coauthors, 2021: Sea ice dynamics in hudson strait and its impact on winter shipping operations. *Journal of Geophysical Research: Oceans*, e2021JC018024.
- Bouttes, N., D. Paillard, and D. Roche, 2010: Impact of brine-induced stratification on the glacial carbon cycle. *Climate of the Past*, **6**, 575–589.
- Braun, M., A. Thiombiano, M. Vieira, and T. Stadnyk, 2020: The changing climatology of hudson bay (1981–2070). *Elementa: Science of the Anthropocene*.
- Braun, M., A. N. Thiombiano, M. J. F. Vieira, and T. A. Stadnyk, 2021: Representing climate evolution in ensembles of GCM simulations for the Hudson Bay system. *Elementa: Science of the Anthropocene*, **9 (1)**.

- Bruneau, J., D. Babb, W. Chan, S. Kirillov, J. Ehn, J. Hanesiak, and D. G. Barber, 2021: The ice factory of hudson bay: Spatiotemporal variability of the kivalliq polynya. *Elem Sci Anth*, **9 (1)**, 00168.
- Burt, W. J., H. Thomas, L. A. Miller, M. A. Granskog, T. N. Papakyriakou, and L. Pengelly, 2016: Inorganic carbon cycling and biogeochemical processes in an arctic inland sea (hudson bay). *Biogeosciences*, **13 (16)**, 4659–4671.
- Canada, S., 2017: Census profile, 2016 census. *No. 98-316-X2016001, Version updated February 2018*.
- Chen, D., M. A. Cane, S. E. Zebiak, R. Canizares, and A. Kaplan, 2000: Bias correction of an ocean-atmosphere coupled model. *Geophysical Research Letters*, **27**, 2585–2588.
- Davis, P. E., C. Lique, H. L. Johnson, and J. D. Guthrie, 2016: Competing effects of elevated vertical mixing and increased freshwater input on the stratification and sea ice cover in a changing Arctic Ocean. *Journal of Physical Oceanography*, **46 (5)**, 1531–1553.
- Dee, D. P., and Coauthors, 2011: The ERA-Interim reanalysis: Configuration and performance of the data assimilation system. *Quarterly Journal of the royal meteorological society*, **137 (656)**, 553–597.
- Déry, S. J., T. J. Mlynowski, M. A. Hernández-Henríquez, and F. Straneo, 2011: Interannual variability and interdecadal trends in hudson bay streamflow. *Journal of Marine Systems*, **88 (3)**, 341–351.
- Déry, S. J., T. A. Stadnyk, M. K. MacDonald, and B. Gauli-Sharma, 2016: Recent trends and variability in river discharge across northern Canada. *Hydrology and Earth System Sciences*, **20 (12)**, 4801–4818.
- Donner, L. J., and Coauthors, 2011: The dynamical core, physical parameterizations, and basic simulation characteristics of the atmospheric component am3 of the gfdl global coupled model cm3. *Journal of Climate*, **24 (13)**, 3484–3519.
- Drinkwater, K., 1986: Physical oceanography of hudson strait and ungava bay. *Elsevier oceanography series*, Vol. 44, Elsevier, 237–264.

- Dunbar, M., 1982: Oceanographic research in hudson and james bays. *Naturaliste Canadien*, **109 (4)**, 677–683.
- Eastwood, R. A., R. Macdonald, J. Ehn, J. Heath, L. Arragutainaq, P. Myers, D. Barber, and Z. Kuzyk, 2020: Role of river runoff and sea ice brine rejection in controlling stratification throughout winter in southeast hudson bay. *Estuaries and Coasts*, **43**, 756–786.
- Elliot, R., V. Moulton, S. Raborn, and R. Davis, 2013: Hudson strait marine mammal aerial surveys, 10 march to 2 april. *A report prepared by LGL Ltd. for Baffinland Iron Mines Corporation, Toronto, ON.*
- Environment and Climate Change Canada, 2013: Sea ice climatic atlas for the northern Canadian waters 1981–2010. Government of Canada, accessed: 2022-03-15, <https://www.canada.ca/en/environment-climate-change/services/ice-forecasts-observations/publications/sea-climatic-atlas-northern-waters-1981-2010.html>.
- Ferland, J., M. Gosselin, and M. Starr, 2011: Environmental control of summer primary production in the hudson bay system: The role of stratification. *Journal of Marine Systems*, **88 (3)**, 385–400.
- Ford, J. D., W. A. Gough, G. J. Laidler, J. Macdonald, C. Irngaut, and K. Qrunnut, 2009: Sea ice, climate change, and community vulnerability in northern Foxe Basin, Canada. *Climate research*, **38 (2)**, 137–154.
- Gagnon, A. S., and W. A. Gough, 2005: Trends in the dates of ice freeze-up and breakup over Hudson Bay, Canada. *Arctic*, 370–382.
- Gagnon, A. S., and W. A. Gough, 2006: East–west asymmetry in long-term trends of landfast ice thickness in the Hudson Bay region, Canada. *Climate Research*, **32 (3)**, 177–186.
- Galley, R. J., B. G. Else, S. E. Howell, J. V. Lukovich, and D. G. Barber, 2012: Landfast sea ice conditions in the Canadian Arctic: 1983-2009. *Arctic*, 133–144.
- Granskog, M. A., Z. Z. A. Kuzyk, K. Azetsu-Scott, and R. W. Macdonald, 2011: Distributions of runoff, sea-ice melt and brine using $\delta^{18}\text{O}$ and salinity data—a new view on freshwater cycling in hudson bay. *Journal of Marine Systems*, **88 (3)**, 362–374.

- Gunn, G., 2015: Polynya formation in hudson bay during the winter period. M.S. thesis, Department of Environment and Geography, University of Manitoba.
- Hamilton, A., 2013: The Hudson Bay Complex in flux: contemplating the future of the world's largest seasonally ice-covered inland sea. Tech. rep., IISD (International Institute for Sustainable Development).
- Hayashida, H., and Coauthors, 2019: Csib v1 (canadian sea-ice biogeochemistry): a sea-ice biogeochemical model for the NEMO community ocean modelling framework. *Geoscientific Model Development*, **12** (5), 1965–1990.
- Hochheim, K., and D. Barber, 2010: Atmospheric forcing of sea ice in Hudson Bay during the fall period, 1980–2005. *Journal of Geophysical Research: Oceans*, **115**.
- Hochheim, K. P., and D. G. Barber, 2014: An update on the ice climatology of the Hudson Bay system. *Arctic, Antarctic, and Alpine Research*, **46** (1), 66–83.
- Houser, C., and W. A. Gough, 2003: Variations in sea ice in the hudson strait: 1971-1999. *Polar Geography*, **27** (1), 1–14.
- Hu, X., and P. Myers, 2015: An Effective Approach to Remap Runoff onto an Ocean Model Grid. CMOS Congress, Poster presented at the 2015 CMOS Congress, Whistler, BC.
- Ingram, R., and S. Prinsenberg, 1998: Coastal oceanography of hudson bay and surrounding eastern canadian arctic waters. *The sea*, **11** (29), 835–859.
- Ingram, R. G., and P. Larouche, 1987: Variability of an under-ice river plume in hudson bay. *Journal of Geophysical Research: Oceans*, **92** (C9), 9541–9547.
- JafariKhasragh, S., J. V. Lukovich, X. Hu, P. G. Myers, K. Sydor, and D. G. Barber, 2019: Modelling sea surface temperature (SST) in the Hudson Bay Complex using bulk heat flux parameterization: Sensitivity to atmospheric forcing, and model resolution. *Atmosphere-Ocean*, **57**, 120–133.
- Kirillov, S., and Coauthors, 2020: Atmospheric forcing drives the winter sea ice thickness asymmetry of hudson bay. *Journal of Geophysical Research: Oceans*, **125**, e2019JC015756.

- Kuzyk, Z., and L. Candlish, 2019: From science to policy in the greater hudson bay marine region: An integrated regional impact study (iris) of climate change and modernization. *ArcticNet, Québec City*, 424.
- Laidler, G. J., and P. Elee, 2008: Human geographies of sea ice: freeze/thaw processes around Cape Dorset, Nunavut, Canada. *Polar Record*, **44** (1), 51–76.
- Laidler, G. J., J. D. Ford, W. A. Gough, T. Ikummaq, A. S. Gagnon, S. Kowal, K. Qrunnut, and C. Irngaut, 2009: Travelling and hunting in a changing Arctic: Assessing Inuit vulnerability to sea ice change in Igloolik, Nunavut. *Climatic change*, **94** (3), 363–397.
- Landy, J. C., J. K. Ehn, D. G. Babb, N. Thériault, and D. G. Barber, 2017: Sea ice thickness in the eastern canadian arctic: Hudson bay complex & baffin bay. *Remote Sensing of Environment*, **200**, 281–294.
- Large, W., and S. Yeager, 2009: The global climatology of an interannually varying air–sea flux data set. *Climate dynamics*, **33** (2), 341–364.
- Lavoie, D., N. Lambert, and A. van der Baaren, 2013: Projections of future physical and biogeochemical conditions in Hudson and Baffin bays from CMIP5 Global Climate Models. Tech. rep., Fisheries and Oceans Canada Pelagic and Ecosystem Science Branch Maurice Lamontagne Institute.
- Leppäranta, M., 2011: *The drift of sea ice*. Springer Science & Business Media.
- Liang, X., and M. Losch, 2018: On the effects of increased vertical mixing on the Arctic Ocean and sea ice. *Journal of Geophysical Research: Oceans*, **123** (12), 9266–9282.
- Lukovich, J. V., and Coauthors, 2021: Simulated impacts of relative climate change and river discharge regulation on sea ice and oceanographic conditions in the hudson bay complex. *Elem Sci Anth*, **9** (1), 00127.
- McCullough, G., and Coauthors, 2019: Freshwater–marine interactions in the greater hudson bay marine region. *From science to policy in the Greater Hudson Bay Marine Region: An Integrated Regional Impact Study (IRIS) of climate change and modernization. Québec City, Québec, Canada: ArcticNet*, 155–197.

- Morales Maqueda, M., A. Willmott, and N. Biggs, 2004: Polynya dynamics: A review of observations and modeling. *Reviews of Geophysics*, **42** (1).
- Nummelin, A., M. Ilicak, C. Li, and L. H. Smedsrud, 2016: Consequences of future increased Arctic runoff on Arctic Ocean stratification, circulation, and sea ice cover. *Journal of Geophysical Research: Oceans*, **121** (1), 617–637.
- Pennelly, C., and P. G. Myers, 2021: Impact of different atmospheric forcing sets on modeling Labrador Sea Water production. *Journal of Geophysical Research: Oceans*, **126** (2), e2020JC016452.
- Prinsenber, S., 1980: Man-made changes in the freshwater input rates of Hudson and James Bays. *Canadian Journal of Fisheries and Aquatic Sciences*, **37** (7), 1101–1110.
- Prinsenber, S., 1986a: On the physical oceanography of Foxe Basin. *Elsevier oceanography series*, Vol. 44, Elsevier, 217–236.
- Prinsenber, S., 1986b: Salinity and temperature distributions of hudson bay and james bay. *Elsevier oceanography series*, Vol. 44, Elsevier, 163–186.
- Prinsenber, S., 1988: Ice-cover and ice-ridge contributions to the freshwater contents of hudson bay and foxe basin. *Arctic*, 6–11.
- Rampal, P., J. Weiss, and D. Marsan, 2009: Positive trend in the mean speed and deformation rate of arctic sea ice, 1979–2007. *Journal of Geophysical Research: Oceans*, **114** (C5).
- Ridenour, N. A., X. Hu, K. Sydor, P. G. Myers, and D. G. Barber, 2019a: Revisiting the circulation of hudson bay: Evidence for a seasonal pattern. *Geophysical Research Letters*, **46** (7), 3891–3899.
- Ridenour, N. A., F. Straneo, J. Holte, Y. Gratton, P. G. Myers, and D. G. Barber, 2021: Hudson strait inflow: Structure and variability. *Journal of Geophysical Research: Oceans*, **126** (9), e2020JC017089.
- Ridenour, N. A., and Coauthors, 2019b: Sensitivity of freshwater dynamics to ocean model

- resolution and river discharge forcing in the Hudson Bay Complex. *Journal of Marine Systems*, **196**, 48–64.
- Sallée, J.-B., and Coauthors, 2021: Summertime increases in upper-ocean stratification and mixed-layer depth. *Nature*, **591 (7851)**, 592–598.
- Sandeep, K., and V. Pant, 2019: Riverine freshwater plume variability in the Bay of Bengal using wind sensitivity experiments. *Deep Sea Research Part II: Topical Studies in Oceanography*, **168**, 104–149.
- Saucier, F., S. Senneville, S. Prinsenbergh, F. Roy, G. Smith, P. Gachon, D. Caya, and R. Laprise, 2004: Modelling the sea ice-ocean seasonal cycle in Hudson Bay, Foxe Basin and Hudson Strait, Canada. *Climate Dynamics*, **23 (3-4)**, 303–326.
- Saucier, F. J., and J. Dionne, 1998a: A 3-d coupled ice-ocean model applied to hudson bay, canada: The seasonal cycle and time-dependent climate response to atmospheric forcing and runoff. *Journal of Geophysical Research: Oceans*, **103**, 27 689–27 705.
- Saucier, F. J., and J. Dionne, 1998b: A 3-D coupled ice-ocean model applied to Hudson Bay, Canada: The seasonal cycle and time-dependent climate response to atmospheric forcing and runoff. *Journal of Geophysical Research: Oceans*, **103 (C12)**, 27 689–27 705.
- SMith, S. D., R. D. Muench, and C. H. Pease, 1990: Polynyas and leads: An overview of physical processes and environment. *Journal of Geophysical Research: Oceans*, **95 (C6)**, 9461–9479.
- Sohail, T., D. B. Irving, J. D. Zika, R. M. Holmes, and J. A. Church, 2021: Fifty year trends in global ocean heat content traced to surface heat fluxes in the sub-polar ocean. *Geophysical Research Letters*, **48 (8)**, e2020GL091 439.
- Somavilla, R., C. González-Pola, and J. Fernández-Díaz, 2017: The warmer the ocean surface, the shallower the mixed layer. how much of this is true? *Journal of Geophysical Research: Oceans*, **122 (9)**, 7698–7716.
- St-Laurent, P., F. Straneo, and D. G. Barber, 2012: A conceptual model of an Arctic sea. *Journal of Geophysical Research: Oceans*, **117 (C6)**.

- Stadnyk, T. A., S. J. Déry, M. K. MacDonald, and K. Kristina, 2019: The freshwater system. *From Science to Policy in the Greater Hudson Bay Marine Region: An Integrated Regional Impact Study (IRIS) of Climate Change and Modernization*, ArcticNet, 113–154.
- Stadnyk, T. A., and Coauthors, 2021: Changing freshwater contributions to the Arctic: A 90-year trend analysis (1981–2070). *Elem Sci Anth*, **9 (1)**, 00 098.
- Stewart, D., and D. Barber, 2010: The ocean-sea ice-atmosphere system of the hudson bay complex. *A little less Arctic*, Springer, 1–38.
- Stewart, D., and W. Lockhart, 2005a: An overview of the Hudson Bay marine ecosystem. Tech. rep., Central and Arctic Region Fisheries and Oceans Canada.
- Stewart, D. B., and W. Lockhart, 2005b: *An overview of the Hudson Bay marine ecosystem*. Department of Fisheries and Oceans, Central and Arctic Region.
- Straneo, F., and F. Saucier, 2008: The outflow from hudson strait and its contribution to the labrador current. *Deep Sea Research Part I: Oceanographic Research Papers*, **55 (8)**, 926–946.
- Stringer, W. J., and J. Groves, 1991: Location and areal extent of polynyas in the bering and chukchi seas. *Arctic*, 164–171.
- Tamura, T., and K. I. Ohshima, 2011: Mapping of sea ice production in the arctic coastal polynyas. *Journal of Geophysical Research: Oceans*, **116 (C7)**.
- Taylor, K. E., R. J. Stouffer, and G. A. Meehl, 2012: An overview of CMIP5 and the experiment design. *Bulletin of the American Meteorological Society*, **93**, 485–498.
- Teutschbein, C., and J. Seibert, 2012: Bias correction of regional climate model simulations for hydrological climate-change impact studies: Review and evaluation of different methods. *Journal of Hydrology*, **456–457**, 12–29.
- Tivy, A., S. E. Howell, B. Alt, S. McCourt, R. Chagnon, G. Crocker, T. Carrieres, and J. J. Yackel, 2011: Trends and variability in summer sea ice cover in the Canadian Arctic

- based on the Canadian Ice Service Digital Archive, 1960–2008 and 1968–2008. *Journal of Geophysical Research: Oceans*, **116** (C3).
- Tomita, H., K. Kutsuwada, M. Kubota, and T. Hihara, 2021: Advances in the estimation of global surface net heat flux based on satellite observation: J-OFURO3 V1.1. *Frontiers in Marine Science*, **8**, 8.
- Von Schuckmann, K., and Coauthors, 2020: Heat stored in the Earth system: where does the energy go? *Earth System Science Data*, **12** (3), 2013–2041.
- Watanabe, M., and Coauthors, 2010: Improved climate simulation by MIROC5: mean states, variability, and climate sensitivity. *Journal of Climate*, **23** (23), 6312–6335.
- Westdal, K., P. Richard, and J. Orr, 2010: Migration route and seasonal home range of the northern hudson bay narwhal (*monodon monoceros*). *A Little Less Arctic*, Springer, 71–92.
- Xu, Z., Y. Han, C. Tam, Z. Yang, and C. Fu, 2021: Bias-corrected CMIP6 global dataset for dynamical downscaling of the historical and future climate (1979–2100). *Scientific Data*, **8** (1), 1–11.
- Yang, D., B. Ye, and D. L. Kane, 2004a: Streamflow changes over Siberian Yenisei river basin. *Journal of Hydrology*, **296** (1-4), 59–80.
- Yang, D., B. Ye, and A. Shiklomanov, 2004b: Discharge characteristics and changes over the Ob River watershed in Siberia. *Journal of Hydrometeorology*, **5** (4), 595–610.
- Yu, Y., H. Stern, C. Fowler, F. Fetterer, and J. Maslanik, 2014: Interannual variability of arctic landfast ice between 1976 and 2007. *Journal of Climate*, **27** (1), 227–243.
- Yukimoto, S., and Coauthors, 2012: A new global climate model of the meteorological research institute: Mri-cgcm3—model description and basic performance—. *Journal of the Meteorological Society of Japan. Ser. II*, **90**, 23–64.

Chapter 5

Conclusion

The Hudson Bay Complex (HBC) is a region of the Canadian Arctic that is influenced by a combination of various physical processes. The complex is characterized by several unique features that make it distinct from other marine systems, such as its large freshwater input from the surrounding rivers and its seasonal ice cover (Braun et al., 2021; Ridenour et al., 2019).

The physical dynamics of the HBC are governed by a variety of processes, including ocean currents, tides, and winds. The most significant factor is the inflow of freshwater from rivers, which has a considerable impact on the stratification and circulation of the system. The freshwater discharge from rivers affects the density and salinity of the water, leading to a significant change in the vertical and horizontal circulation of the HBC (Braun et al., 2021; Florindo-López et al., 2020; Ridenour et al., 2019). Furthermore, tides play a crucial role in mixing the water column and creating currents in the HBC. The tides in the Hudson Bay region have a complex pattern due to the presence of numerous islands and shallow regions, which can generate internal waves that propagate and affect the water dynamics (Braun et al., 2021; Petrushevich et al., 2020).

The thermodynamics properties of the HBC are also influenced by various processes, including solar radiation, heat exchange with the atmosphere, and sea-ice formation and melting that have been discussed in Chapter 4. The seasonal ice cover is an essential factor that affects the heat balance of the system. During the winter months, the ice cover isolates the water from the atmosphere, reducing the heat loss from the water to the air. However, in summer, the melting of sea ice exposes the water to solar radiation, leading to a significant increase in

surface heating (Braun et al., 2021; Petrusевич et al., 2020). In addition, the biogeochemical properties of the HBC are also strongly influenced by the freshwater input from rivers, which can affect the nutrient concentrations, primary productivity, and carbon cycle of the system (Braun et al., 2021; Florindo-López et al., 2020).

In conclusion, the Hudson Bay Complex is a unique marine system that is influenced by a variety of physical processes. The dynamics of the system are governed by the inflow of freshwater from rivers and winds, while the thermodynamics properties are influenced by solar radiation, heat exchange with the atmosphere, and sea-ice formation and melting. The work in our thesis highlights the importance of understanding these processes to accurately model and predict the behavior of the HBC in the context of global climate change.

5.1 Main Findings

The analysis we made in previous Chapters leads us to the following conclusions:

- (1) The surface air temperature and precipitation are linked with the ocean and ice properties. Precipitation plays a smaller role than melting ice and river runoff in freshwater changes.
- (2) In the HBC, the deep MLDs can reach depths of around 230 m along the north side of the HS due to the loss of sea ice and the exposure of surface water to cold winter conditions, which leads to deep mixing. However, augmented freshwater from rivers and ice melting are projected to lead to slightly shallower mixed layers in the future (2006–2070), compared to historical period (1981–2005).
- (3) Increased freshwater volume was transported into the HBC with river regulation. As global warming intensifies, a substantial increase in both freshwater and heat content is projected under different representative CO₂ concentrations (RCP4.5 and RCP8.5). However, a strong warming effect is also expected to cause a steep decrease in sea ice thickness (about 0.3 m) and concentration (about 22%) by 2070.
- (4) Over the next 50 years, the HBC temperature will warm and the sea-ice concentration and thickness will significantly decrease. The transition from naturalized to regulated

river runoff has little impact on the warming of ocean temperature and the averaged sea-ice variations.

- (5) Salinity and FWC variations are highly relevant to different members of the ensemble, influenced by the hydrological cycle evolution in climate models. Changes in inflow and residence time affect the overall freshwater budget changes. The differences in salinity and freshwater content between naturalized and regulated regimes are inferred to be associated with the freshwater residence time and the timing of discharge, which are at least as important as the total long-term freshwater input for salinity in the HBC.

5.1.1 The Significance of Findings

The results are important as they provide an understanding of the potential impact of climate change on the HBC system. They help to understand the impact of climate change on the sea ice cover in the HBC, and the potential consequences for the marine ecosystem and regional climate. The projected decline in SIC and SIT has significant implications for the timing and duration of the open water season, as well as the amount of freshwater added to the HBC from melting sea ice. They demonstrate the impact of climate change on the ocean's temperature and heat content. This information is essential in predicting future changes in oceanic systems and for informing strategies to mitigate the impact of climate change. Moreover, the results suggest that river regulation has little impact on temperature and heat content, which means it barely controls ocean temperature variability. Our study also highlights the importance of considering freshwater input in understanding the changes in salt-determined stratification of the HBC.

The study provides useful information for policymakers and stakeholders to make informed decisions concerning the HBC system's conservation and management. It is crucial to have information on the potential effects of climate change and river regulation to develop strategies to mitigate their impacts.

5.2 Thesis Summary

This thesis focuses on how different climate scenarios and river discharge regulation affect the Hudson Bay system. Our study utilized an ensemble of climate-driven data from the fifth Coupled Model Intercomparison Project (CMIP5). The data included atmospheric forcing fields such as sea surface temperature, precipitation, humidity, short- and long-wave radiation, surface pressure, and zonal and meridional surface winds. We found that there is a general increase in surface air temperature, which is considered a precursor, symptom, and consequence of climate change. This study predicts a future increase in temperature and precipitation rates, with precipitation rates expected to increase by 18.60%, 25.05%, and 62.58% in the spring, fall, and winter, respectively. Additionally, there are only slight differences in surface wind speed (U_{10}) on either seasonal or yearly scales.

The sea ice cover in the HBC plays a crucial role in the ecology of the marine system, influences atmosphere-ice-sea interactions, and is both an indicator of climate change and a crucial driver of regional climate. This study investigated the properties of sea ice in the HBC, focusing on the annual and seasonal variations of sea ice concentration (SIC) and sea ice thickness (SIT). The results show that both SIC and SIT have decreased over the entire time period. The annual mean SIC is projected to reduce from $50 \pm 2\%$ for the historical control to $39 \pm 9\%$ for the future scenario, representing an overall 22% decrease. The annual mean SIT is projected to be 0.37 ± 0.04 m in the near future and 0.28 ± 0.04 m in the far future, compared to the historical mean of 0.57 ± 0.07 m.

In this thesis, the importance of understanding ocean temperature and heat content due to their response to climate change and river regulation has been discussed. Equations for computing heat content based on temperature at different depths are presented, and variations of this heat content with time under different scenarios are described. Our results show that the ocean temperature is projected to increase, with a higher rate in the upper 50 meters compared to the upper 250 meters. Additionally, after river regulation, the variability of ocean temperature is found to be reduced.

Moreover, the salinity and freshwater content are examined to estimate the changes in salt-determined stratification. A reference salinity of 33 is used to calculate liquid freshwater

content (FWC) based on salinity. The freshwater storage (FWS) can be estimated by integrating FWC over the HBC. It is noted that the FWC calculation is to estimate how much freshwater would be needed to change water of a given salinity to that reference. The results show that the ensemble means of annual salinity in the top 50 m and 250 m ocean layers only decrease by 0.2 and 0.3, respectively, while freshwater content increases by 211.25 km³ and 728 km³ from 2006 to 2070 with naturalized river runoff. Higher ocean salinities (+2.4%) and freshwater contents (+33.5%) are found in deeper ocean layer from the upper 50 m to 250 m. However, there are large discrepancies of salinity and freshwater content among the five ensemble members.

The trends of salinity and freshwater content with regulated river runoff are also studied. The reduction of ensemble means of annual salinity in the top 50 m and 250 m ocean columns over the future period are slightly larger than the same conditions with unregulated rivers, as 0.39 and 0.38, respectively. However, the trends in freshwater content of all regulated ensemble members in future period are positive, where means of the top 50 m and 250 m FWCs are suggested to increase by 564.20 km³ and 1225.25 km³ from 2006 to 2070.

With regard to the research questions listed in the section 1.4, we now answer them as follows:

- Under the circumstance of climate change, how would the ocean and ice properties respond?

Climate change is expected to have significant impacts on the properties of the ocean and sea ice in the HBC. Warmer air temperatures and increased freshwater runoff from land are expected to increase surface ocean temperatures and decrease sea ice extent and thickness, leading to enhanced stratification of the water column and changes in the region (Garcia-Soto et al., 2021; Zellen, 2009; Lindsey and Scott, 2019). These changes can have cascading effects on the marine ecosystem, affecting primary productivity, nutrient cycling, and the distribution and abundance of species.

- What effects would exist if river regulation, defined as controlling rivers to meet human demands for domestic and industrial water supplies, is applied in the five simulated climate runs?

River regulation, defined as the control of river flow to meet human demands, can have significant effects on the physical properties of the ocean and the marine ecosystem in the HBC. The effects of river regulation on the HBC will depend on the location, timing, and intensity of the river discharge. For example, increased river discharge can lead to changes in water column stratification, nutrient availability, and primary productivity, as well as changes in the distribution and abundance of species (Masotti et al., 2018). However, river regulation can also have negative impacts on the marine ecosystem, including changes in salinity, increased sedimentation, and the introduction of pollutants and pathogens (Nilsson and Renöfält, 2008).

- How does atmospheric forcing variability affect the ocean, sea ice, and the atmosphere itself?

Atmospheric forcing variability can have significant effects on the physical properties of the ocean, sea ice, and the atmosphere itself in the HBC (Liang et al., 2020). Variability in air temperature, wind, and precipitation can affect the surface ocean temperature, water column stratification, sea ice extent and thickness, and the distribution and abundance of species (Skogseth et al., 2020; Janout et al., 2020). In addition, atmospheric variability can affect the exchange of heat, moisture, and momentum between the ocean and the atmosphere, leading to changes in atmospheric circulation patterns and weather conditions in the region (Cronin et al., 2019; Taylor et al., 2018). Understanding the interactions between the atmosphere, ocean, and sea ice is crucial for predicting the response of the HBC to future climate change and river regulation.

5.2.1 Limitations and Further work

This study, outlined in Section 4.4, has illuminated certain limitations that signal potential avenues for future enhancement:

- (1) Refining Bathymetric Data: Further research could focus on gathering and refining detailed bathymetric information for the Hudson Bay. This effort would enhance the accuracy of tidal simulations and provide a more comprehensive understanding of ocean dynamics.

- (2) **Advanced Sea Ice Modeling:** Exploring advanced sea ice models tailored to the region could broaden the scope of variables examined, encompassing sea fluxes and their interactions with other oceanic processes. For example, employing multi-category sea ice models such as LIM3 can lead to more realistic ice simulations.
- (3) **Enhanced River Discharge Representation:** Prospective studies might endeavor to enhance the accuracy of river discharge representation in simulations. This could encompass integrating more comprehensive data sources and refining the hydrological model to capture a wider spectrum of factors influencing river flow.

These potential future directions address the identified limitations and have the potential to contribute to a more comprehensive and accurate analysis of the study's focus.

Moreover, there are additional opportunities for improvement that can be pursued. While the remapping method used in this study was found to be more accurate than simple interpolation (Hu and Myers, 2015), recent studies have developed more advanced remapping techniques. For example, Biastoch et al. (2021) created a tool for remapping the JRA55-do dataset to the NEMO model that can more realistically address the issue of spatial fine-scale heterogeneity by reassigning runoff to the simulated coastline. By exploring and applying these advanced remapping methods, more accurate and realistic simulations of coastal ocean dynamics and biogeochemistry can be achieved.

To improve upon the results of this study, it would be valuable to consider the impact of river regulation on other oceanographic variables such as currents and eddies. Previous studies have shown that river runoff can influence the ocean circulation and the formation of eddies in coastal regions (Auricht et al., 2022; Korotenko et al., 2022). The variations of maximum mixed layer depth (MMLD) in the HBC can be attributed to a complex interplay of physical processes. It is likely that the predicted increase in the mixed layer depth in the HBC from 2021 to 2070 is due to a combination of factors listed in section 4.3.3. However, the exact mechanisms and their relative contributions are still subject to ongoing research and modeling efforts in physical oceanography. Further research is needed such as sensitivity studies on vertical mixing processes, diffusivity and representation of the thermocline, to better understand the relative importance of each factor and how they may evolve in the

future, particularly in the context of ongoing climate change.

Another area for improvement is the use of higher resolution models to better capture the coastal processes that are important in the HBC. This could include incorporating the effects of tides, waves, and coastal upwelling in the models, which have been shown to play an important role in the transport and mixing of water masses in coastal regions (Liang and Zhou, 2022; Tinker et al., 2022).

Finally, incorporating observations into future studies to validate models and improve their accuracy would be beneficial. Data from moored instruments, autonomous underwater vehicles, and satellites could corroborate model results and offer further insights into the HBC's physical processes. Combining models and observations can yield a comprehensive understanding of climate change and river regulation impacts on the HBC.

Overall, the results of this study provide important information for policymakers and researchers alike to understand the impacts of climate change on high-latitude regions and the importance of freshwater management in these areas. There is a need for more comprehensive studies to investigate the effects of river regulation on the physical processes in the HBC, particularly in the context of climate change. By using higher resolution models and incorporating observations, we can improve our understanding of these complex systems and better predict their response to future changes in the environment.

Bibliography

- Auricht, H., L. Mosley, M. Lewis, and K. Clarke, 2022: Mapping the long-term influence of river discharge on coastal ocean chlorophyll-a. *Remote Sensing in Ecology and Conservation*, **8** (5), 629–643.
- Biastoch, A., and Coauthors, 2021: Regional imprints of changes in the Atlantic Meridional Overturning Circulation in the eddy-rich ocean model VIKING20X. *Ocean Science*, **17** (5), 1177–1211.
- Braun, M., A. N. Thiombiano, M. J. Vieira, and T. A. Stadnyk, 2021: Representing climate evolution in ensembles of GCM simulations for the Hudson Bay System. *Elem Sci Anth*, **9** (1), 00011.
- Cronin, M. F., and Coauthors, 2019: Air-sea fluxes with a focus on heat and momentum. *Frontiers in Marine Science*, **6**, 430.
- Florindo-López, C., S. Bacon, Y. Aksenov, L. Chafik, E. Colbourne, and N. P. Holliday, 2020: Arctic Ocean and Hudson Bay freshwater exports: New estimates from seven decades of hydrographic surveys on the Labrador Shelf. *Journal of Climate*, **33** (20), 8849–8868.
- Garcia-Soto, C., and Coauthors, 2021: An overview of ocean climate change indicators: sea surface temperature, ocean heat content, ocean pH, dissolved oxygen concentration, Arctic Sea ice extent, thickness and volume, sea level and strength of the AMOC (Atlantic Meridional Overturning Circulation). *Frontiers in Marine Science*, **8**, 642372.
- Hu, X., and P. Myers, 2015: An Effective Approach to Remap Runoff onto an Ocean Model Grid. CMOS Congress, Poster presented at the 2015 CMOS Congress, Whistler, BC.
- Janout, M. A., J. Hölemann, G. Laukert, A. Smirnov, T. Krumpfen, D. Bauch, and L. Timokhov, 2020: On the variability of stratification in the freshwater-influenced Laptev Sea Region. *Frontiers in Marine Science*, **7**, 543489.
- Korotenko, K., A. Osadchiv, and V. Melnikov, 2022: Mesoscale Eddies in the Black Sea and Their Impact on River Plumes: Numerical Modeling and Satellite Observations. *Remote Sensing*, **14** (17), 4149.

- Liang, H., and X. Zhou, 2022: Impact of tides and surges on fluvial floods in coastal regions. *Remote Sensing*, **14** (22), 5779.
- Liang, Y., H. Bi, Y. Wang, Z. Zhang, and H. Huang, 2020: Role of atmospheric factors in forcing Arctic sea ice variability. *Acta Oceanologica Sinica*, **39**, 60–72.
- Lindsey, R., and M. Scott, 2019: Climate Change: Arctic sea ice summer minimum. *Climate.gov. September*, **26**.
- Masotti, I., P. Aparicio-Rizzo, M. A. Yevenes, R. Garreaud, L. Belmar, and L. Fariás, 2018: The influence of river discharge on nutrient export and phytoplankton biomass off the central Chile Coast (33–37 S): seasonal cycle and interannual variability. *Frontiers in Marine Science*, **5**, 423.
- Nilsson, C., and B. M. Renöfält, 2008: Linking flow regime and water quality in rivers: a challenge to adaptive catchment management. *Ecology and Society*, **13** (2).
- Petrusevich, V. Y., I. A. Dmitrenko, A. Niemi, S. A. Kirillov, C. M. Kamula, Z. Z. A. Kuzyk, D. G. Barber, and J. K. Ehn, 2020: Impact of tidal dynamics on diel vertical migration of zooplankton in Hudson Bay. *Ocean Science*, **16** (2), 337–353.
- Ridenour, N. A., X. Hu, K. Sydor, P. G. Myers, and D. G. Barber, 2019: Revisiting the circulation of hudson bay: Evidence for a seasonal pattern. *Geophysical Research Letters*, **46** (7), 3891–3899.
- Skogseth, R., and Coauthors, 2020: Variability and decadal trends in the Isfjorden (Svalbard) ocean climate and circulation—An indicator for climate change in the European Arctic. *Progress in Oceanography*, **187**, 102394.
- Taylor, P. C., B. M. Hegyi, R. C. Boeke, and L. N. Boisvert, 2018: On the increasing importance of air-sea exchanges in a thawing Arctic: A review. *Atmosphere*, **9** (2), 41.
- Tinker, J., J. A. Polton, P. E. Robins, M. J. Lewis, and C. K. O’Neill, 2022: The influence of tides on the North West European shelf winter residual circulation. *Frontiers in Marine Science*, **9**.

Zellen, B. S., 2009: *Arctic doom, Arctic boom: the geopolitics of climate change in the Arctic*.
ABC-CLIO.